

UC Berkeley

UC Berkeley Electronic Theses and Dissertations

Title

Micromechanics of the Human Proximal Femur: Role of Microstructure and Tissue-Level Ductility on Femoral Strength

Permalink

<https://escholarship.org/uc/item/4s53t3hp>

Author

Nawathe, Shashank

Publication Date

2014

Peer reviewed|Thesis/dissertation

**Micromechanics of the Human Proximal Femur:
Role of Microstructure and Tissue-Level Ductility on Femoral Strength**

by

Shashank Nawathe

A dissertation submitted in partial satisfaction of the

requirements for the degree of

Doctor of Philosophy

in

Engineering – Mechanical Engineering

in the

Graduate Division

of the

University of California, Berkeley

Committee in Charge:

Professor Tony M. Keaveny, Chair

Professor Lisa Pruitt

Professor Jon Wilkening

Fall 2014

Micromechanics of the Human Proximal Femur:
Role of Microstructure and Tissue-Level Ductility on Femoral Strength

© 2014

by

Shashank Nawathe

ABSTRACT

Micromechanics of the Human Proximal Femur: Role of Microstructure and Tissue-Level Ductility on Femoral Strength

by

Shashank Nawathe

Doctor of Philosophy in Engineering – Mechanical Engineering

University of California, Berkeley

Professor Tony M. Keaveny, Chair

Knowledge of the micromechanics of the human proximal femur is fundamental to improving clinical assessment of hip fracture risk and to understand the etiology of hip fractures. In this context, the focus of this dissertation was to enhance the current understanding of the role of bone microstructure and tissue-level ductility in the whole-bone failure behavior.

Combining the latest advances in micro-computed tomography and high-resolution finite element modeling, we investigated the fundamental issue of load-sharing between the cortical and trabecular bone in the proximal femur. Well-delineated, consistent regions of load-transfer in the proximal portion of the femoral neck and load-sharing in the distal portion were identified, both for a sideways fall and stance loading of the femur, and the mechanisms by which high stresses can develop in the cortical and trabecular bone tissue were demonstrated.

Using non-linear finite element analysis, microstructural failure mechanisms of the human proximal femur during a sideways fall loading were elucidated. The simulations revealed that structure-level failure of the weaker femurs was associated with a relatively lower proportion of tissue-level failure compared to the stronger femurs — an indication of diminished structural redundancy in the weaker bones. The trabecular tissue failure always preceded and was more prominent than cortical tissue failure in all femurs, and dominated in the very weakest bones. A new morphological measure of hip fragility was identified: the proportion of trabecular bone compared with cortical bone in the femoral neck. This measure was a strong predictor of femoral strength even after adjusting for the effects of areal bone mineral density (aBMD), the current clinical gold-standard for fracture risk assessment.

The work presented in this dissertation has also provided new insight into the influence of tissue-level ductility on structure-level bone strength. It was revealed that the structure-level bone strength reduced substantially (by 40-60%) when the manner in which bone tissue deforms was altered from fully ductile to fully brittle. This effect was relatively uniform across all the specimens of an anatomic site subjected to similar kind of loading, but was greater for the femurs during a sideways fall compared to stance loading. This dissertation also evaluated the effect of

typical population-variations in tissue-level ductility on the femoral strength. It was revealed that there was only a modest variation (~10-12%) in the femoral strength when both cortical and trabecular tissue ductility were simultaneously varied by one standard deviation about their mean.

In closure, this dissertation answers fundamental questions regarding the role of cortical and trabecular bone, and the underlying microstructural failure mechanisms, during age-related hip fractures, and provides new insight into the relationship between tissue-level ductility and structure-level bone strength. This work also outlines potential areas of future research to further advance our understanding of hip fracture etiology and describes a systematic approach to perform morphometric analysis on the bones so as to identify biomechanics-based structural determinants of femoral strength.

Tony M. Keaveny
Dissertation Committee Chair

To,
Mom and Dad

TABLE OF CONTENTS

ABSTRACT.....	1
TABLE OF CONTENTS	II
LIST OF FIGURES	IV
LIST OF TABLES.....	VIII
ACKNOWLEDGEMENTS	IX
1. INTRODUCTION	1
1.1 <i>Structure and composition of bone.....</i>	2
1.2 <i>Anatomy of the proximal femur</i>	4
1.3 <i>Mechanical behavior of the proximal femur</i>	5
1.4 <i>Tissue-level ductility for the human bone.....</i>	6
1.5 <i>Computational modeling of the bone.....</i>	8
1.6 <i>Objectives and scope</i>	9
2. CORTICAL-TRABECULAR LOAD-SHARING IN THE HUMAN FEMORAL NECK.....	20
2.1 <i>Introduction</i>	20
2.2 <i>Methods</i>	20
2.3 <i>Results.....</i>	22
2.4 <i>Discussion.....</i>	23
3. MICROSTRUCTURAL FAILURE MECHANISMS IN THE HUMAN PROXIMAL FEMUR FOR SIDWAYS FALL LOADING	32
3.1 <i>Introduction</i>	32
3.2 <i>Methods</i>	32

3.3	<i>Results</i>	35
3.4	<i>Discussion</i>	36
4.	THEORETICAL BOUNDS FOR THE INFLUENCE OF TISSUE-LEVEL DUCTILITY ON THE APPARENT-LEVEL STRENGTH OF HUMAN TRABECULAR BONE	49
4.1	<i>Introduction</i>	49
4.2	<i>Methods</i>	49
4.3	<i>Results</i>	51
4.4	<i>Discussion</i>	52
5.	EFFECT OF TISSUE-LEVEL DUCTILITY ON VERTEBRAL AND FEMORAL STRENGTH. 63	
5.1	<i>Introduction</i>	63
5.2	<i>Methods</i>	63
5.3	<i>Results</i>	66
5.4	<i>Discussion</i>	67
5.5	<i>Appendix</i>	69
6.	INFLUENCE OF TYPICAL POPULATION-VARIATIONS IN TISSUE-LEVEL DUCTILITY ON THE FEMORAL STRENGTH	79
6.1	<i>Introduction</i>	79
6.2	<i>Methods</i>	79
6.3	<i>Results</i>	81
6.4	<i>Discussion</i>	82
7.	CONCLUSIONS	93
8.	REFERENCES	98

LIST OF FIGURES

Figure 1-1: Cumulative survival probability by sex and type of fracture [4].	12
Figure 1-2: Hierarchical structures of bone from the sub-micron length scale to the millimeter length scale [29].	13
Figure 1-3: High-resolution renderings of trabecular bone from: a) bovine proximal tibia; b) human proximal tibia; c) human femoral neck; d) human vertebra [97].	14
Figure 1-4: Proximal femur compartmentalized (left) into femoral head, neck, and trochanter regions (left). Cortical bone shell and trabecular bone core identified (right) using a ray-based search algorithm [98].	15
Figure 1-5: Classification of hip fractures. Femoral neck and intertrochanteric fractures (top row) are the most commonly observed types (Adapted from: http://advancedortho.net/info/hipfractureinfo.php).	16
Figure 1-6: Mid-frontal sections of human femurs from 66-year old (left) and 93-year old (right) donors. Aging and disease result in substantial loss of bone mass, deterioration in trabecular microarchitecture, decrease in cortical thickness and increase in cortical porosity.	17
Figure 1-7: Age-related variations in ultimate strain, a measure of tissue-level ductility, for cortical and trabecular bone tissue. Ultimate strains decrease with aging for cortical tissue [25] but not for trabecular tissue [76].	18
Figure 1-8: Mid-frontal cutaways from a healthy (left) and osteoporotic (right) human femurs showing the distribution of maximum principal strains as predicted by linear, elastic finite element analysis [63].	19
Figure 2-1: Projection of a 1-mm-thick mid-frontal section of the proximal femur, showing the cortical (red) and trabecular bone (gray) identified using a ray-based search algorithm (see text).	27
Figure 2-2: Boundary conditions used in finite element analysis to simulate: a) a sideways fall, and b) stance loading. A force of 4,000 N was applied to the femoral head, the resultant directed towards the center of the femoral head. Component analysis of one randomly chosen proximal femur for: c) a sideways fall, and d) stance loading. F: overall loading (4,000 N). F _A : axial component and F _T : transverse component.	28
Figure 2-3: The variation in the fraction of total frontal-plane bending moment carried by the cortical bone for: a) a sideways fall, and b) stance loading. The vertical dotted line demarcates the load-sharing and load-transfer regions in the femoral neck. Error bars represent standard deviations from the mean values (for n=18 bones).	29
Figure 2-4: The variation in the distribution of tissue-level axial stress across the femoral neck cross-sections, for sideways fall and stance loading, in a single femur. S: Superior, P: Posterior, A: Anterior, I: Inferior.	30
Figure 2-5: The variation in the distribution of von Mises stress across the femoral neck cross-sections in the distal neck, for sideways fall and stance loading, across six bones randomly chosen for our cohort of 18 femurs. S: Superior, P: Posterior, A: Anterior, I: Inferior. Strength values are shown from non-linear finite element modeling, for fall and stance loading (performed as part of a different study [45], which is presented in the next chapter in this dissertation).	31

Figure 3-1: Projection of a 1 mm-thick mid-frontal slice of the proximal femur, showing the cortical (light gray) and trabecular bone (dark gray). The neck and trochanteric regions of interest are shown, which were used in prediction of fracture type (see text).....	42
Figure 3-2: Boundary conditions used in finite element analysis to simulate a sideways fall: A) the femoral diaphysis axis is set to an angle of 10° with respect to the horizontal, and B) the femur is internally rotated by an angle of 15°.....	43
Figure 3-3: A) Association between finite element-predicted femoral strength and the experimental measurements from biomechanical testing ($Y = 1.02 X - 0.15$, $R^2 = 0.94$, $p < 0.0001$). B) Estimation of fracture type (neck vs. trochanteric) by the finite element analysis. The fracture types observed during biomechanical testing are denoted by <i>N</i> for a neck fracture and <i>T</i> for a trochanteric fracture.....	44
Figure 3-4: Mid-frontal projected 0.615 mm-thick sections from the human proximal femur showing the distribution of failed tissues (Red : tensile failure; Blue : compressive failure) at the structure-level 0.2%-offset yield point for each femur. The femurs are arranged in the order of increasing femoral strength, from the top left to the bottom right corners. Femoral strength and the proportion of failed tissue are given; the letters <i>N</i> and <i>T</i> denote if the experimentally observed fracture type was neck (N) or trochanteric (T). There is generally less failed tissue per unit bone mass for the weaker femurs, indicative of diminished structural redundancy. The reader is referred to the online article for the corresponding animations of the deforming microstructure.....	45
Figure 3-5: Ratio of the amounts of failed tissue in the trabecular to cortical bone, averaged over all 12 femurs, vs. femoral strain. Femoral strain is the overall strain of the femur, normalized by the structure-level 0.2%-offset yield strain. Error bars represent the 95% confidence intervals.....	46
Figure 3-6: Tissue failure in the cortical versus trabecular bone: A) the proportion of overall failed tissue (as a percentage of the total amount of bone tissue) vs. experimentally-measured femoral strength ($p < 0.0001$, for all). B) ratio of the amounts of failed tissue in the trabecular to cortical bone, vs. experimentally-measured femoral strength ($R^2 = 0.67$, $p < 0.01$).....	47
Figure 3-7: A) Variation in the femoral neck aBMD (from DXA) and the ratio of trabecular-to-cortical bone volume in the femoral neck, versus the measured femoral strength ($p < 0.01$, for both). B) Variation in the percent change in stiffness at 0.1% bone tissue failure — a quantitative measure of structural redundancy (a larger change in stiffness being indicative of less structural redundancy) — and the ratio of trabecular-to-cortical bone volume in the femoral neck, versus the femoral neck aBMD. The squared data denote one specimen that had a high femoral neck aBMD but low strength.....	48
Figure 4-1: Material models depicting the stress-strain response at the tissue-level for: A) fully brittle, and B) fully ductile bone tissue.....	57
Figure 4-2: An example of a typical apparent-level stress-strain curve for trabecular bone corresponding to the fully ductile and fully brittle tissue-level behaviors, computed from the finite element analyses. For the ductile analysis, a 0.2%-offset criterion was used to define the apparent strength. For the brittle analysis, a 0.2%-offset criterion was not used because it exceeded the ultimate strain and thus an ultimate stress was used. The general shape of these curves did not depend on bone volume fraction.....	58

Figure 4-3: The variation in the proportion of failed tissue with bone volume fraction for brittle and ductile tissue-level behaviors.	59
Figure 4-4: The spatial distribution of the failed tissue at the apparent-level strength for fully brittle and fully ductile behaviors for three different specimens: A) low bone volume fraction (6.2%); B) medium bone volume fraction (17.3%); and C) high bone volume fraction (28.2%). Blue: tissue failure in compressive mode; Red: tissue failure in tensile mode.....	60
Figure 4-5: The ratio of the volume of failed tissue in tension to the volume of failed tissue in compression (at the apparent-level failure point) plotted versus the bone volume fraction, for the brittle and ductile behaviors. For brittle behavior, the ratio was greater than one for almost all specimens, reflecting a dominance of tensile failure mode at the tissue level. For ductile behavior, the ratio was less than one for most specimens, reflecting a dominance of compressive failure mode at the tissue level, particularly at bone volume fraction (>20%).	61
Figure 4-6: The variation in the apparent-level failure strain vs. bone volume fraction for simulated fully ductile ($R^2=0.54$) and fully brittle ($R^2=0.68$) behaviors from finite element analysis, and for real specimens from mechanical testing ($R^2=0.77$).	62
Figure 5-1: Material models depicting the stress–strain response at the tissue-level for: a) fully brittle, and b) fully ductile bone tissue.....	73
Figure 5-2: Boundary conditions used in finite element analysis to simulate: a) a sideways fall of the femur, b) stance loading of the femur, and c) uniaxial compression loading of the vertebra.	74
Figure 5-3: An example of a typical apparent-level stress–strain curve for trabecular bone corresponding to the fully ductile and fully brittle tissue-level behaviors, computed from the finite element analyses. For the ductile analysis, a 0.2%-offset criterion was used to define the apparent strength. For the brittle analysis, a 0.2%-offset criterion was not used because it exceeded the ultimate strain and thus an ultimate stress was used. The general shape of these curves did not depend on the anatomic site or loading configuration.	75
Figure 5-4: Variation in the ratio of whole-bone brittle to ductile strength across the specimens. The ratio was relatively uniform across all specimens but at the hip was larger for fall than stance loading. The specimens spanned a wide range in ductile (and brittle) strength indicating substantial heterogeneity in the bone external geometry and internal microstructure across the cohort.	76
Figure 5-5: Variation in the total proportion of failed tissue when the tissue-level behavior is changed from fully ductile (D) to fully brittle (B): a) the contributions of cortical and trabecular tissue failure have been shown separately; b) the contributions of tensile and compressive tissue failure have been shown separately. In all cases, the total amount of failed tissue was much less for fully brittle behavior. Bars show 95% confidence interval.	77
Figure 5-6: Mid-frontal sections of one proximal femur and mid-sagittal sections of one vertebra. (Colors depict locations of tissue-level failure. Blue: Compression. Red: Tension. Grey: No Failure). The amount of tissue-level failure (shown in %) required for overall bone failure was 5 to 10 times lower when the bone tissue was assumed to be fully brittle (bottom row) versus fully ductile (top row). Bone strength values are shown in Newton, N.	78

Figure 6-1: Boundary conditions used in finite element analysis to simulate a sideways fall. The femoral diaphysis axis is set to an angle of 10° with respect to the horizontal (left), and the femur is internally rotated by an angle of 15° (right). 87

Figure 6-2: Material model depicting the stress–strain response at the tissue-level for both the cortical and trabecular tissue. E_{ult} represents the tissue-level ultimate strain. It was assumed same in tension and compression, and was different for the cortical vs. trabecular tissue. Y represents the tissue-level yield point and F represents tissue-level ultimate point. 88

Figure 6-3: Variation in the femoral strength on simultaneously altering the trabecular and cortical tissue-level ultimate strains by ± 1 SD about their mean values. 89

Figure 6-4: Variation in the femoral strength on altering a) only the cortical tissue-level ultimate strain by ± 1 SD, b) only the trabecular tissue-level ultimate strain by ± 1 SD and ± 2 SD. * represents the values of trabecular tissue ultimate strains that were simulated for only one femur. 90

Figure 6-5: Variation in the relative proportion of yielded to failed tissue in the bone when a) both the cortical and trabecular tissue-level ultimate strains are simultaneously varied by ± 1 SD, b) only the trabecular tissue-level ultimate strain is varied by ± 1 SD and ± 2 SD. * represents the value of trabecular tissue ultimate strains that were simulated for only one femur. 91

Figure 6-6: Variation in the total proportion of tissue-level failure when a) only the cortical tissue-level ultimate strain is varied by ± 1 SD, keeping the trabecular tissue ultimate strain fixed at its mean (8.8%), b) only the trabecular tissue-level ultimate strain is varied by ± 1 SD and ± 2 SD keeping the cortical tissue ultimate strain fixed at its mean (2.2%). * represents the values of trabecular tissue ultimate strains that was simulated for only one femur. 92

LIST OF TABLES

Table 3-1: Characteristics of the study population (mean, standard deviation) and correlation coefficients between selected outcomes and various predictor variables.....	39
Table 3-2: Correlation analysis on the residuals of the linear regression between the femoral strength (from experiment) and femoral neck aBMD (from DXA), versus selected variables. Positive or negative coefficients indicate that a low or high value, respectively, in the variable is associated with a negative residual, namely, a low strength with respect to the aBMD.....	41
Table 4-1: Specimen details for the final cohort.....	55
Table 4-2: The influence of variation in tissue-level strength asymmetry (<i>C</i>) on the ratio of brittle to ductile strength as predicted by both cellular solid theory and finite element analysis (n=3 specimens; BV/TV = 8.8%, 17.2%, 26.8%).....	56
Table 5-1: Characteristics of the study population (mean, standard deviation) for the femurs (n=16) and correlation coefficients between selected outcomes and the brittle-to-ductile strength, both for a sideways fall and stance loading of the femurs.	71
Table 5-2: Characteristics of the study population (mean, standard deviation) for the vertebrae (n=12) and correlation coefficients between selected outcomes and the brittle-to-ductile strength for uniaxial compression loading of the vertebra.....	72
Table 6-1: The combinations of tissue-level ultimate strains that were simulated.	86

ACKNOWLEDGEMENTS

I would like to express my gratitude towards my research adviser, Prof. Tony Keaveny, for mentoring me during my graduate career. He has played a major role in helping me grow as a researcher. His insightful comments on my work, and his enthusiasm for research, have been highly beneficial for this dissertation work.

I am grateful to Professors Lisa Pruitt and Jon Wilkening for serving on my qualifying exam and dissertation committee. Thanks to Prof. Mary Bouxsein (BIDMS), for providing me with cadaver bones analyzed in this dissertation. Thanks to Prof. Grace O’Connell for providing me the opportunity of learning cell culture in her laboratory. Thanks also to Bonnie Kirk and Jean Lin-Wong for providing administrative support.

I would like to thank all the past and present members of OBL, for creating a fun and collaborative atmosphere. I owe a great deal of thanks to Aaron Fields, Sarah Easley, and Arnav Sanyal for helping me get started with my academic life at Berkeley. The afternoon coffee-time discussions with Arnav were always interesting and thought provoking. Several undergraduate students — Kevin, Hosna, Bich, Nasim, Suraj, Divya, and Haley — assisted me with various aspects of finite element analysis, and it was a pleasure getting to know them and working with them. Thanks also to Haisheng, Jérôme, Frédéric, Annika, Saghi, Alex, and Megan, for the happy times that we spent working together in the laboratory.

On the personal front, life in Berkeley wouldn’t have been so special without friends! I found two really amazing friends in Deepan and Ajay. Our dinner-time conversations and weekend trips will forever be some of my best memories of Berkeley. I couldn’t have asked for better housemates than Varun and Saurabh. They were always cooperative, and maintained a homely atmosphere in our house. Varun’s calm demeanor and Saurabh’s chirpy attitude will be greatly missed. I will forever cherish my friendship with Rahul, Narayanan, and Mohit, who made me feel at home in Berkeley when I arrived, and have been close friends ever since. Thanks also to all the friendly folks on Euclid Avenue, especially Java and Jamal from Humming Bird and Eric from Brewed Awakenings, for their smiling faces.

Last, but most importantly, I would like to express my gratitude towards my parents, for their unconditional love and support. Without my mom’s prayers and sacrifices, I wouldn’t have come this far in my life. My father has always been there whenever I needed him, sometimes even at the cost of his own professional goals. His hard-working nature has always inspired me, especially during hard times. Talking to my grandparents on the phone every week was always refreshing and comforting. To my wife, Pallavi, who I met at Berkeley — you have had a very positive influence on my life, and I wish for our long, loving, and prosperous life together.

1. INTRODUCTION

The skeleton is essential for terrestrial animal life, and human beings have evolved both light enough to allow rapid mobility and strong enough to avoid disabling fractures during the reproductive years. However, after the menopause in women and with advancing age in men, bone mass declines and the risk of fractures increases [1-3]. Osteoporosis — defined as a skeletal disorder characterized by compromised bone strength predisposing to an increased risk of fracture — is a major public health problem throughout the world [4, 5]. Currently affecting more than 10 million people in the US, osteoporosis is projected to impact approximately 14 million adults over the age of 50 by the year 2020 [6]. The annual incidence of osteoporotic fractures exceeds 1.5 million in the US and costs the federal health care system approximately \$17 billion annually [7, 8]. These direct medical costs represent a greater burden than the projected annual costs of stroke, breast cancer, diabetes, or chronic lung disease [9].

Of the various types of osteoporotic fractures, hip fractures have long been considered to be the most devastating (**Figure 1-1**). Their incidence rates are known to increase exponentially with age in both women and men in most regions of the world [10-12]. Notably, 1 in 5 individuals die during the first year after a hip fracture, whereas nearly one third require nursing home placement after hospital discharge, and less than one third regain their pre-fracture level of physical function [13]. Thus, it is evident that, in addition to the direct costs associated with hip fractures, the indirect cost — the costs associated with fracture-related morbidity and mortality — are also substantial [14, 15]. Clearly, the clinical and economic consequences of osteoporosis call for a concerted effort to assess patients at risk to allow for prevention and early intervention when appropriate.

Given the serious nature of hip fracture outcomes, identifying individuals who are at high risk of fracture becomes imperative. The current clinical standard for osteoporosis diagnosis uses Dual energy X-ray absorptiometry (DXA) [16, 17]. As per the World Health Organization (WHO) guidelines [18], patients are classified as being osteoporotic when they have a areal bone mineral density (aBMD) — measured by DXA — that is 2.5 standard deviations (SD) below that of the optimal peak aBMD of a healthy young adult of the same sex. This is equivalent to having a T-score ≤ -2.5 , where T-score is calculated as the person's aBMD normalized by the aBMD of a young healthy adult of the same sex. However, it has been recently reported in the Rotterdam study — a 7-year average follow-up on over 7,000 participants — that only 44% of women and 21% of men presenting with non-vertebral osteoporotic fractures had T-scores of less than -2.5 [19]. Therefore, if only individuals with T-scores of less than -2.5 were to be treated for osteoporosis — as is followed in the current medical practice — more than 50% of those who eventually fracture would remain unidentified, and thus untreated. Thus, there exists an immediate need to move beyond the existing paradigm of osteoporosis diagnosis — the DXA-derived aBMD — so as to improve fracture risk predictions.

The fundamental issue that hinders further improvement in the hip fracture risk assessment is a lack of clear understanding of the influence of “bone quality” on bone fragility [20-22]. Bone quality generally refers to the effects of skeletal factors that contribute to bone strength but are not accounted for by measures of “bone quantity” such as the bone mass and aBMD. Because a clinical fracture is ultimately a mechanical event, any clinically relevant

modification of bone quality must change bone biomechanical performance independent of bone quantity. Of the several risk factors that could be categorized as being under the realm of bone quality, microstructure and tissue-level failure properties are considered to be of utmost importance from a biomechanical standpoint [23, 24], since they are understood to vary substantially across individuals and with aging [25-27], diseases [28], and treatments. Consequently, a number of key questions remain unanswered. What are the relative roles of various femoral compartments in the overall biomechanics of the proximal femur? What are the microstructural failure mechanisms in the femur and how do they influence hip fragility? How does the tissue-level failure behavior influence the structure-level behavior of bones?

To address these issues, the primary focus of this dissertation is on improving the current understanding of the micromechanics of the human proximal femur. Specifically, the aim is to elucidate the biomechanical mechanisms underlying the strength behavior of the femurs so as to gain insight into the etiology of hip fractures. Such an understanding is not only key to improving the femoral strength predictions and fracture risk assessment, but is also required to demonstrate the effects of aging and disease on the bone strength.

The remainder of this chapter will establish a foundation in the whole-proximal femur biomechanics, which will be useful in understanding the material presented in the subsequent chapters of this dissertation. First, the structure and composition of bone will be briefly summarized, followed by detailed discussions of the anatomy and mechanical behavior of the human femur. Next, a short section summarizing human bone tissue-level ductility measurements reported in the literature will be presented. The fifth section will address contemporary issues regarding computational modeling of whole bones such as the proximal femur and vertebral body. The final section contains an outline of the objectives and scope of this dissertation.

1.1 Structure and composition of bone[‡]

Bone structure is woven at many dimensional scales into an architectural masterpiece of biomechanical engineering (**Figure 1-2**) with an optimal mass adapted in size, shape, and architecture, which enables it to perform diverse mechanical, biological, and chemical functions, such as structural support, protection and storage of healing cells, and mineral ion homeostasis. In order to understand the mechanical properties of bone, it is important to understand the mechanical properties of its component phases, and the structural relationship between them at the various levels of hierarchical structural organization [30]. This hierarchically-organized structure has an irregular—yet optimized—arrangement and orientation of the components, making the material of bone heterogeneous and anisotropic [31].

Hierarchical Structure: By weight, the constituent materials of bone are inorganic ceramic materials (primarily hydroxyapatite, 60%), organic materials (primarily type-I collagen, 30%), and water (10%). At the smallest size-scale, the hydroxyapatite crystals may resemble small plate-like structures ($\sim 5 \times 15 \times 40$ nm). These crystals are surrounded by woven collagen fibrils

[‡] Portions of this section were adapted in part from [29].

(~30 nm in diameter \times 300 nm in length). At the next size-scale (~10 μ m), the mineralized collagen fibrils are arranged in one of two forms. In the first form, the fibrils randomly orient to form a structure often termed woven bone. In the second form, the fibrils assemble into sheets called lamellae, which then stack together in layers with alternating fiber angles between layers.

Lamellae are arranged in five different structures at the next size scale: 1) Trabecular bone, a highly porous structure (>60% porous in humans) is made of an organized lattice of lamellar packets. Trabecular bone occupies the ends of the long bones and the vertebral centrum; the trabecular lattice resembles an interconnected network of rod-like and plate-like struts with substantial variability across anatomic sites and species (**Figure 1-3**). Trabecular thickness is variable, but generally ranges between ~100-250 μ m; 2) Osteonal or Haversian bone consists of 10-15 lamellae arranged in concentric cylinders (~200 μ m in diameter \times 2 mm in length) about a central Haversian canal. These canals contain blood vessels, capillaries, nerves, and bone cells. The substructure of the concentric lamellae is termed an osteon. Osteons are the primary discrete units of human cortical bone; 3) Primary lamellar bone is wrapped circumferentially in a 2-3 mm layer around the diaphysis of long bones such as the femur and tibia; 4) Woven bone is found in areas of rapid growth such as at locations of fracture; and 5) Laminar bone consists of a series of concentric laminae (each laminae is ~0.1-0.2 mm thick) around a marrow cavity. Sandwiched between adjacent laminae is a two-dimensional network of blood vessels.

Cortical Vs. Trabecular Bone: Bone is characterized as cortical or trabecular bone depending on its level of porosity (**Figure 1-4**). Cortical bone has porosity of 35% or less [32-34]—the porosity is generally greater in femur than in vertebra. It is found in the diaphysis of long bones and flat, irregular bones such as the sternum and pelvis. Trabecular bone has porosity of 60-95%, depending on the anatomic site [35, 36] and is found at the ends of long bones such as the femur and within cuboidal bones such as the vertebral bodies of the spine. Trabecular bone supports the articular surfaces of the joints, transfers joint and muscle loads to long bone shafts and plays a role in energy absorption. Other functions of trabecular bone include hematopoiesis (production of red blood cells) and calcium storage.

The underlying bone tissue that forms trabecular and cortical bone is very similar, being made of lamellar bone arranged as previously described for cortical bone or in the more irregular shaped packets for trabecular bone. Differences also arise from the manner in which the two types of bone are remodeled. Remodeling in trabecular bone occurs at the free surfaces of the rods and plates, which is greater than on the internal surfaces of the Haversian canals within cortical bone [22]. As a result, trabecular bone is less mineralized than cortical bone, although the difference is subtle. This difference in mineralization and the different arrangements of the lamellar bone are thought to produce slightly lower material properties of the trabecular tissue compared with the cortical tissue [37].

Structural Adaptation: Bone is a remarkable material, able to adapt to a changing mechanical environment and replace old or damaged tissue through bone modeling and remodeling [38]. At the cellular level, this process is carefully orchestrated through the resorption of existing bone matrix by osteoclasts and the formation of newly mineralized material by osteoblasts [39]. Remodeling also results in constant fluctuations in local levels of tissue mineralization and in overall bone mass [40]. Imbalance between the resorption and

formation phases of the remodeling process due to aging and disease—such as osteoporosis—are thought to cause a net bone loss [41]. Osteocytes—cells that reside in lacunae (5-8 μ m diameter) within and between lamellar packets—are believed to play a role in monitoring mechanical stimuli and tissue damage, recruiting osteoclasts and osteoblasts to respond with appropriate adaptive responses [42]. The precise mechanisms through which osteocytes sense mechanical stimuli and regulate the functions of osteoclasts and osteoblasts are still being investigated [43, 44].

1.2 Anatomy of the proximal femur

The femur is the only bone in the thigh and is categorized as a long bone. It comprises of the diaphysis and two epiphysis or extremities that articulate with adjacent bones in the hip and knee. The upper or proximal extremity of the femur (close to the torso) is called the “proximal femur”. The principal structural components of the proximal femur are the femoral head, neck, and trochanter (**Figure 1-4**). In this dissertation, the main focus is on understanding the micromechanics of the proximal femur, which is not only the most geometrically and morphologically complicated region within the femur, but is also most susceptible to fragility fractures.

The cortical bone (cortex) forms the periphery of the proximal femur (**Figure 1-4**). By weight, the cortex amounts to ~40-60% of the bone tissue in the proximal femur [45]. The two important measures of cortical bone morphology are its thickness (width) and porosity. Within the femoral neck, the cortical width varies markedly as we traverse from the inferior to the superior aspect of the bone [46, 47] — it is generally thickest at the inferior aspect (~2-4 mm thick) and thinnest at the superior-posterior aspect (~0.2-0.5 mm thick). There are also regional differences in the porosity within the femoral neck cortex. In general, inferior cortex is less porous (~6-11% porosity) than the superior cortex (~12-18% porosity), although the porosity gradient between these two locations may differ between men and women. Also, the anterior cortex is 40% more porous in osteoporotic cases compared to healthy individuals [33, 48]. The shape of femoral neck cross-section varies considerably along the length of the femoral neck. Adjacent to the shaft the neck is elliptical in shape, with the longest diameter in the superior–inferior direction, whereas, near the femoral head, it is more circular and largely trabecular [49]. These differences in shape might be a consequence of structural adaptations to external loading. While there is some evidence that both cortical width and porosity might be key structural determinants of hip fragility [50], little has been done to clearly demonstrate their relationship with femoral strength [51].

The trabecular bone is located in the interior of the proximal femur and forms the core of the bone (**Figure 1-3**). The volume fraction of trabeculae (the fraction of total volume occupied by trabecular tissue) varies with anatomic location in the bone [35, 36]. It is generally highest in the femoral head (~30-60%) and lowest in the greater trochanter (~5-15%), with a substantial variation observed in the neck (~15-40%). A key determinant of the trabecular bone quality that varies considerably, both within and across the femurs, is the trabecular microarchitecture. The term “microarchitecture” in the context of trabecular bone broadly refers to the spatial arrangement and interconnection of individual trabeculae. Several parameters that have been developed to describe various aspects of trabecular microarchitecture are listed below. In

Chapter 4, the role of microarchitectural parameters in the relationship between tissue-level ductility and apparent-level trabecular bone strength has been investigated.

Microarchitecture parameters: Trabecular thickness (Tb.Th): the average thickness of a trabecular object, trabecular separation (Tb.Sp): average thickness of a pore space, trabecular number (Tb.N): average number of times per unit length that any random line drawn through the volume of interest intersects a trabecular object, structure model index (SMI): quantifies the structural appearance of trabecular bone by relating the convexity of the structure to a type of model [35]. Flat, plate-like structures have an SMI of zero and ideal cylindrical rods have an SMI of three, connectivity density (Conn.D): defined per unit volume and is related to the maximal number of branches that can be broken before a structure is separated into two parts [52], and degree of anisotropy (DA): quantifies the presence or absence of preferential alignment along a particular directional axis. A perfectly isotropic structure has a DA of one and increasing values of DA represent increasing degrees of anisotropy. All of the microarchitecture measures presented in this dissertation will be evaluated using the three-dimensional distance transformation approach, *i.e.* the so-called “direct approach” [53]. This approach makes no *a priori* assumptions about the structure type of the trabeculae.

1.3 Mechanical behavior of the proximal femur

The most common serious injury associated with the fall of an elderly person is a hip fracture. Over 90% of the hip fractures are a result of fall on the greater trochanter but only 1-2% of all falls of the elderly lead to a hip fracture [54]. Clinically, hip fractures can be classified into two main groups (**Figure 1-5**), cervical (neck) and trochanteric fractures, and it has been widely suggested that these two fracture types have different risk factors and different fracture mechanisms [55, 56]. Understanding why and how failure occurs at different anatomic locations within the proximal femur — neck versus trochanter — is fundamental to acquire mechanistic insight into the etiology of hip fractures.

Substantial changes occur in the proximal femur with aging (**Figure 1-6**). Decline in bone mass coupled with deterioration in microarchitecture and tissue-level material properties are thought to be the primary causes of decreases in femoral strength. A recent clinical investigation has reported that, between the ages 20 to 90, the femoral strength decreases by about 55% in women and 39% in men, with notable declines starting in the mid-40s for women and a decade later for men [57]. In the same age span, femoral neck aBMD — a strong predictor of femoral strength [58, 59] — also follows a similar trend; however, in comparison to the femoral strength, it only decreases by 26% in women and 21% in men. Since aBMD fails to completely explain these age-related variations in the femoral strength, it is quite evident that bone microstructure and/or tissue-level material behavior also exacerbate with aging and lead to greater increase in hip fragility than what is predicted by aBMD alone. This issue clearly underscores the importance of investigating the role of bone microstructure — and the interaction between cortical and trabecular compartments — during structure-level failure of the femur.

The structural role of cortical bone in the femoral strength is a fundamental but poorly researched topic in bone biomechanics. There is some evidence both from cadaver and clinical studies that, cortical bone morphology [60] and trabecular bone density [61], as measured with quantitative computed tomography (QCT), are strongly associated with femoral strength. However, the relative contribution of the cortical and trabecular compartments to femoral strength still remains a contentious issue. Finite element analysis of the femur models constructed using clinical-resolution CT scans has suggested that cortical bone supports approximately 50% of the load at the mid-neck and 96% of the load at the base of the neck during both normal gait and sideways fall on the greater trochanter [62]. However, these computational models, typically overestimate cortical thickness and cannot directly capture cortical porosity, thus possessing limited fidelity in terms of how the thin cortical shell is modeled. Recent advances in micro-CT imaging and high-resolution finite element modeling of the whole-proximal femurs [45, 63, 64] has provided a reliable means to develop more mechanistically correct models. However, the studies to date have only been exploratory in nature since they have analyzed just one or two human femurs [63, 64], making it difficult to generalize their findings. Given different pharmacological interventions impact the cortical and trabecular morphology differently, quantifying the cortical-trabecular load sharing in the femur is therefore considered highly relevant from a clinical viewpoint.

Understanding the influence of tissue-level ductility — the ability of bone tissue to deform prior to its fracture — on the overall bone strength is an outstanding biomechanical issue. Addressing this issue is central to improving our current understanding of the role of bone quality in the etiology of age-related hip fractures. In doing so, it might also be potentially important to consider the distinction between cortical versus trabecular ductility. Cortical tissue becomes less ductile with aging [25], but no one has ever directly linked such changes to reductions in whole-bone strength. Interestingly, some recent experiments have suggested that trabecular tissue has much greater ductility than cortical tissue but that trabecular ductility does not change with age. This raises the possibility that whole-bone strength may be more influenced by ductility changes in the cortical tissue than in the trabecular tissue. The relative effects of cortical vs. trabecular ductility will also depend on what type of tissue typically fails first when the overall bone is overloaded. Those internal failure characteristics might be different for the femur versus vertebral body, will depend on loading conditions, and may be different across different bones at any given anatomic site or loading depending on cortical-trabecular load sharing and trabecular microarchitecture. Moreover, like cortical-tissue ductility, the effects of reductions in tissue-level ductility for trabecular tissue – or loss of it with aging or osteoporosis — on whole-bone strength has never been assessed. Clearly, further research addressing these issues is warranted to explore how the ductility-related variations in bone quality might impact hip fragility.

1.4 Tissue-level ductility for the human bone

The ductility of any material is a mechanical property that describes the extent to which the material can plastically deform prior to fracturing. It represents an important aspect of the material failure behavior, and primarily depends on the sub-microstructural or even lower-level organization of the material. In the context of bone, there is substantial evidence that the amount of collagen, and its molecular stability and cross-linking play an important role in influencing the

ductility of the bone tissue [65-69]. Since tissue-level ductility is a key determinant of bone quality, understanding its variations across individuals and with aging, diseases, or treatments is key to understanding the etiology of hip fractures. Further, the ability to determine subject-specific elastic, yield, and failure properties of the bone tissue is necessary for the estimation of bone strength using computational models [70]. Currently, the predictive power of high-resolution finite element models is partially limited by subject-specific variability in the tissue-level failure properties and the lack of tools capable of assessing tissue-level properties *in vivo*. It is therefore evident that new devices and techniques need to be developed to characterize tissue-level failure properties and to evaluate the variation in these properties across the population.

A number of studies have biomechanically tested individual trabeculae [71-73] and uniformly shaped (micro-machined) specimens [74, 75] derived from trabeculae to measure either elastic modulus or fatigue properties of the human trabecular bone tissue. However, to date, only a few studies [28, 76] have reported direct measurements of the ultimate strain of human trabecular bone tissue due to the technical challenges associated with performing failure testing on samples of individual trabecula that are about 0.5-2 mm in length and ~100-200 μm in diameter. Hernandez and colleagues [76] conducted the first investigation to determine the human trabecular tissue ultimate strain. They performed tensile testing on 221 specimens of individual trabeculae (vertical trabeculae extracted from vertebral bodies harvested from $n=32$ donors; ages 54-92 years; 4 to 9 trabeculae per donor) and demonstrated large and highly variable values of ultimate strain. On average, the ultimate strain was $8.8 \pm 3.7\%$ (mean \pm SD), ranged from 1.8% to 20.2% and showed considerable intra-individual variation. Ultimate strain was statistically similar in males ($8.5 \pm 3.6\%$) and females ($9.1 \pm 3.9\%$, $P = 0.39$); however, these experiments did not detect any relationship between donor age and ultimate strain.

More recently, Carretta and colleagues [28] developed and validated a novel three-point bending device, to test samples of single trabeculae in tension and bending modes. They only tested a total of 32 trabeculae ($n=2$ donors (1 osteoporotic and 1 healthy); ages 54-56), 16 trabeculae each in bending and tension, and reported high variability in the ultimate strain within each donor. It must be noted that, values of ultimate strain suggested by these investigators (healthy donor: $5.1 \pm 2.4\%$ in tension, $8.2 \pm 2.5\%$ in bending; osteoporotic donor: $2.4 \pm 0.9\%$ in tension, $6.1 \pm 2.6\%$ in bending) lie within the lower range of the values reported by Hernandez (1.8-20% in tension). For any testing mode, the ultimate strain was higher in the healthy donor, suggesting better bone quality compared to the osteoporotic bone. However, it still remains to be seen if higher tissue-level ductility in the healthy donor would translate to greater overall bone strength, and if so, what would be its overall impact on the strength.

McCalden and coauthors [25] performed tensile testing to failure on 235 cortical tissue specimens that had been machined from human cadavers ($n = 47$ donors; ages 20-102). They measured a tissue-level ultimate strain of $2.2 \pm 0.9\%$ and reported the ultimate strain to decline with age by 9% per decade. This study is the most comprehensive of all the studies performed on the cortical tissue and the value of ultimate strain reported here is quite consistent across the different studies conducted on this topic.

Clearly, there is substantial variation in the trabecular tissue ultimate strain both within and across the individuals. Various factors may explain the wide range of values reported in the literature, such as the varying test conditions (wet or dry), the boundary conditions and the device used. Nevertheless, there is no estimate with respect to the extent to which the ultimate properties are influenced by the test conditions, and therefore, it is difficult to estimate the ultimate strain in physiological conditions. Regardless, it seems — albeit from a very limited data — that trabecular tissue is much more ductile compared to the cortical tissue (**Figure 1-7**). In Chapter 6 of this dissertation, we have used the range of values suggested by Hernandez and McCalden as the basis to evaluate the influence of typical population-variations in cortical and trabecular tissue ductility on the femoral strength.

1.5 Computational modeling of the bone

Finite element analysis is a powerful computational tool for investigating the biomechanical behavior of bone. This technique allows investigators to perform “virtual” mechanical testing that has several advantages over gold-standard biomechanical testing in the laboratory. First, computer simulations are non-destructive in nature, so the effects of variables such as boundary conditions, external loading [77] or tissue-level material properties [78] can be evaluated in controlled, repeated measures-type parameter studies. Second, the technique can provide detailed insight into stress and strain distributions (**Figure 1-8**) within the bone [63, 79] whereas biomechanical testing only yields information about the structure-level mechanical behavior (or at best, about local stresses and strains on the surface of the bone using strain gauges [80, 81]). Perhaps the greatest benefit of computer modeling in bone mechanics research lies in combining the technique with biomechanical testing in order to leverage the individual strengths of each approach. In this manner, for example, researchers have gained substantial insight into tissue-level mechanical properties [37, 82] and failure mechanisms [45, 83, 84].

This dissertation reports on the use of high-resolution finite element modeling of whole proximal femurs. These finite element models are constructed from micro-CT images (61.5 microns voxel-element size) of the transverse sections of the proximal femurs using a voxel-based technique in which each voxel in the images is converted into an eight-node brick element (hexahedral element). Hence, the models implicitly capture the spatially heterogeneous trabecular microarchitecture and the cortical bone morphology (**Figure 1-4**). By accurately capturing the physics of these microstructures, the models can be used to understand the micromechanics of the proximal femur and to resolve issues such as the relative contributions of the cortical versus trabecular bone in the load-carrying capacity of the overall femur. In addition to addressing this issue, this dissertation also uses the high-resolution finite element models to elucidate the microstructural failure mechanisms in the trabecular and cortical bone, including how these failure mechanisms vary—both quantitatively and qualitatively—across individuals exhibiting a wide range of bone morphologies.

In contrast to continuum-level finite element models of the femur [85-87] that are constructed using quantitative-CT (QCT) images (1-3 mm voxel-element size) in which each element is assigned a different material property based on its CT-derived density, high-resolution finite element models typically use homogeneous and isotropic material properties. This enables separation of the effects of variations in microarchitecture from the effects of variations in

material properties. Additionally, apparent-level predictions of mechanical properties as well as tissue-level stress and strain distributions from high-resolution finite element models with homogeneous and isotropic material properties have correlated well with experimental measures providing some level of validation for this modeling approach [83, 88-91].

Computationally, high-resolution finite element modeling of the whole proximal femur requires both state-of-the-art software and hardware. In the past, high-resolution finite element models of trabecular bone have traditionally been solved with the iterative, element-by-element (EBE) preconditioned conjugate gradient (PCG) method [82, 88, 90, 92]. This method is memory efficient and the work per iteration and per degree of freedom is constant. However, because the number of iterations required to reduce the residual by a constant amount using the EBE-PCG method rises dramatically as the problem size increases, this method is inefficient for solving larger problems, such as those involving the whole vertebra. The models of whole proximal femurs typically contain up to 800 million degrees of freedom, and therefore, the analyses require more efficient solvers [93, 94] and substantial parallel computing capacity. By dividing the global finite element mesh into sub-domains and spreading the workload over thousands of processors that perform the computations in parallel, previously intractable problems can be solved in minutes. The work in this dissertation utilizes a highly-scalable, implicit finite element framework (*Olympus* [93]) implemented on some of the world's fastest and most advanced parallel supercomputers. In particular, the work utilizes implementations of *Olympus* on two supercomputing platforms: 1) a Sun Constellation cluster with 62,976 processors and 123 TB of memory (Ranger; Texas Advanced Computing Center, Austin, TX USA); and 2) a Dell Power Edge C8220 cluster with 102,400 dual 8-core Intel Xeon E5-2680 processors and 270 TB of memory (Stampede; Texas Advanced Computing Center, Austin, TX USA).

In addition to their large size, high-resolution finite element models of whole proximal femurs represent a significant computational challenge due to their numerical complexity. For example, performing fully nonlinear analysis involves both material and geometric nonlinearities. Material nonlinearities are necessary in order to capture the tension-compression strength asymmetry of the bone tissue [91, 95]. Geometric nonlinearities—which involve updating the stiffness matrix based on changes to the orientation of the structure—are required to capture the deformation mechanisms such as large-deformation bending and buckling [83, 96]. Due to the computational challenge of simulating these nonlinearities, past studies on whole femurs have focused only on *linear* analysis. However, recent advances in supercomputing technology combined with efficient solver algorithms [93] have finally made it possible to perform fully *nonlinear*, high-resolution finite element analysis of whole vertebrae. Chapters two through five of this dissertation are devoted to such analyses—the first of their kind for whole bones— and in particular, to understanding how the failure mechanisms in the human femurs subjected to a sideways fall or gait loading depend on bone microstructure and tissue-level failure behavior.

1.6 Objectives and scope

The overall goal of this dissertation is to study the micromechanics of the human proximal femur with the aim of enhancing current understanding of the etiology of hip fractures. Toward this goal, the first objective is to study the interaction between the cortical and trabecular compartments in the femur so as to determine their relative importance in maintaining structural integrity. In addition, biomechanical mechanisms that dictate the strength behavior of femurs will also be elucidated with special focus on identifying morphological measures that might enhance fracture risk prediction beyond the currently used gold-standard, aBMD. The second objective is to understand the relationship between tissue-level ductility — a key determinant of bone quality — and whole-bone strength. It is well appreciated that ability of the bone tissue to deform might deteriorate with aging, disease, or treatments but currently there is very little understanding of how such variations in tissue-level failure behavior influence the whole-bone failure behavior.

Chapter two estimates the relative contributions of the cortical and trabecular bone to load-carrying capacity of the femoral neck. Using linear elastic finite element analysis, the axial and bending load-sharing in the femoral neck is quantified and the associated spatial distributions of stress within the femoral neck is demonstrated, both for a sideways fall and stance loading of the femur.

Chapter three elucidates the microstructural failure mechanisms in the human femurs during a sideways fall impact and seeks to identify microstructural measures that enhance fracture risk assessment beyond the DXA-derived bone mineral density. Using a combined experimental and computational approach, this work provides direct validation of the whole-proximal femur finite element models used in this dissertation. Owing to the numerical complexity of simulating both geometric and material nonlinearities in high-resolution finite element models of whole bones (300-800 million degrees of freedom), characterizing the failure mechanisms in this manner represents a significant challenge in the field of computational bone mechanics. Indeed, the nonlinear, high-resolution finite element analyses in this chapter are the first of their kind for whole femurs, and are examples of some of the biggest non-military applications of finite element analysis.

The first ever investigation that aimed at understanding the influence of tissue-level ductility on the trabecular bone strength has been presented in Chapter four. Since the trabecular tissue ultimate strain spans a wide range both within and across the individuals, we simulate two hypothetical cases of fully brittle and fully ductile tissue-level behaviors so as to derive theoretical bounds on the apparent-level strength of trabecular bone. To justify the finite element-estimated outcomes, this study also uses cellular solid analysis.

In Chapter five, the effect of tissue-level ductility on the structure-level failure behavior of the femurs and vertebra is studied. This study also investigates which factors — the bone geometry, morphology, or the nature of external loading — regulate the role of tissue-level ductility on whole-bone strength.

Chapter six explores the influence of typical population-variations in the cortical and trabecular tissue-level ductility on femoral strength with a special focus on understanding

whether such variations in ductility are more influential for the cortical or trabecular bone. By simulating multiple combinations of cortical and trabecular tissue-level ultimate strains for each femur, this study provides insight on how the variations in femoral strength due, in specific, to variations in tissue-level ductility compare with typical across-population variations in femoral strength. That is, how important is role of tissue-level ductility in the femoral strength compared to the roles of bone mass and microstructure.

Finally, Chapter seven provides concluding remarks and suggests future directions of research. The primary novelty of this work is its use of massively parallel, nonlinear, micro-CT-based finite element modeling, incorporating latest advances in the quantitative imaging technology. In Chapters four through six, computer simulations make it feasible to understand the influence of tissue-level ductility on whole-bone strength in a highly controlled, pairwise manner, which is not possible to with mechanical testing alone.

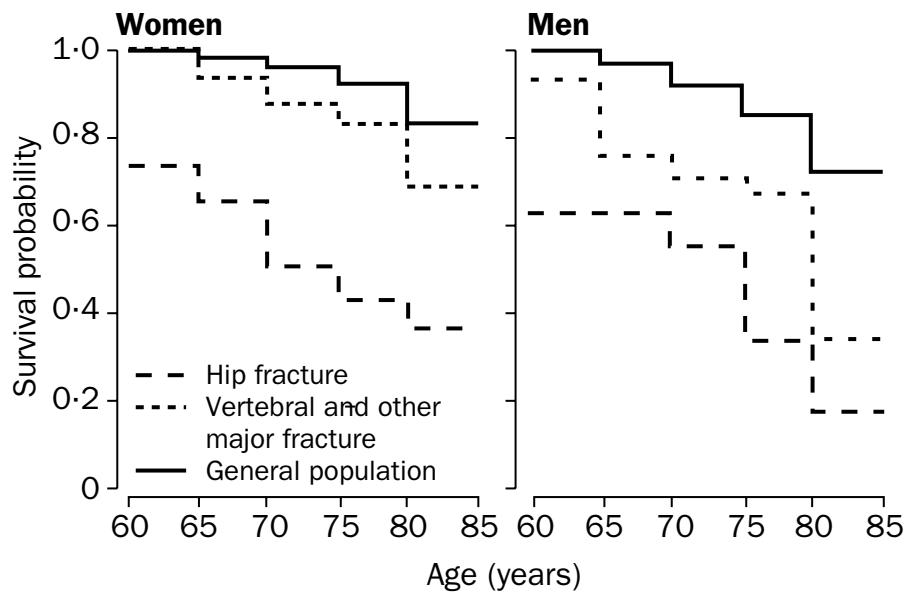


Figure 1-1: Cumulative survival probability by sex and type of fracture [4].

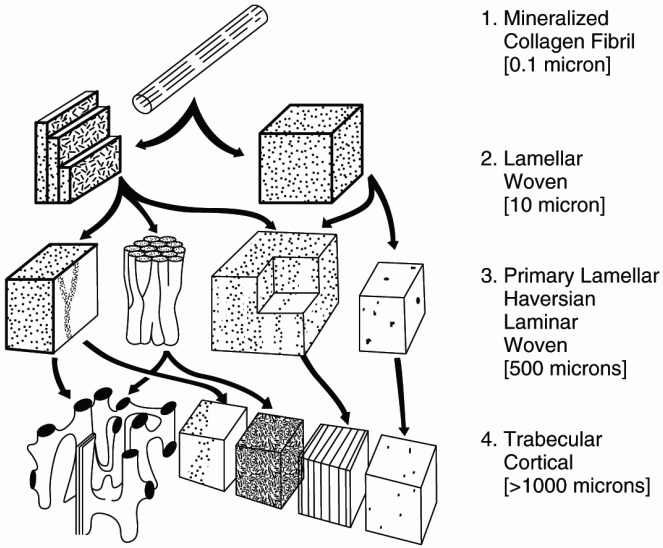


Figure 1-2: Hierarchical structures of bone from the sub-micron length scale to the millimeter length scale [29].

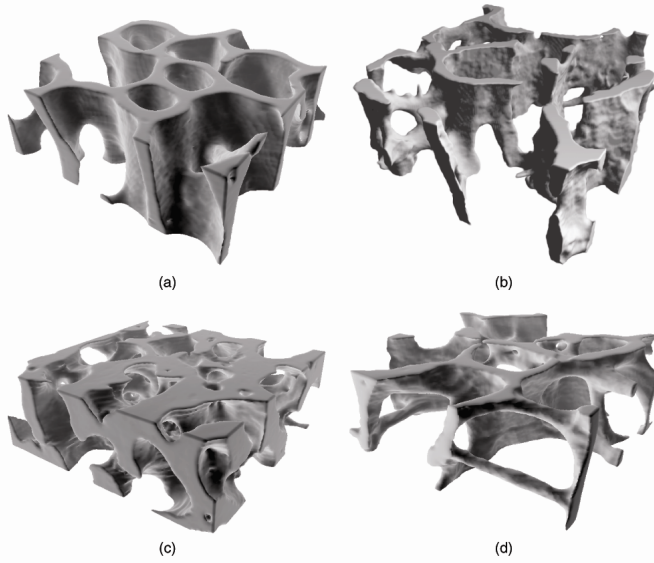


Figure 1-3: High-resolution renderings of trabecular bone from: a) bovine proximal tibia; b) human proximal tibia; c) human femoral neck; d) human vertebra [97].

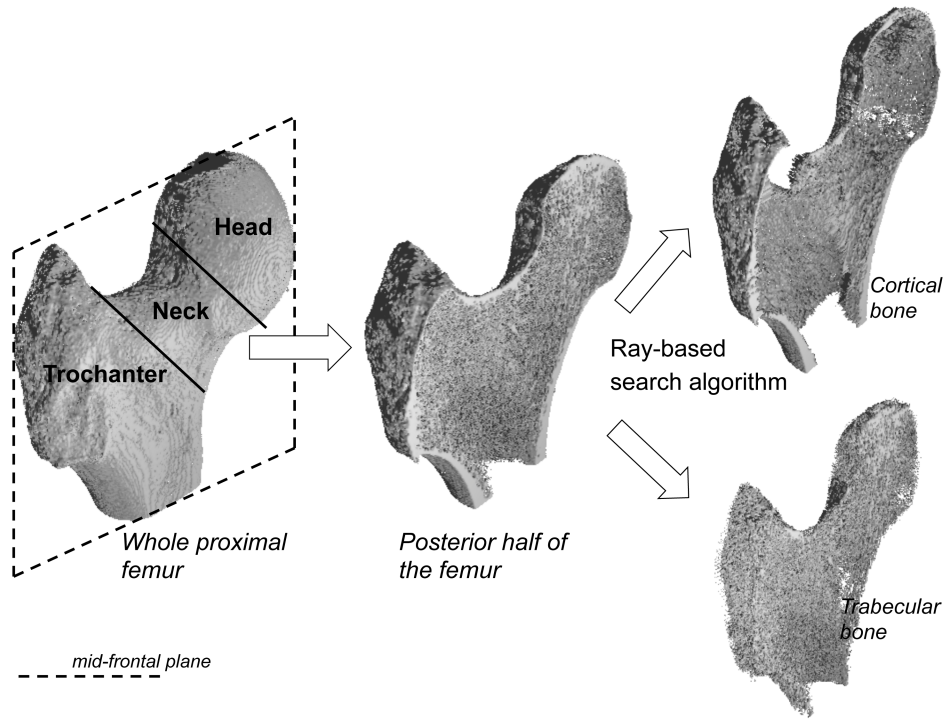


Figure 1-4: Proximal femur compartmentalized (left) into femoral head, neck, and trochanter regions (left). Cortical bone shell and trabecular bone core identified (right) using a ray-based search algorithm [98].

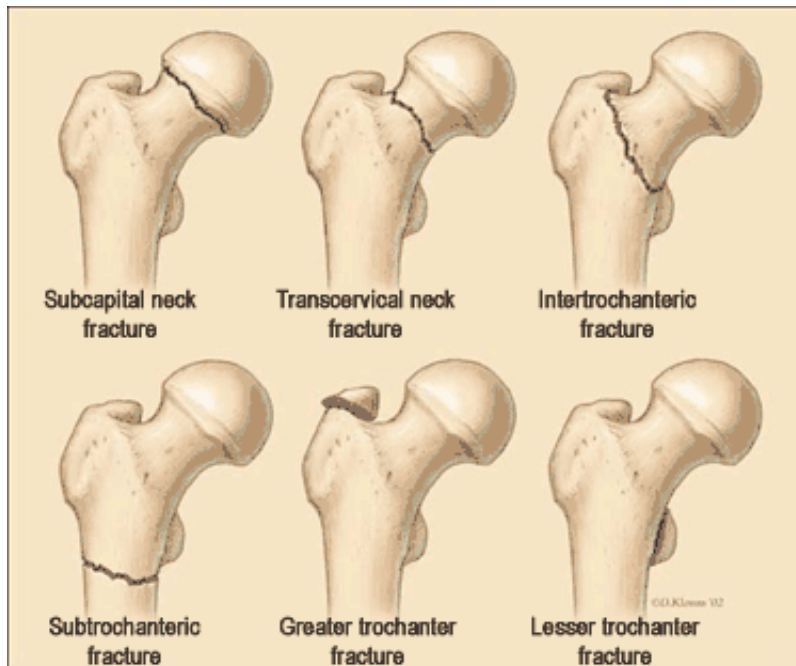


Figure 1-5: Classification of hip fractures. Femoral neck and intertrochanteric fractures (top row) are the most commonly observed types (Adapted from: <http://advancedortho.net/info/hipfractureinfo.php>).



Figure 1-6: Mid-frontal sections of human femurs from 66-year old (left) and 93-year old (right) donors. Aging and disease result in substantial loss of bone mass, deterioration in trabecular microarchitecture, decrease in cortical thickness and increase in cortical porosity.

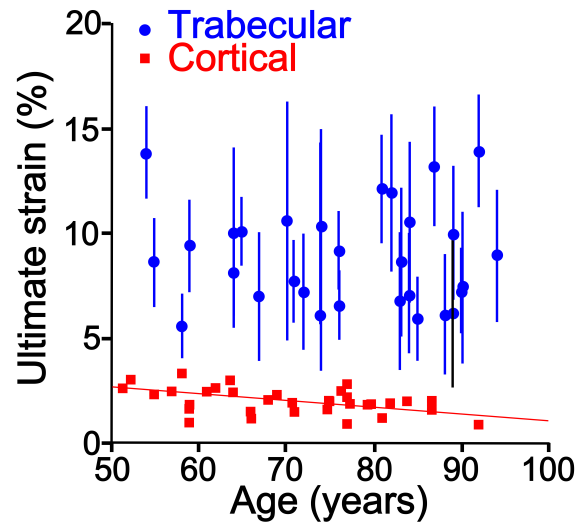


Figure 1-7: Age-related variations in ultimate strain, a measure of tissue-level ductility, for cortical and trabecular bone tissue. Ultimate strains decrease with aging for cortical tissue [25] but not for trabecular tissue [76].

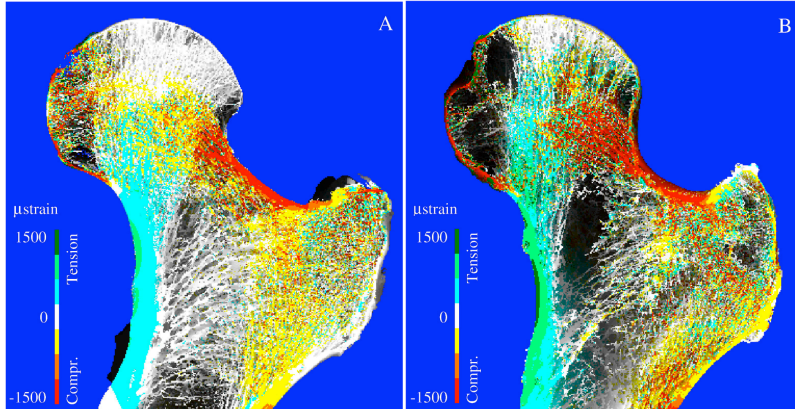


Figure 1-8: Mid-frontal cutaways from a healthy (left) and osteoporotic (right) human femurs showing the distribution of maximum principal strains as predicted by linear, elastic finite element analysis [63].

2. CORTICAL-TRABECULAR LOAD-SHARING IN THE HUMAN FEMORAL NECK¹

2.1 Introduction

A fundamental but poorly understood structure-function issue in both basic-science and clinical biomechanics is the role of the cortical and trabecular bones in the load-carrying capacity of the proximal femur. Cadaver studies have reported that both cortical bone geometry [60] and trabecular bone density [99], as measured with quantitative computed tomography (CT), are strongly associated with femoral strength. However, views diverge as to the relative contributions of the cortical and trabecular compartments to overall femoral strength [50, 100, 101]. Whereas, some have reported that the contribution of the trabecular bone compared to cortical bone to the strength of the femoral neck is only marginal [102, 103], others have suggested that both cortical and trabecular bone work in synergy to provide mechanical competence to the femur [104, 105]. Using finite element analysis, Lotz et al. [62] estimated that the cortical bone supports approximately 50% of the load at the mid-neck and 96% of the load at the base of the neck, during both normal gait and a sideways fall on the greater trochanter. However, that analysis included only one bone, and had limited spatial resolution, which may have led to overestimation of the cortical thickness over some regions of the femoral neck. Addressing the need for higher resolution, more recent analyses developed more mechanistically correct models [45, 63]. However, these studies have not yet focused on load sharing. Thus, the overall goal of this study was to elucidate load-sharing between the cortical and trabecular bone in the human femoral neck, accounting for real bone microstructure at high spatial resolution and multiple bones displaying a wide range in strength.

2.2 Methods

Specimen Preparation and Imaging:

Eighteen fresh-frozen human proximal femurs were obtained from cadavers (n = 13 women; n=5 men; age range: 61–93 years, mean \pm SD = 77 \pm 10 years) with no medical history of metabolic bone disorders. High-resolution peripheral computed tomography images (isotropic voxel size of 61.5 μ m) of the transverse sections of the intact femurs were acquired (XtremeCT, Scanco Medical AG, Switzerland). The femurs were scanned in a custom holder that ensured the femoral diaphysis axis was parallel to the scan's axis of rotation, with the scan region starting at the superior edge of the femoral head and extending to just distal to the lesser trochanter [106]. The scanned gray-scale images were segmented using a global threshold value to create a binary array that contained bone tissue only. A femoral neck region-of-interest was identified based on the procedure described elsewhere in detail [99]. The trabecular and cortical compartments were also identified (**Figure 2-1**), using a two-dimensional ray-based search algorithm previously developed for the vertebral body [98], modified by adding more search directions to account for the geometric complexity of the femur (IDL software suite, ITT Visual Information Solutions, Boulder, CO).

Finite Element Modeling:

High-resolution, three-dimensional finite element models were created for each proximal

¹ This study is under review at Journal of Biomechanics [169]

femur by converting each 61.5-microns cubic voxel into an 8-noded, brick-shaped finite element. All bone elements were assigned the same homogeneous and isotropic hard-tissue material properties: elastic modulus 7.3 GPa [45] and Poisson's ratio of 0.3 [37]. Each femur was virtually tested under two different types of boundary conditions (**Figure 2-2**): stance loading [107] and a sideways fall on the greater trochanter [108]. In each case, a 4,000 N force was applied to the femoral head, the resultant directed at the femoral head center, distributed evenly via a layer of polymethylmethacrylate (elastic modulus of 2.5 GPa and Poisson's ratio of 0.3)

Each finite element model had up to about 280 million elements. Linear elastic finite element analysis was performed using a custom code, including a parallel mesh partitioner and an algebraic multigrid solver [93] on a supercomputing cluster (Stampede, TACC). Typical hardware requirements for a single analysis comprised up to 2176 processors in parallel and 10 TB of memory. Altogether, 36 analyses were performed, requiring a total of about 26,000 CPU hours.

Outcomes and Statistical Analyses

The primary outcome was the fraction of bending moment in the frontal plane (about an anterior-posterior axis) supported by the cortical bone, and was characterized as the ratio of the bending moment acting on the cortical bone to the bending moment acting on all the bone, the calculations performed at each transverse section of the femoral neck (perpendicular to the neck axis) all along its length. By evaluating the variation of this cortical-to-total-bone bending moment along the femoral neck, we identified regions of general load-sharing and load-transfer along the femoral neck. First, the gradient of the cortical-to-total-bone bending moment curve was computed at each transverse section of the femoral neck by calculating the slope of the curve at that section. Then, the transition from load-sharing to load-transfer region was determined as that section at which there was a 20% change in the gradient of the curve compared to the previous section. The length of the load-sharing region and the mean of the cortical-to-total-bone bending moment in this region were also computed for each femur.

The secondary outcome was the distribution of the "axial" (the normal stresses directed along the femoral neck axis) and the von Mises stress, per femoral neck cross-section. The axial stress was presented in the upper and lower neck sections of the femoral neck (at 20% and 80% of the neck length, respectively), and the neutral axis of the bone cross-section (line of zero axial stress) was also identified and displayed. The von Mises stress distribution was only presented in the lower neck section so as to compare the pattern of stress distribution between the femurs.

For one randomly chosen femur from the cohort, we also evaluated the relative contribution of transverse bending versus axial compression behavior of the femoral neck on the overall tissue-level axial stress distribution in the neck. For this analysis, the externally applied femoral head force was resolved into an axial compression component, directed along the neck axis, and a transverse component, directed perpendicular to the neck axis (**Figure 2-2**). Separate finite element analyses were then performed for each component and the resulting stress distributions were compared with those from the original loading condition. These analyses were implemented both for the stance and sideways fall loading configurations.

Standard deviations were determined to describe the inter-specimen variations in the average measurements presented in this study. For the convenience of data post-processing, the femoral neck region-of-interest in each bone was divided into 25 sections, and the data corresponding to each section was computed as an average over all the slices in that section. All statistical tests (JMP 9.0; SAS Institute, Cary, NC USA) were considered significant at $p < 0.05$.

2.3 Results

On average, across all 18 femurs, the cortical bone supported $88\% \pm 5\%$ of the overall frontal-plane bending moment for stance loading and $64\% \pm 9\%$ for a sideways fall on the greater trochanter in the load-sharing region (**Figure 2-3**). Gradients of the load-sharing between the cortical and trabecular bone indicated relatively uniform load distribution over the distal $51\% \pm 6\%$ and $77\% \pm 8\%$ of the femoral neck for the stance and sideways fall loading, respectively. Thus, there was a longer region of load-transfer for stance than sideways fall loading. In the load-transfer region, there was a steep descent in the fraction of bending moment supported by the cortical bone, with its contribution to load-sharing declining down to 40% and 30% for stance and sideways fall, respectively. As a result, the trabecular bone supported up to 60% of the overall bending moment for stance and up to 70% for a sideways fall. For both the types of loading, the region in which trabecular bone dominated the load sharing was located close to the proximal end of the neck, and the cortical bone dominated the load sharing at the distal end of the neck.

There were notable differences in the distribution of normal stresses across a femoral neck cross-section in the distal versus proximal parts of the neck, distinctive of the separate load-transfer and load-sharing characteristics of these regions (**Figure 2-4**). Distally in the femoral neck, the highest normal stresses occurred in the cortical bone, specifically in the inferior and superior aspects. In a sideways fall, the inferior cortex experienced highest stresses in tension, whereas the superior cortex experienced highest stresses in compression. Although the pattern of tensile-compressive stress distribution was reversed during stance loading, the regions of high stresses remained unaltered, and were still concentrated within the cortical bone. For both loading conditions, there was also clear evidence of a straight line of zero axial stress, that is, the neutral axis of the cross-section (**Figure 2-4**). Together, these overall axial stress patterns are indicative of a fully developed beam-bending type behavior of the distal femoral neck, regardless of whether the bone was loaded in a stance or a sideways fall configuration. As a result of this fully developed beam-type behavior, there was well-defined load-sharing between the cortical and trabecular bone.

By contrast, proximally in the femoral neck, the highest normal stresses occurred in the trabecular bone and there was evidence instead of a load transfer through the trabecular bone out to the cortex, without any beam-type behavior. The pattern of tensile-compressive stress distribution in the proximal femoral neck was considerably different for the stance vs. a sideways fall loading. While the regions of high compressive stress were spread out across the cross-section, the regions of high tensile stress consistently occurred within the trabecular bone (**Figure 2-4**). For both the loading configurations, there was no evidence of a neutral axis in the femoral neck cross-section, indicating that beam-bending type behavior that was observed in the

distal femoral neck was absent proximally.

The component analysis on one proximal femur revealed that the relative contributions of the axial vs. transverse component of the overall loading differed between stance vs. a sideways fall (**Figure 2-2**). Nevertheless, the similarities in the pattern of axial stress distribution between overall loading vs. transverse bending (**Figure 2-4**) elucidated the dominant contribution of bending loads to the tissue-level stress distribution in the distal neck. On superposing the axial component of the loading onto the transverse bending portion, there was a greater shift in the position of the neutral axis of the femoral neck cross-section during stance than in a sideways fall (**Figure 2-4**). Moreover, the direction of transverse component of the load was exactly opposite between fall and stance with the direction of axial component being the same (**Figure 2-2**), explaining the reversal in the pattern of tension-compression stress distribution between these two loading configurations (**Figure 2-4**).

The distribution of von Mises stresses across a femoral neck cross-section was considerably different for the stance versus a sideways fall loading (**Figure 2-5**). In the distal neck, the superior-posterior aspect of the cortex was consistently the region of highest von Mises stresses for a sideways fall, whereas, lowest von Mises stresses typically occurred in the trabecular bone. During stance loading, however, superior-posterior aspect of the cortex was the region of lowest von Mises stresses and the highest stresses generally occurred in the inferior aspect of the cortex.

2.4 Discussion

Given that the relative biomechanical roles of the cortical versus trabecular bone in the load-carrying capacity of the proximal femurs is not clear, the goal of this study was to elucidate any load-sharing between the cortical and trabecular bone in the human femoral neck. We found that while the cortical bone supported up to 90% of the overall frontal-plane bending moment in stance loading, it supported only about 60% in sideways fall loading, indicating the important role of trabecular bone for the latter. The load-sharing region always occurred in the distal portion of the femoral neck, was longer for fall than stance loading, and most importantly, was consistently indicative of well-developed beam-type behavior. As a result of these trends, the cortical bone was most highly loaded in the distal region of the neck, whereas the trabecular bone could be more highly loaded more proximally. Taken together, by demonstrating well-delineated, consistent regions of load-sharing and load-transfer between the cortical and trabecular bone within the femoral neck, this study demonstrates the very different biomechanical characteristics of the proximal and distal portions of the femoral neck, and elucidates the mechanisms by which high stresses can develop in the cortical or trabecular bone tissue within the femoral neck.

A major strength of this study is the use of micro-CT-based finite element models that capture bone microstructure at the level of an individual trabecula. Such models can reasonably differentiate between the trabecular and cortical compartments within the femoral neck, which is currently infeasible using low-resolution imaging modalities because of their failure to precisely capture the thin cortex at certain locations with the femur [64, 77]. The finite element models

used here were previously validated for 12 of the 18 femurs analyzed here [45] by using non-linear analysis to compare the model predictions of femoral strength vs. experimental measurements. We have since extended those non-linear analyses to include all the 18 femurs used in this work, and the correlation between the two measures of femoral strength remained high ($R^2 = 0.91$; $p < 0.0001$; data on file at UC Berkeley), confirming the general validity of our computer models. Further, the model-based prediction that high von Mises stresses occur at the superior-posterior aspect of the cortex during a sideways fall is consistent with the experimental observation of de Bakker et al. [109] who reported macroscopic crack initiation at the same location in the femur. These researchers used high-speed video to capture the failure process for twelve femurs, and interestingly, observed secondary macroscopic crack initiation at the inferior-medial aspect of the cortex, which is also predicted to be a region of high von Mises stresses in our computational analyses. In contrast, during stance, the occurrence of low von Mises stresses at the thin, superior-posterior cortex and high von Mises stresses at the thick, inferior-medial cortex, can be explained by the mechanics of bipedal locomotion in the humans — the differential load distribution across the femoral neck during normal gait ultimately leads to evolution of asymmetric (elliptical) structure of the cortex in the distal neck since mechanical loading is known to be a key stimulus for osteogenesis [110].

The pattern of tissue-level stress distribution obtained in this work is consistent with the findings of other finite element studies, both for the stance and sideways fall loading [63, 111]. Moreover, it has been previously suggested — albeit for a very limited sample size — that, cortical bone supports more than 50% of the overall load in the femoral neck during a sideways fall [62, 63]. Recently, Nishiyama et al. [112], using QCT-based models for a sideways fall, reported that cortical bone carries $68.4\% \pm 4.9\%$ of the load in the femoral neck region, which is in close agreement with the finding of this study. However, to our understanding, none of the prior investigations have focused on quantifying the cortical-trabecular load-sharing along the femoral neck either for stance or for a sideways fall.

One novel finding from this study is that cortical bone appears to be consistently the main load-bearing component in the distal half of the femoral neck, both for the stance and sideways fall loading, and is also more highly loaded than the trabecular bone in this region. Together, these results support the widely held tenet that measures of cortical bone geometry and morphology, like the porosity or thickness, might be key determinants of hip fragility [22, 113, 114]. Even so, it is quite clear that the contribution of trabecular bone in maintaining structural integrity of the femur cannot be neglected, especially for a sideways fall on the greater trochanter for which it supports about 40% of the overall bending load. Our finding that both cortical and trabecular bone work in synergy to provide strength to the femur is consistent with the conclusion of Manske and coworkers [105] who reported cortical BMC and trabecular BMD as significant contributors to the femoral failure load. Elucidating the structural relevance of cortical bone, Mayhew and colleagues [50], using critical stress calculations and assuming Euler buckling of the thin superior-lateral cortex, proposed that loss in elastic stability of the cortex in the elderly population might be an important factor leading to hip fractures. Their simplified analysis, however, seems to neglect any stiffening effect that trabecular bone has on the well-developed beam behavior of the distal portion of the femoral neck, since for such behavior, the endosteally located trabecular bone will contribute appreciably to the overall moment of inertia

of the bone. Similarly, Holzer [102] performed mechanical testing on intact versus excavated femurs to suggest that the contribution of trabecular bone to hip failure strength is less than 10%. Although, we qualitatively agree with their outcome, it must be appreciated that by selectively removing trabecular bone from the femoral neck, they might have altered the fundamental micro-mechanics of load distribution within the femur by preferentially loading the cortical bone beyond its physiological capacity, thereby over-estimating its overall contribution to the femoral strength. In this regard, we propose it might be beneficial that any future studies designed to estimate hip fracture risk must consider biomarkers pertaining to both cortical and trabecular bones for holistic analysis of hip fragility.

The presence of high stresses in the peripheral inferior and superior aspects of the cortex — along with the existence of a neutral axis about which the femoral neck seems to bend and a linear gradient in stress distribution across the neck cross-section — provides sufficient evidence to infer that the distal femoral neck exhibits a fully-developed, beam-bending behavior. The development of such beam-type behavior is significant since for such behavior, principles of classical beam theory dictate the normal stress distribution profile across any femoral neck cross-section. Euler beam theory prescribes that, for a beam subjected to transverse bending or combined loading (bending + compression), the stress at any point in a cross-section of the beam is linearly dependent on the shortest distance of that point from the neutral axis of the beam. Accordingly, if the distal neck is behaving like a beam, it would experience maximum normal (tensile or compressive) stresses farthest away from the neutral axis — on the periosteal surface of the cortical bone — and this is indeed observed in our computer analysis. Furthermore, the shift in the position of the neutral axis on superposing axial compression over transverse bending, in conjunction with the exactly opposite orientation of the bending moment acting on the neck for stance versus sideways fall loading, essentially explains the reversal in stress profiles (tension and compression) between these two types of loading. Mechanistically, these analyses indicate that all the bone material, including the trabecular bone, in a cross-section in the distal neck bends about one common neutral axis.

In contrast, proximal to this load-sharing region but still within the femoral neck there is substantial load transfer from the trabecular bone to the cortical bone and beam-bending behavior does not occur. This load-transfer region is longer for stance loading than for sideways fall loading; that is to say, more of the femoral neck exhibits classic beam-type bending for a sideways fall loading than for stance loading. In contrast to the load-sharing region, in the load-transfer region maximum stress can occur anywhere in the cross-section, the location depending on how and where the load is transferred. Our analyses show that the trabecular bone is most highly loaded in the load-transfer region and individual trabeculae bend about their own neutral axes. Taken together, these analyses suggest that while cortical bone will be the first tissue to fail in the distal portion of the femoral neck where there is fully-developed, beam-type behavior, trabecular bone can fail first in the more proximal portion because of the load transfer that occurs in that region.

This study has a number of limitations. First, we assumed the same homogenous material properties for both cortical and trabecular bone tissue. The literature suggests only minor differences between the elastic properties of cortical and trabecular tissue [37] and our

preliminary studies showed only a small effect on overall femoral stiffness after changing the elastic modulus of the cortical bone by $\pm 20\%$ [115]. Consistent with this small effect, as noted above, our non-linear failure study [45], which assumed homogeneous cortical and trabecular properties, produced excellent agreement with experiments ($R^2 = 0.94$). Thus, this limitation was considered minor. Second, we only examined two load cases. It is likely that different degrees of load sharing would occur for different loading cases, but we do not expect the general trends of distinctly different regions of load-sharing and load-transfer to disappear. Lastly, the sample size was relatively small. Again, given the consistency in trends, we would not expect to have reached different conclusions had a larger sample size been used. However, different trends might be observed for different racial groups, particularly if bone size or shape were fundamentally different. Lastly, resolution was fine, but still limited, at 60 micron. It is likely that this limitation might influence failure behavior more than the elastic behavior reported here, consistent with results from various convergence studies [116, 117].

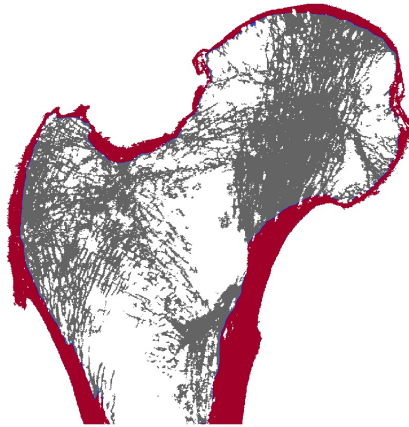


Figure 2-1: Projection of a 1-mm-thick mid-frontal section of the proximal femur, showing the cortical (red) and trabecular bone (gray) identified using a ray-based search algorithm (see text).

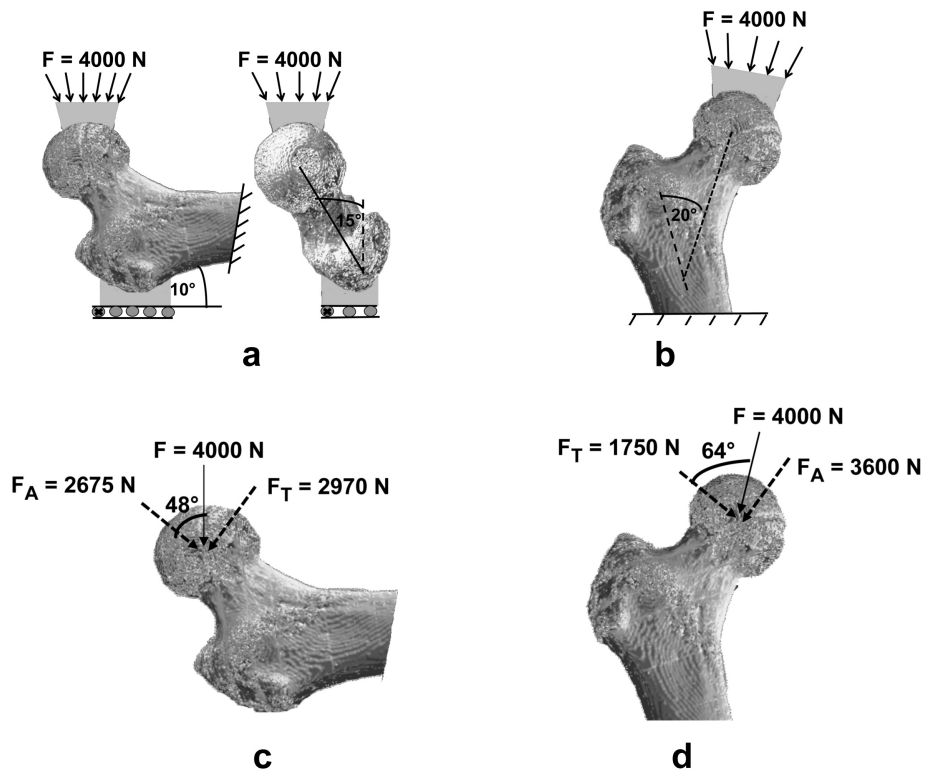


Figure 2-2: Boundary conditions used in finite element analysis to simulate: a) a sideways fall, and b) stance loading. A force of 4,000 N was applied to the femoral head, the resultant directed towards the center of the femoral head. Component analysis of one randomly chosen proximal femur for: c) a sideways fall, and d) stance loading. F : overall loading (4,000 N). F_A : axial component and F_T : transverse component.

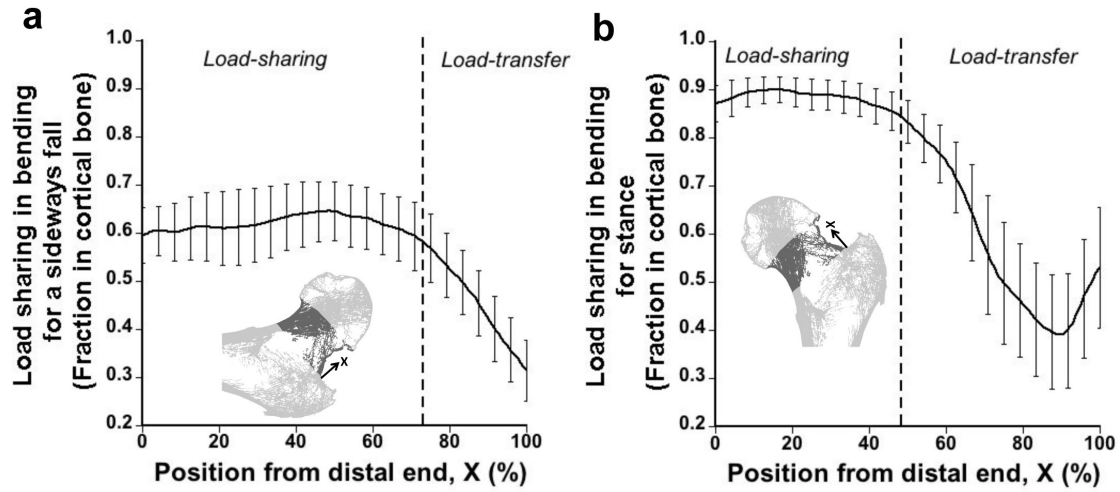


Figure 2-3: The variation in the fraction of total frontal-plane bending moment carried by the cortical bone for: a) a sideways fall, and b) stance loading. The vertical dotted line demarcates the load-sharing and load-transfer regions in the femoral neck. Error bars represent standard deviations from the mean values (for n=18 bones).

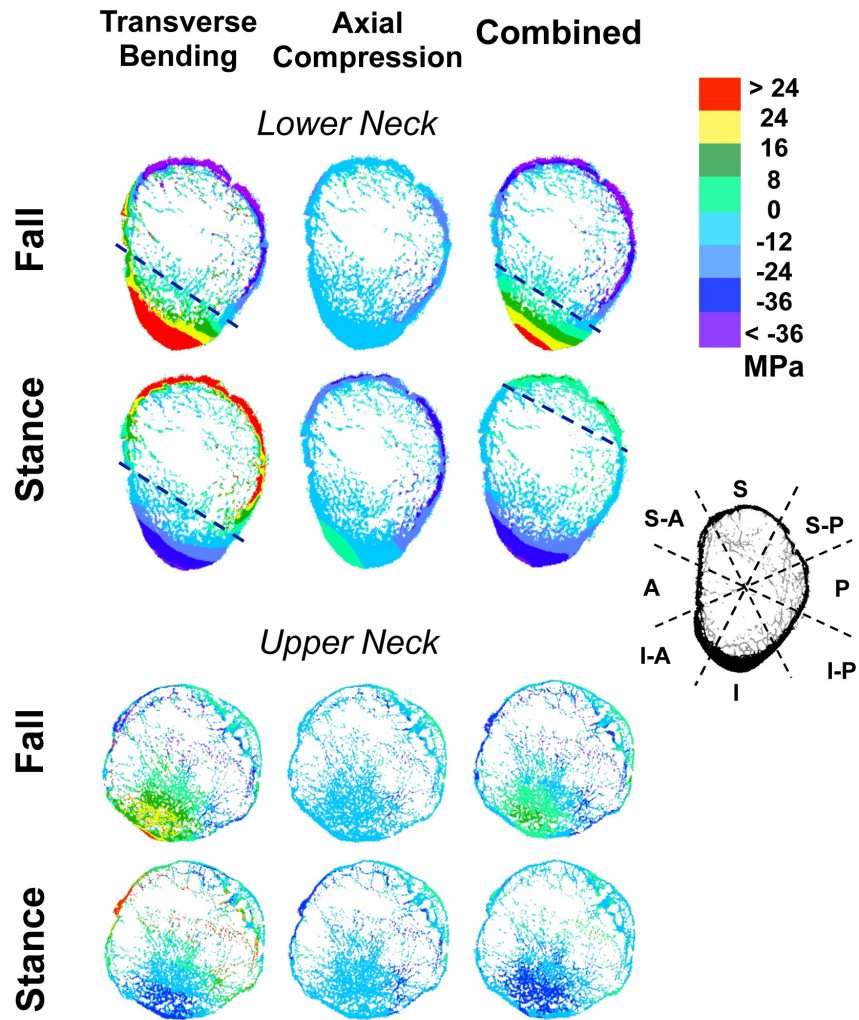


Figure 2-4: The variation in the distribution of tissue-level axial stress across the femoral neck cross-sections, for sideways fall and stance loading, in a single femur. S: Superior, P: Posterior, A: Anterior, I: Inferior.

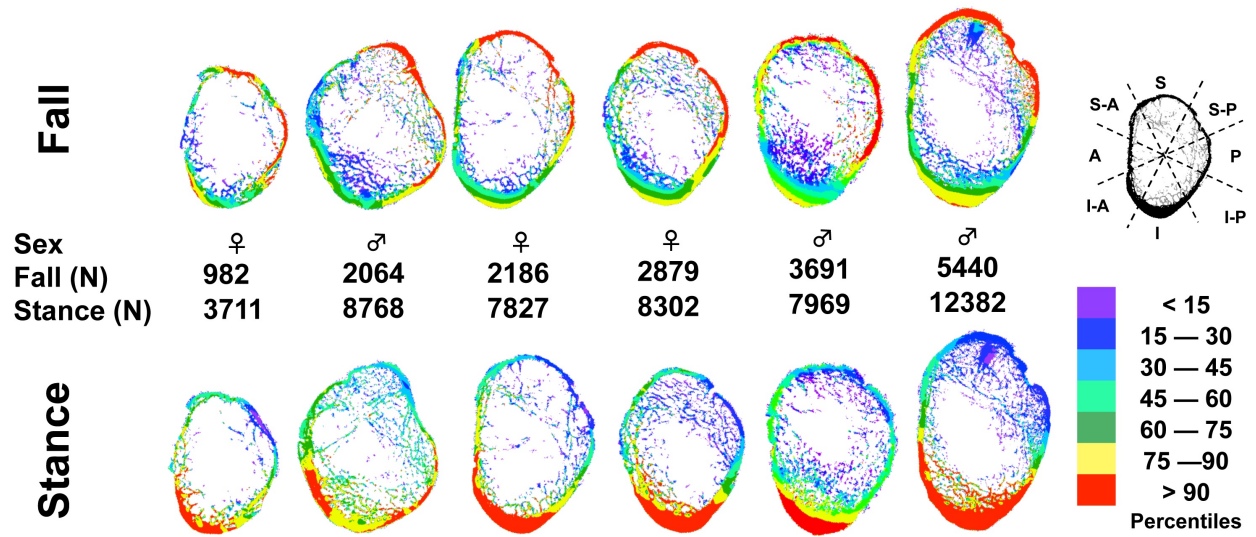


Figure 2-5: The variation in the distribution of von Mises stress across the femoral neck cross-sections in the distal neck, for sideways fall and stance loading, across six bones randomly chosen for our cohort of 18 femurs. S: Superior, P: Posterior, A: Anterior, I: Inferior. Strength values are shown from non-linear finite element modeling, for fall and stance loading (performed as part of a different study [45], which is presented in the next chapter in this dissertation).

3. MICROSTRUCTURAL FAILURE MECHANISMS IN THE HUMAN PROXIMAL FEMUR FOR SIDEWAYS FALL LOADING²

3.1 Introduction

Just as the cytoskeletal and cell membrane mechanisms of mechanotransduction are fundamental to understanding adaptive bone remodeling, the microstructural failure mechanisms of femoral strength are integral to understanding hip fracture etiology [118]. Elucidating the microstructural failure mechanisms of individual trabeculae within isolated trabecular bone specimens has provided unique insight into their structure-level strength behavior [119-123]. However, at the whole-bone level, much less is understood. A recent study on microstructural failure mechanisms within elderly cadaver vertebrae, which used micro-CT-based, non-linear finite element analysis combined with biomechanical testing, suggested that diminished structural redundancy — in which the overall bone yields after failure of only a tiny proportion of the bone tissue — might be an important etiologic aspect of age-related vertebral fragility [84]. However, such studies have not yet been extended to the proximal femur due in large part to the technical challenges of imaging the proximal femur at sufficiently high resolution and performing the massive computational analysis with the required non-linear constitutive modeling. Since there are substantial differences in the size, geometry, shape and internal morphology (both cortical and trabecular) [124-126] — and thus biomechanics — between vertebral bodies and the proximal femur, it is not clear if these same principals of structural redundancy also apply to the proximal femur. Thus, overcoming these technical challenges, we sought to elucidate the microstructural failure mechanisms in the elderly human proximal femur, for sideways fall loading, by performing biomechanical testing and nonlinear finite element analysis on high-resolution micro-CT-based models of the proximal femur and doing so for multiple bones.

3.2 Methods

Sample Preparation And Micro-CT Scanning:

To account for the possibility that the microstructural failure mechanisms might be influenced by overall bone morphology, trabecular bone volume fraction, and microstructure, our sample of 12 elderly proximal femurs was chosen to be morphologically diverse (Table 3-1). The femurs were obtained fresh-frozen from cadavers with no medical history of metabolic bone disorders (Mean \pm SD age = 76 \pm 10 years; age range = 62-93 years; n=8 females, n=4 males). Before biomechanical testing, high-resolution images were acquired (XtremeCT, Scanco Medical AG, Switzerland) of each intact femur, using a custom holder to ensure the femoral diaphysis axis was parallel to the scan's axis of rotation, the scan covering from just above the femoral head to just below the lesser trochanter. The resulting images (isotropic voxel size of 61.5 μ m) were coarsened to 82 μ m to facilitate computational analysis and then segmented using a global threshold. To facilitate model parameterization and results post-processing, a femoral neck region-of-interest was defined using procedures described elsewhere [61], and a trochanteric region-of-interest was defined as all bone lateral and distal to the femoral neck (**Figure 3-1**). The trabecular and cortical compartments were also identified (**Figure 3-1**), using a two-dimensional ray-based search algorithm previously developed for the vertebral body [98],

² This study has been published in Journal of Bone and Mineral Research [45]

modified by adding more search directions to account for the geometric complexity of the femur (IDL software suite, ITT Visual Information Solutions, Boulder, CO).

Standard measures of bone volume and geometry were derived from the original scans. Integral bone volume was calculated as the total volume of all bone voxels in the femur. Cortical and trabecular bone volume were defined as the total volume of bone voxels present in the cortical and trabecular compartments, respectively. Femoral neck axis length, neck-shaft angle, minimum femoral neck cross-sectional area, minimum femoral neck areal moment of inertia, and femoral head diameter, were measured as per published guidelines [127, 128].

Dual-Energy X-ray Absorptiometry (DXA):

DXA scans were taken for all bones before biomechanical testing. Areal bone mineral density (aBMD, g/cm²) for the femoral neck and total femur regions, and total hip bone mineral content (BMC, g) were measured (QDR4500 Discovery, Hologic, Inc., Bedford, MA) as described elsewhere [106]. Briefly, femurs were scanned in a 15-cm-deep water bath to simulate the presence of soft tissue and a custom-made holder was used to ensure clinical-like positioning.

Biomechanical Testing:

After all imaging, biomechanical testing was performed to measure femoral strength using a sideways fall configuration [106]. Briefly, the femurs were cut distal to the lesser trochanter and embedded in polymethylmethacrylate (PMMA) within a positioning jig. Adduction and internal rotation were then set to 10° and 15°, respectively. To minimize localized point loading, load was applied at the femoral head via a plastic cup, and the greater trochanter was embedded in PMMA. Rapid vertical loading was applied at a constant rate of 100 mm/s using a servohydraulic materials testing system (Model 1331, Interlaken Technology Corporation, Chaska, MN). To facilitate direct comparison with the finite element results, a 0.2%-offset yield strength — heretofore denoted simply as the strength — was defined from the resulting force-strain curve using a 0.2%-offset strain criterion, in which strain was calculated as the vertical displacement of the surface of application of load with respect to the lateral trochanter divided by the original distance between these planes. We note that the ultimate and 0.2%-offset yield strengths were highly correlated with each other ($R^2 = 0.96$), and, on average, were within 10% of each other (see Table 3-1), and thus the yield strength was also highly representative of the ultimate strength. High-speed video was obtained at 500 frames per second (MotionScope PCI 8000S, Redlake Imaging Corporation) to visualize the external failure patterns and classify fracture location (trochanteric versus femoral neck).

Non-Linear Finite Element Analysis:

Using the high-resolution scans, a voxel-type finite element model was generated for each femur. All elements were eight-noded, cube-shaped, and 82 μm along each side. Using custom code [93, 129], geometrically and materially nonlinear analysis [83, 96] was performed. Bone tissue in the femoral neck and the trochanter was modeled as a fully ductile material [78], using a rate-independent elasto-plasticity model [130] and homogenous isotropic tissue material properties: effective elastic modulus 18.0 GPa, Poisson's ratio of 0.3, and tissue-level tensile and compressive yield strains of 0.33% and 0.81%, respectively [37]. Because the effective elastic modulus for the bone tissue is not known *a priori* for these whole-femur models, the tissue-level

elastic modulus was then retrospectively scaled down from 18.0 GPa to 7.3 GPa by calibrating the finite element-estimated 0.2%-offset yield strength with the corresponding measured strength to ensure $Y=X$ agreement. Use of a strain-based failure criterion ensured that such a calibration only proportionately reduced the absolute value of the computed femoral strength, without influencing the tissue-level deformation mechanisms or failure locations.

Displacement-type boundary conditions were applied to simulate the loading used in the experiments (**Figure 3-2**). An apparent-level compressive strain of 1.6% was applied to the medial aspect of the femoral head via a simulated layer of PMMA (elastic modulus 2.5 GPa; Poisson's ratio 0.3), this loading being sufficient to reach the 0.2%-offset yield point of each femur. The layer of PMMA at the greater trochanter was constrained in the vertical direction to simulate contact between the trochanter and the floor. The distal end of the diaphysis was held fixed from horizontal motion using a roller boundary condition, a single node being held fixed to avoid rigid body rotation. For computational efficiency, the bone tissue in the superior portion of the femoral head was not allowed to fail so as to eliminate spurious stress oscillations near the boundary conditions. As in the experiment, structure-level yield strength was defined from the overall force-strain curve using a 0.2% strain-offset criterion, and is referred to henceforth as simply the strength.

In terms of the computational infrastructure requirements, the nonlinear nature of the analysis represented a challenging computational problem due to the huge size of each finite element model, further magnified by the inclusion of multiple bones. Individual finite element models contained up to about 120 million elements (over 400 million degrees of freedom) and were solved using an implicit, parallel finite element framework [93]. The nonlinear solution algorithm was an inexact Newton's method wherein each iteration was solved using an algebraic multigrid solver designed specifically for use on a massively parallel supercomputer. Each analysis was performed on a Sun Constellation Cluster supercomputer (Ranger, TACC), requiring up to 4096 processors in parallel and a 140 TB of memory. Overall, the 12 nonlinear analyses required a total CPU time of about 525,000 hours (~ 60 days).

Finite Element Outcomes and Statistical Analysis:

Several outcomes from the finite element analyses were used to characterize the microstructural failure mechanisms. To quantify the failed tissue and identify the tissue-level deformation mechanisms, we assessed the number and loading modes (tensile vs. compressive) of the failed Gauss points (of eight total) in each finite element. The total proportion of failed tissue (*i.e.* the amount of failed tissue per unit bone volume) was calculated as the number of failed Gauss points at the 0.2%-offset yield point of the whole femur, divided by the total number of Gauss points in the model (excluding the PMMA). A similar calculation was used for each of the cortical and trabecular compartments. The ratio of the proportion of failed tissue in the neck to that in the trochanter, defined as the neck-to-trochanter failure ratio, was used in an exploratory manner to predict the fracture type (femoral neck fracture for high values vs. trochanteric fracture for low values). We also calculated a structure-level elastic limit, yield strain, and post-elastic strain from the finite element analysis. The elastic-limit strain was defined as the strain at which 0.1% of the bone tissue in the femur had failed; the yield strain was defined

as the strain corresponding to the 0.2%-offset yield point of the femur; and the post-elastic strain was calculated as the difference between the yield and elastic-limit strains. We also calculated the percent change in secant stiffness of the femur (secant stiffness at the elastic-limit strain vs. initial stiffness), which was considered to be a measure of structural redundancy in the femur: the higher the percent change in this secant stiffness, the lower the structural redundancy. This measure was motivated by the common engineering practice in which the redundancy of such engineering structures as buildings and bridges is evaluated by computing the decline in their stiffness after some of their critical load-bearing components are damaged [131].

To assess model validity, regression analysis was used to compare the degree of scatter between the experimentally measured and finite element-estimated strengths. Pearson correlation coefficients were then used also to assess the association between the measured femoral strength and any other finite element outcomes, as well as the various measures of bone volume, density, and geometry. To assess any independent role of the finite element outcomes with respect to aBMD (as measured by DXA), we performed correlation analysis between each of the predictors and the residuals of the strength-aBMD linear regression relation (strength from experiment; aBMD from DXA). All statistical tests (JMP 9.0; SAS Institute, Cary, NC USA) were considered significant at $p < 0.05$.

3.3 Results

The finite element-derived strengths spanned a large range ($\sim 1,000$ – $5,000$ N) and were in excellent agreement with the directly measured values ($R^2 = 0.94$, $p < 0.0001$, **Figure 3-3A**), supporting the validity of the finite element simulations. There was also good qualitative agreement between the model predictions of fracture type (femoral neck vs. trochanter) and the observations from the high-speed video recordings (**Figure 3-3B**). Overall, we observed, from the videos, five neck fractures and seven trochanteric fractures, with no obvious trend between fracture type and measured femoral strength, and 8/12 of these fracture types were correctly classified by ranking of the finite element-estimated neck-to-trochanter failure ratio. In particular, the five lowest values of the finite element-estimated neck-to-trochanter failure ratio occurred in femurs that exhibited trochanteric fractures, and the three highest values occurred in femurs that had neck fractures (**Figure 3-3B**).

The amount of failed tissue comprised only a tiny proportion (1.5–6.4%) of the overall bone tissue (**Figure 3-4**), a hallmark of poor structural redundancy, and an effect that was accentuated in the weaker femurs. Regardless of the measured femoral strength, tissue-level failure always started in the trabecular bone, the initial amount of failed tissue in the trabecular bone being over 20-fold greater than in the cortical bone (**Figure 3-5**, see animations in [45]). In the weakest femurs, the failed tissue occurred in the trabecular bone in either the greater trochanter or subcapital femoral neck regions (**Figure 3-4**). For one of these weak femurs, the highly localized tissue failure in the greater trochanter was consistent with crushing of the greater trochanter as observed in the video from biomechanical testing (see animation 4 for the high-speed video recording in the online version of this article). In the stronger femurs, the failed tissue was more widespread: in addition to the trabecular bone regions, the tissue failure also progressed into the cortical bone at the medial and superior-lateral aspects of the femur (**Figure 3-4**).

There was a shift in the microstructural failure mechanisms between weak versus strong femurs as reflected by more dominant failure behavior of the trabecular bone in the weakest of bones and recruitment of both trabecular and cortical bone as strength increased. In general, as femoral strength increased, there was an approximately linear increase (**Figure 3-6**) in the amount of failed tissue in both the cortical ($R^2 = 0.83$, $p < 0.0001$) and trabecular ($R^2 = 0.87$, $p < 0.0001$) bone. In the weakest bones, there was also preferential failure of the trabecular bone, indicated by an increase in the ratio of trabecular-to-cortical failure ($R^2 = 0.67$, $p < 0.01$, **Figure 3-6**), in large part because there was so little failure of the cortical bone.

As expected, the linear regression analysis indicated that the finite element-derived strength had a higher correlation with the measured femoral strength than did the various measures of bone mass, volume, density, and geometry, but surprisingly so too did the finite element-derived proportion of failed tissue (**Table 3-1**). The correlation analysis of the residuals of the strength-femoral neck aBMD relation revealed that femurs with low strength relative to their areal BMD had a low proportion of trabecular bone compared to cortical bone in the femoral neck ($p < 0.001$), less failed tissue ($p < 0.05$), and low structural redundancy as quantified by the percent decline in secant stiffness at 0.1% tissue failure ($p < 0.005$; **Table 3-2**). Consistent with these correlations, one particular femur had a relatively high aBMD (total hip and femoral neck) but a low strength (**Figure 3-7A**). This femur had the lowest trabecular-to-cortical bone volume amongst all specimens and had the lowest degree of structural redundancy, (**Figure 3-7B**).

3.4 Discussion

This is the first study to directly link direct measures of proximal femoral strength to estimates of the amount and distribution of tissue-level failure within the bone, accounting for the spatial resolution of individual trabeculae and the thin cortex. Our results suggest that, when the femur fails as a result of a sideways fall, tissue-level failure starts in the trabecular bone, particularly in the trochanter and subcapital femoral neck regions for the very weakest of bones. Because of this “weak-link” effect of the trabecular bone, cortical bone appears only be engaged in the failure process when there is sufficient trabecular strength in the trochanteric and subcapital femoral neck regions to withstand the fall loading. Once the cortex is engaged, tissue-level failure appears to involve both the trabecular and cortical bone, with neither dominating in any obvious way although, by volume, we always observed more trabecular failure. We also found evidence, as we have done for the vertebral body [84], of reduced structural redundancy, particularly in the weakest of femurs, as indicated by the tiny amount of failed tissue per unit bone mass at the point of initial structural failure. Femurs with low structural redundancy tended to have low strength relative to their areal BMD, which was associated with a low proportion of trabecular bone compared to cortical bone in the femoral neck. We conclude that initial failure of the femur during a sideways fall is associated with failure of just a tiny proportion of the bone tissue, failure of the trabecular tissue dominating in the very weakest femurs due in part to diminished structural redundancy.

These new results emphasize the importance of the concept of structural redundancy in the etiology of osteoporotic fractures, both for the hip and spine. Engineers design structural

redundancy into systems that require safe function in the event of failure of some individual components, for example in airplanes and bridges. Redundancy in biological systems is not limited to structural redundancy, as is evident by our eyes and ears: while failure of one eye diminishes overall vision function it does not lead to blindness; similar for hearing loss in one ear. Our results suggest that the major “osteoporosis” regions of the skeleton — the hip and spine — do not exhibit such redundancy in the face of appreciable bone loss. In a recent investigation on cadaver vertebral bodies loaded to failure in axial compression[84], the concept of structural redundancy was introduced to better elucidate the microstructural basis of whole-bone fragility at the spine, and it was revealed that weaker vertebrae had less structural redundancy since only a tiny amount of tissue failure, per unit bone mass, occurred at the point of initial vertebral structural failure. Likewise, in this study, we found that the weakest femurs had minimal structural redundancy. Since the overall size and shape, internal cortical [125, 126] and trabecular[124] morphology, and external loading conditions of the proximal femur (for a fall) and the vertebral body are so different, these collective findings suggest that reduced structural redundancy is a general characteristic of advanced bone loss, at least at the hip and spine.

This concept of structural redundancy also helps elucidate how some bones may be weak despite a relatively high measure of areal BMD. The fact that structural redundancy for the femur (and spine) is directly linked to strength is not unexpected — just as the addition of extra support cables in a suspension bridge increases structural redundancy, those extra cables also increase strength. Importantly, minimal structural redundancy signals little or no margin of error if the hip or spine is slightly overloaded. In particular, if a bone with a higher degree of structural redundancy is slightly overloaded, it can sustain appreciable internal tissue-level damage without overtly fracturing — and presumably can recover over time via bone remodeling that repairs such damage. By contrast, a more fragile bone will fracture if only slightly overloaded because of its lack of structural redundancy. We note that this is not to say a weak bone is automatically more fragile. In this small cadaver study, we only assessed older bones, most with relatively low bone volume fraction. It is likely that small-sized bones in young people would also be weak due to their small size even if they had a high bone volume fraction — but we would expect such bones to maintain structural redundancy if they had high bone volume fraction. On the other hand, we observed one femur in this small cohort that had relatively high aBMD but low strength. This femur had the lowest degree of structural redundancy because of its low relative amount of trabecular bone compared to cortical bone in the femoral neck, which in turn led to a low proportion of trabecular failure — in a sense, the cortical bone was not engaged in the failure process because of the lack of structural redundancy. This unique specimen exemplifies that femurs with high bone density, mass, volume or size might not necessarily be strong if they lack sufficient structural redundancy. This finding suggests that individuals with low trabecular mass relative to cortical mass in the femoral neck have fewer internal load transfer paths and thus less structural redundancy, leading to low strength relative to areal BMD. Such a hypothesis, which may help explain why many individuals with osteopenia sustain hip fractures, requires further testing in cadaver and clinical studies.

These results also provide insight into the relative strengthening roles of the cortical versus trabecular bone. Our simulations revealed that failure started in the trabecular tissue for all femurs. For the weakest three femurs (strength < 1,700 N), this trabecular failure was

sufficient to trigger overall structure-level yielding without much cortical engagement because of the low degree of structural redundancy. However, for the stronger femurs, because of slightly better structural redundancy, overall yielding did not occur until tissue-level failure had progressed into the cortical bone. Based on these observations, the five-fold difference in femoral strength between the weakest versus strongest femurs in this study could be attributed in part to the negligible role of cortical bone and the diminished capacity of the remaining trabecular bone in the very weakest femurs — these femurs fail structurally before the cortical bone can be recruited. Cortical bone is deemed to be a major load-carrying component of the proximal femur [105, 132, 133] — and it may well be in many femurs. However, our analysis suggests a potentially important interaction effect: that unless the trabecular bone is sufficiently strong, the strengthening capacity of the cortical bone will remain largely untapped. Realizing that these results require validation in a larger cohort, they nonetheless suggest interesting implications for how treatments might alter fracture risk differently in patients who have severely weak versus moderately weak femurs.

This study has a number of limitations. Most importantly, as a cadaver study with a small sample size, care must be taken when generalizing. While the sample of bones in this study spanned a wide range of strengths (~ 1,000–5,000 N), and thus was sufficiently diverse to support the generality of the trends reported here, it clearly would be desirable to increase this sample size to confirm these trends and to better probe the behavior of those femurs having relatively high real BMD but low strength or other unusual characteristics. Secondly, because the corresponding experiments would be almost impossible to perform, we used simulation, albeit highly advanced, to assess internal tissue-level failure. Those simulations only modeled microstructural failure mechanisms at initial whole-bone structural-level failure, and furthermore were based on a number of specific assumptions that could affect the absolute measures of tissue failure, most importantly that: 1) the cortical and trabecular failure and post-yield properties are the same, although the available evidence suggests they are not [25, 76]; 2) the tissue is fully ductile and does not undergo micro-damage or fracture [134]; and 3) there was no intra- or inter-bone variation in assumed tissue-level material properties [135, 136]. Changing these assumptions, as well as changing the overall loading conditions and bone orientation, will undoubtedly change the absolute numbers of failed tissue reported here, and perhaps more importantly, the relative magnitude of the cortical vs. trabecular failure. In a recent study [78], we compared strength for trabecular bone cubes using simulations that assumed either fully ductile or fully brittle tissue-level failure behavior. We found an almost two-fold difference in predicted strength, although that effect was almost constant despite a wide range of bone volume fraction and microarchitecture, suggesting on the one hand that limitations on tissue-level ductility may be important, and on the other hand that such tissue-level ductility effects may be independent of bone volume fraction and microstructure. These recent results and the good agreement in this study between model and experiment for whole-bone yield strength together suggest that the general *trends* (but not absolute values) reported here are unlikely to change appreciably. Even so, further studies are required to determine how the various modeling assumptions might affect the trends reported here, and it is entirely possible that in a larger cohort some bones are encountered with tissue-level material and overall strength behaviors that are not typical of these trends.

Table 3-1: Characteristics of the study population (mean, standard deviation) and correlation coefficients between selected outcomes and various predictor variables.

Outcomes and Variables (units)	Sample Characteristics (n=12)		Expt ultimate strength (N)	Expt yield strength (N)	FEA yield strength (N)	DXA FN aBMD (g/cm ²)
	Mean	SD				
Experiment Outcomes:						
Expt ultimate strength (N)	2840	1050	1.00	0.98	0.96	0.80
Expt yield strength (N)	2590	990	0.98	1.00	0.97	0.78
Finite Element Parameters:						
FEA-estimated strength (N)	2690	960	0.96	0.97	1.00	0.79
FEA-estimated stiffness (kN/mm)	3.21	0.94	0.91	0.93	0.96	0.73
Total failed tissue (%)	4.10	1.61	0.96	0.94	0.93	0.73
Femoral neck failed tissue (%)	1.55	0.85	0.67	0.57	0.62	0.50
Trochanter failed tissue (%)	2.55	1.08	0.90	0.95	0.89	0.69
Trabecular failed tissue (%)	2.69	0.84	0.95	0.94	0.95	0.71
Cortical failed tissue (%)	1.41	0.78	0.94	0.91	0.87	0.75
Tension failed tissue (%)	2.42	0.96	0.94	0.93	0.90	0.77
Compression failed tissue (%)	1.68	0.71	0.91	0.86	0.88	0.62
Force at elastic limit (from FEA, N)	960	430	0.89	0.91	0.92	0.60
Structure-level elastic strain (%)	0.30	0.07	0.74	0.72	0.68	0.38
Structure-level yield strain (%)	1.18	0.08	0.48	0.48	0.35	0.34
Structure-level post-elastic strain (%)	0.88	0.09	-0.16	-0.15	-0.22	0.00
Percent change in stiffness (at 0.1% damage)	1.92	0.32	-0.74	-0.74	-0.71	-0.40
DXA Parameters:						
Femoral neck aBMD DXA (g/cm ²)	0.44	0.16	0.80	0.78	0.79	1.00
Total hip aBMD DXA (g/cm ²)	0.58	0.20	0.87	0.84	0.85	0.96
Total hip BMC DXA (g)	21.3	8.61	0.87	0.85	0.81	0.92
Micro-CT Parameters:						
Total hip integral bone volume (cm ³)	48.8	9.25	0.87	0.86	0.87	0.83
Total hip cortical bone volume (cm ³)	19.8	3.94	0.78	0.76	0.79	0.86
Total hip trab bone volume (cm ³)	29.0	6.00	0.83	0.82	0.82	0.72
Femoral neck integral volume (cm ³)	8.69	1.71	0.65	0.65	0.57	0.82
Femoral neck cortical volume (cm ³)	3.58	1.08	0.21	0.19	0.13	0.63
Femoral neck trab volume (cm ³)	5.11	1.57	0.83	0.84	0.75	0.79
Trochanter integral volume (cm ³)	25.1	5.46	0.86	0.83	0.89	0.69
Trochanter cortical volume (cm ³)	13.2	2.56	0.80	0.78	0.84	0.74
Trochanter trabecular volume (cm ³)	12.0	3.16	0.78	0.75	0.80	0.55
Total hip trab/cortical volume ratio	1.48	0.24	0.06	0.09	0.10	-0.09
Femoral neck trab/cort volume ratio	1.46	0.31	0.74	0.78	0.76	0.32

<i>Trochanter trab/cortical volume ratio</i>	0.91	0.19	0.22	0.20	0.20	0.04
<i>Head diameter (cm)</i>	2.21	0.13	0.61	0.67	0.72	0.64
<i>Neck-axis length (cm)</i>	6.20	3.87	0.20	0.20	0.21	0.46
<i>Neck-shaft angle (degrees)</i>	125	4.90	-0.26	-0.21	-0.17	0.09
<i>Neck cross-sectional area (cm²)</i>	7.20	1.22	0.54	0.60	0.57	0.45
<i>Neck areal moment of inertia (cm⁴)</i>	4.71	1.80	0.62	0.66	0.65	0.54

Bolded values have $p < 0.05$. SD: standard deviation, Expt: experiment; FEA: finite element analysis; DXA: dual-energy X-ray absorptiometry; FN: femoral neck; aBMD: areal bone mineral density; BMC: bone mineral content.

Table 3-2: Correlation analysis on the residuals of the linear regression between the femoral strength (from experiment) and femoral neck aBMD (from DXA), versus selected variables. Positive or negative coefficients indicate that a low or high value, respectively, in the variable is associated with a negative residual, namely, a low strength with respect to the aBMD.

Variables (Units)	Pearson correlation coefficient (r)
<i>FEA-estimated strength (N)</i>	0.56
<i>Total failed tissue (%)</i>	0.60*
<i>Trabecular failed tissue (%)</i>	0.64*
<i>Cortical failed tissue (%)</i>	0.52
<i>Force at elastic limit (from FEA, N)</i>	0.70*
<i>Structure-level elastic strain (%)</i>	0.68*
<i>Percent change in stiffness (at 0.1% damage)</i>	-0.78[†]
<i>Total hip BMC DXA (g)</i>	0.21
<i>Total hip integral bone volume (cm³)</i>	0.33
<i>Total hip trab/cortical volume ratio</i>	0.26
<i>Femoral neck trab/cortical volume ratio</i>	0.85[§]
<i>Trochanter trab/cortical volume ratio</i>	0.27

Bolded values have $p < 0.05$. * $p < 0.05$, [†] $p < 0.005$, [§] $p < 0.001$
See Table 3-1 for legends.

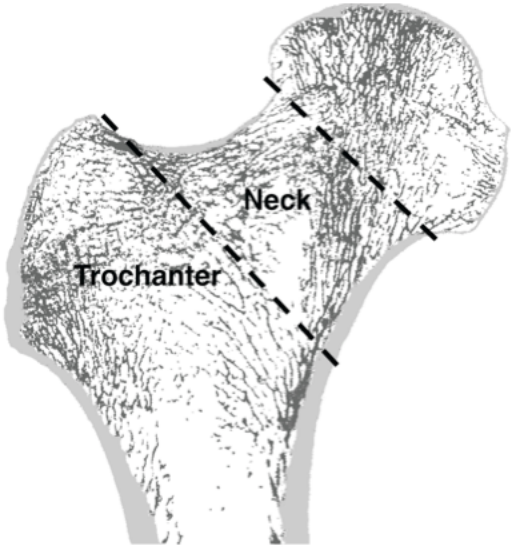


Figure 3-1: Projection of a 1 mm-thick mid-frontal slice of the proximal femur, showing the cortical (light gray) and trabecular bone (dark gray). The neck and trochanteric regions of interest are shown, which were used in prediction of fracture type (see text).

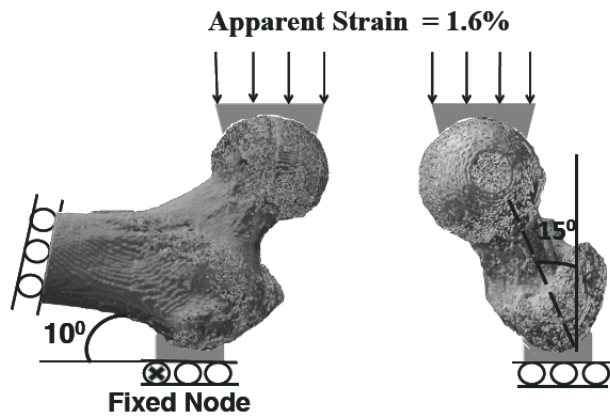


Figure 3-2: Boundary conditions used in finite element analysis to simulate a sideways fall: A) the femoral diaphysis axis is set to an angle of 10° with respect to the horizontal, and B) the femur is internally rotated by an angle of 15°.

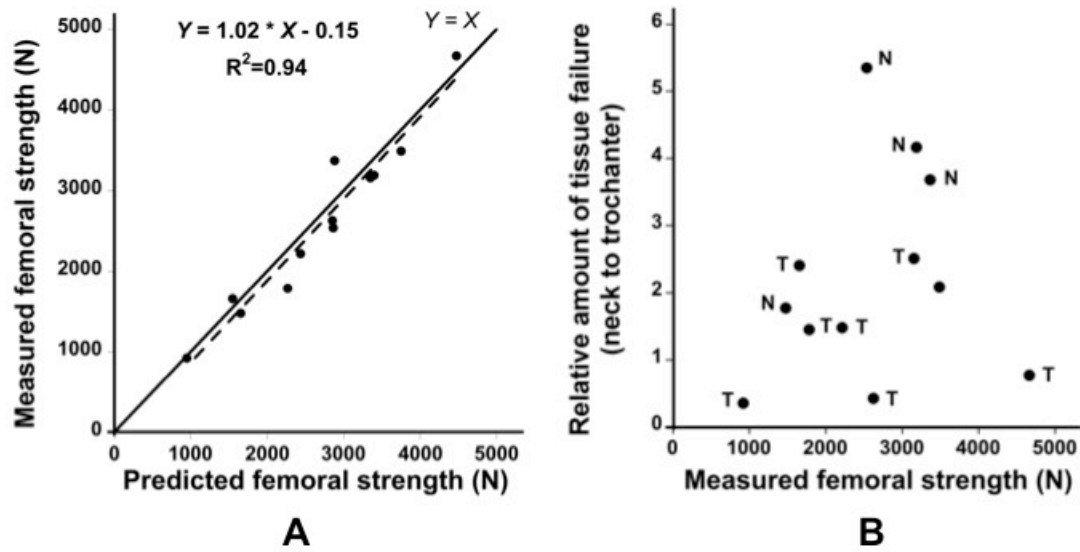


Figure 3-3: A) Association between finite element-predicted femoral strength and the experimental measurements from biomechanical testing ($Y = 1.02 X - 0.15$, $R^2 = 0.94$, $p < 0.0001$). B) Estimation of fracture type (neck vs. trochanteric) by the finite element analysis. The fracture types observed during biomechanical testing are denoted by *N* for a neck fracture and *T* for a trochanteric fracture.

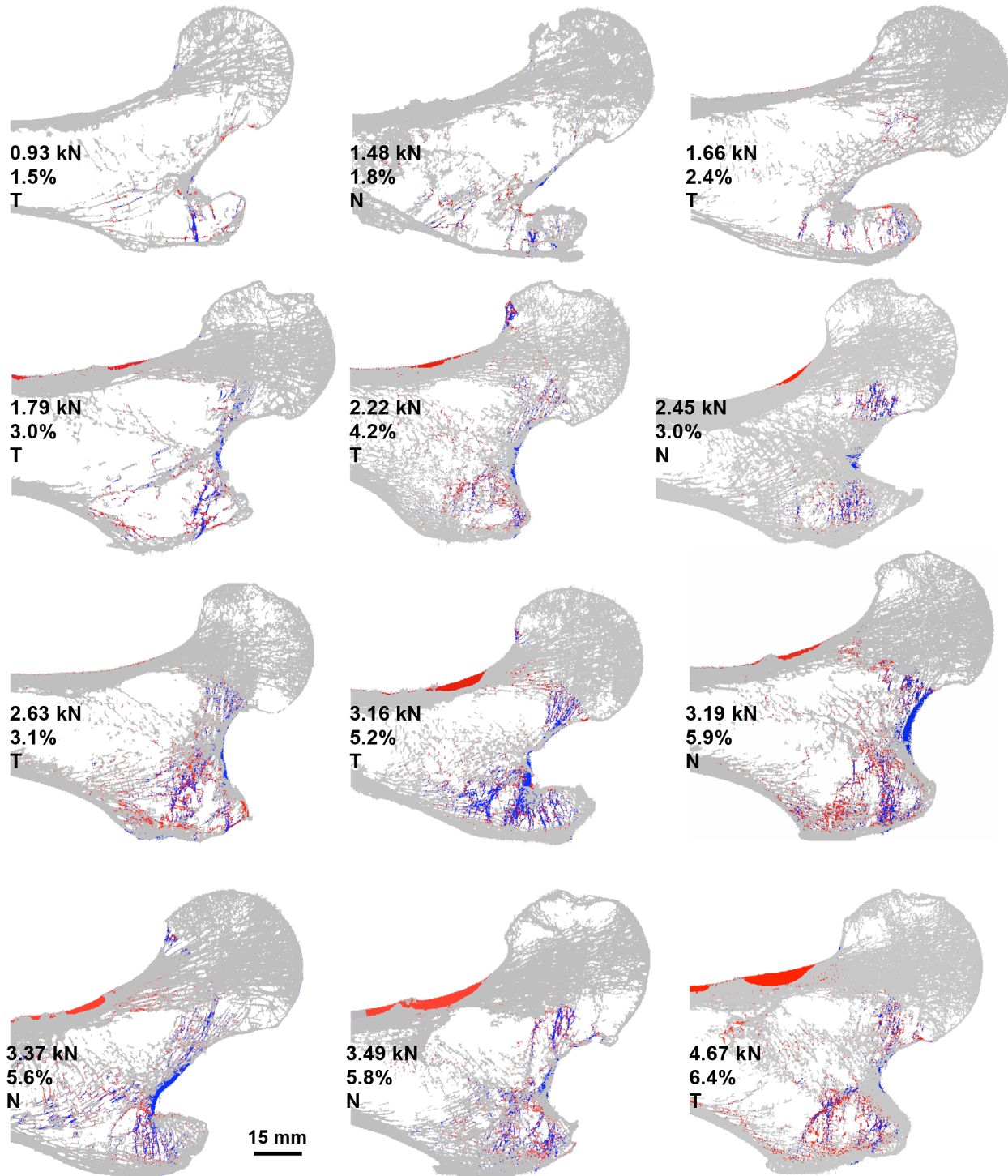


Figure 3-4: Mid-frontal projected 0.615 mm-thick sections from the human proximal femur showing the distribution of failed tissues (**Red**: tensile failure; **Blue**: compressive failure) at the structure-level 0.2%-offset yield point for each femur. The femurs are arranged in the order of increasing femoral strength, from the top left to the bottom right corners. Femoral strength and the proportion of failed tissue are given; the letters *N* and *T* denote if the experimentally observed fracture type was neck (*N*) or trochanteric (*T*). There is generally less failed tissue per unit bone mass for the weaker femurs, indicative of diminished structural redundancy. The reader is referred to the online article for the corresponding animations of the deforming microstructure.

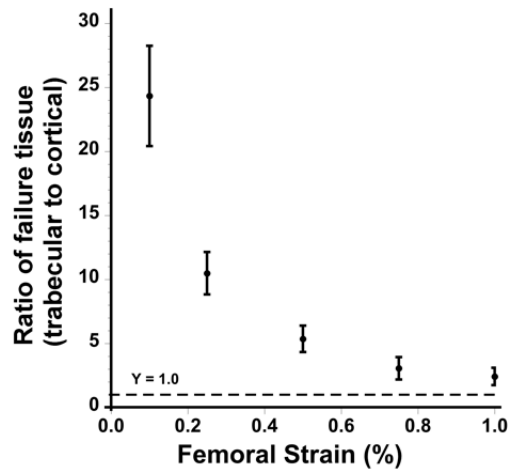


Figure 3-5: Ratio of the amounts of failed tissue in the trabecular to cortical bone, averaged over all 12 femurs, vs. femoral strain. Femoral strain is the overall strain of the femur, normalized by the structure-level 0.2%-offset yield strain. Error bars represent the 95% confidence intervals.

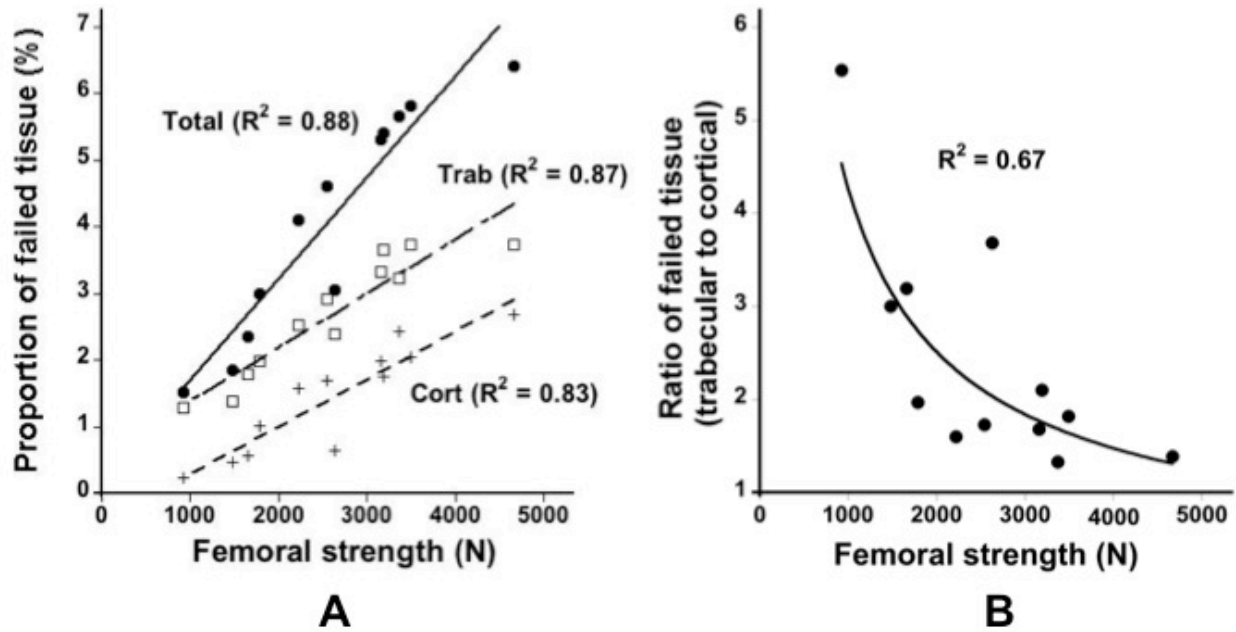


Figure 3-6: Tissue failure in the cortical versus trabecular bone: A) the proportion of overall failed tissue (as a percentage of the total amount of bone tissue) vs. experimentally-measured femoral strength ($p < 0.0001$, for all). B) ratio of the amounts of failed tissue in the trabecular to cortical bone, vs. experimentally-measured femoral strength ($R^2 = 0.67$, $p < 0.01$).

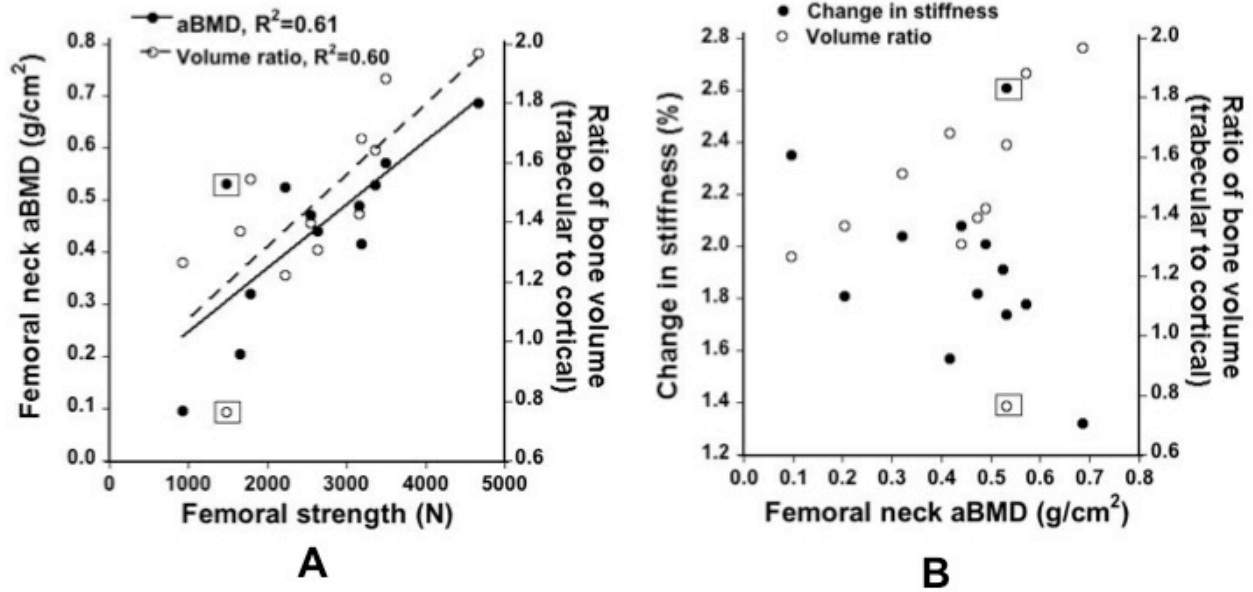


Figure 3-7: A) Variation in the femoral neck aBMD (from DXA) and the ratio of trabecular-to-cortical bone volume in the femoral neck, versus the measured femoral strength ($p < 0.01$, for both). B) Variation in the percent change in stiffness at 0.1% bone tissue failure — a quantitative measure of structural redundancy (a larger change in stiffness being indicative of less structural redundancy) — and the ratio of trabecular-to-cortical bone volume in the femoral neck, versus the femoral neck aBMD. The squared data denote one specimen that had a high femoral neck aBMD but low strength.

4. THEORETICAL BOUNDS FOR THE INFLUENCE OF TISSUE-LEVEL DUCTILITY ON THE APPARENT-LEVEL STRENGTH OF HUMAN TRABECULAR BONE³

4.1 Introduction

One fundamental issue in bone biomechanics is the influence of tissue-level ductility on the apparent-level strength behavior of trabecular bone. Tissue-level ductility is most easily characterized by the magnitude of the post-yield strain to fracture. While this post-yield strain decreases with aging for cortical tissue [25, 137-139] and is thought to influence whole-bone fragility [22], many details for trabecular bone remain unclear. In the only study of its type we are aware of, Hernandez *et al.* [76] tested 231 individual trabeculae from 32 cadavers to failure in tension, and found relatively large values of ultimate strain (mean \pm SD = 8.8% \pm 3.7%). Compared to average ultimate strains for human cortical tissue on the order of about 2% [25], this limited literature suggests that trabecular tissue may be much more ductile than cortical tissue. However, it is difficult to interpret the relevance of such findings without understanding the influence of tissue-level ductility on the apparent-level strength of trabecular bone. This multi-scale issue, which relates ductility at one scale to strength at a higher scale, has been well investigated for composites [140, 141] and cellular solid materials [142, 143], but less so for trabecular bone. Verhulp [144] used micro-CT-based finite element analysis to study the micro-mechanics of bovine trabecular bone and found no appreciable effect of variations in the assumed shape of the post-yield behavior of the tissue on the apparent-level strength. However, they did not address the degree of ductility, imposing no limit on the magnitude of the tissue-level strains. Thus, we investigated how the apparent-level trabecular bone strength and the underlying failure mechanisms are altered when the tissue-level failure behavior is changed from fully ductile to fully brittle — the two extremes of possible tissue-level ductility; we also assessed how these effects depend on typical population variations in bone volume fraction and microarchitecture. In this way, we provided theoretical bounds for the influence of tissue-level ductility on the apparent-level strength of human trabecular bone.

4.2 Methods

Specimen Preparation and Imaging:

We analyzed 20 specimens of human trabecular bone, taken from four anatomic sites, 16 cadavers, both sexes, and spanning a wide range of age and bone volume fraction (**Table 4-1**). The specimens were originally machined as 8 mm-diameter cylindrical cores along their principal trabecular orientation, and were scanned at a spatial resolution of 10-22 microns using micro-CT (n=15; Scanco Medical AG, Switzerland) or serial milling (n=5) [145]. For this analysis, we virtually extracted out a 5 mm cube from the central portion of each image and resampled all images to a 22-micron voxel size. Measures of bone volume fraction (BV/TV) and standard microarchitecture parameters [146, 147] were obtained from these specimens, the microarchitecture data available only for the 15 specimens scanned with micro-CT. These 15 specimens displayed substantial heterogeneity in the bone volume fraction and microarchitecture (Mean \pm SD: BV/TV=0.16 \pm 0.06, SMI=1.00 \pm 0.73, Conn.Den. = 5.78 \pm 2.86, Tb.N = 1.39 \pm 0.29, Tb.Sp = 0.70 \pm 0.14, Tb.Th = 0.17 \pm 0.03, Tb.(1/N).SD = 0.26 \pm 0.05, Tb.Sp.SD = 0.24 \pm 0.06, Tb.Th.SD = 0.06 \pm 0.01, and DA = 1.88 \pm 0.35) .

³ This study has been published in Journal of Biomechanics [78]

Finite Element Modeling:

Voxel-based finite element models were generated for each specimen by converting each image voxel in the 5 mm cube to an 8-noded brick element (22 micron element size). This element size fulfilled the convergence requirements [148, 149]. In each model, all finite elements were assigned the same hard tissue material properties, having an isotropic elastic modulus of 18.0 GPa [37], a Poisson's ratio of 0.3, and failure properties as described below. Displacement roller-type boundary conditions were applied to impose unconstrained uniaxial compression loading.

For each model, two separate non-linear finite element analyses were performed to simulate fully ductile and fully brittle tissue-level behaviors (**Figure 4-1**). For both types of analyses, kinematic large-deformation geometric non-linearity was included in the constitutive model [83, 96]. All analyses were performed using a highly scalable, implicit parallel finite element framework, Olympus [93] on a Sun Constellation Linux Cluster (Ranger; TACC, TX, USA). On average, each fully ductile analysis required about 100 CPU hours and each fully brittle analysis required about 450 CPU hours.

For the fully ductile case, as described in detail elsewhere (Bevill et al. 2006), we assumed tissue-level failure by yielding, using a rate-independent elasto-plasticity type model [130]. Such yielding comprised a modified von-Mises criterion with tension-compression strength asymmetry [37, 91], which was achieved by introducing pseudo-kinematic hardening to shift the yield envelope. The tissue-level yield strains of 0.33% in tension and -0.81% in compression were chosen [83]. The apparent-level yield strength was obtained from the computed apparent-level stress-strain curves using a 0.2%-offset criterion (**Figure 4-2**). Such measures of apparent-level yield strength have been well validated previously in experiments [83, 150] and are about 83% of, and highly correlated ($R^2=0.96$) with, ultimate strength [151].

For the fully brittle case, element yielding was not allowed and instead we used a quasi-nonlinear approach to simulate brittle fracture of any elements that exceeded the assumed tissue-level yield strengths in either tension or compression. In particular, an elastic analysis was performed to a specified apparent-level strain; stresses were computed at each element centroid, as was the overall apparent-level stress for the whole specimen. Once either the maximum or minimum principal stress at any element centroid exceeded the assumed respective tissue-level tensile or compressive yield strength, that element was assumed to fail in a brittle manner and we reduced its elastic modulus 100-fold for subsequent analyses. Using these reduced properties in all such failed elements, a new elastic analysis was then performed for the whole specimen to an incrementally higher apparent-level strain. This whole process was repeated until we generated an overall apparent-level stress-strain curve that displayed an ultimate point. Typically for each of these fully brittle analyses, 20 increments of apparent-level strain were applied, and thus 20 geometrically non-linear but otherwise elastic analyses were performed. The apparent-level ultimate strength was defined as the maximum stress on the computed apparent-level stress-strain curve. An apparent-level 0.2%-offset yield strength was not used for these brittle analyses since the corresponding yield strain was greater than the ultimate strain (**Figure 4-2**).

To aid in interpretation of the results, we also performed an ancillary parametric sub-study on three trabecular bone specimens wherein the tissue-level compressive strength was altered while keeping the tissue-level tensile strength constant.

Cellular Solid Analysis

To provide additional insight, we also used cellular solid theory [142] to derive an analytical expression for the ratio of brittle to ductile strengths. As described elsewhere [70, 142, 152], we assumed a 2D honeycomb-like structure with a hexagonal unit cell having side length L and thickness T , and accounted for tissue-level tension-compression strength asymmetry. As in the computer models, the tissue-level fracture strength was assumed to equal the tissue-level yield strength. Any kinematic large-deformation effects were ignored for analytical simplicity, and the dominant failure mode was assumed to be bending-type failure of the oblique struts. This analysis revealed the following equation for the ratio R of brittle, σ_{brit} , to ductile, σ_{duc} , apparent-level strengths:

$$\sigma_{\text{duc}} = \left\{ \frac{T}{L} \right\}^2 \left(\frac{1}{2\text{Cos}^2\theta} \right) \left(\frac{2C}{1+C} \right) \sigma_{y-t}^T ; \sigma_{\text{brit}} = \left\{ \frac{T}{L} \right\}^2 \left(\frac{1}{3\text{Cos}^2\theta} \right) \sigma_{y-t}^T ; R = \frac{\sigma_{\text{brit}}}{\sigma_{\text{duc}}} = \frac{1+C}{3C} \quad \text{Equation 1}$$

in which θ is the angle of the oblique struts, σ_{y-t}^T is the assumed tissue-level yield strength in tension, and C is the compressive-to-tensile ratio of the tissue-level yield strength.

Outcomes and Statistical Analyses

The main quantitative outcomes were the apparent-level strengths and corresponding strains, and bone volume fraction and the microarchitectural properties. We also quantified the proportion of failed tissue (at apparent-level strength), defined as the number of Gauss points exceeding the assumed tissue-level yield point divided by the total number of Gauss points in the model. In the ductile analysis, the simulated tissue failure occurred via *yielding* while in the brittle analysis, tissue failure occurred via *fracture*. However, for simplicity, we henceforth adopt the terminology '*failed tissue*' to denote failed tissue regardless of whether it failed by yielding or fracture. We also distinguished tissue failure by its mode, *i.e.* tensile vs. compressive. Non-linear and general linear regression models (JMP 9.0; SAS Institute, Cary, NC USA) were used to determine the effect of the ductile versus brittle behaviors on the strength outcomes, accounting for variations in bone volume fraction and microarchitecture.

To further aid in interpretation of our results, model predictions of apparent-level yield (and ultimate) strain were compared against the corresponding experimental data for the same 20 specimens used in the simulations. These experimental data were obtained previously [153, 154] from mechanical testing of the full cylindrical specimens from which the 5 mm-cube specimens were virtually extracted.

4.3 Results

Changing the tissue-level failure behavior from fully ductile to fully brittle substantially reduced the apparent-level strength of the trabecular bone, and did so to a similar degree across

all specimens regardless of bone volume fraction and microarchitecture. There was a strong non-linear correlation between the apparent strength and the bone volume fraction for both ductile ($Y=0.064X^{1.73}$, $R^2=0.98$, $p<0.0001$) and brittle ($Y=0.033X^{1.73}$, $R^2=0.96$, $p<0.0001$) behaviors. As a result of the similarity of exponents and the high R^2 values, the ratio of brittle to ductile strength (mean \pm SD = 0.56 ± 0.02) was almost constant across cohort ($R^2=0.99$ between the two strength measures). The slight inter-specimen variation in this ratio was moderately explained by SMI ($R^2=0.58$, $p<0.01$) and bone volume fraction ($R^2=0.44$, $p=0.01$). Since the brittle and ductile strengths were so highly correlated with each other, the correlation coefficients for the variation of brittle strength with microarchitecture were identical to those for ductile strength.

Changing the tissue-level failure behavior from fully ductile to fully brittle also substantially altered the failure mechanisms. At the point of apparent-level failure, on average, only a tiny proportion of the bone tissue had failed ($1.1\% \pm 0.4\%$) for the fully brittle bone, which was almost 16-fold less than for the fully ductile bone ($16.5\% \pm 6.5\%$, **Figure 4-3**). In general, the tissue that failed (*i.e.* yielded) in the fully ductile analyses subsumed the tissue that failed (*i.e.* fractured) in the fully brittle analyses (**Figure 4-4**). Further, for the fully ductile behavior, the tissue failed primarily in tensile mode at low bone volume fraction ($< 10\%$) and primarily in compressive mode at high bone volume fraction, whereas for the fully brittle behavior, the tissue failed primarily in tensile mode at all bone volume fractions (**Figure 4-5**).

Both our parametric finite element study and our cellular solid analysis indicated that increasing the tissue-level compressive strength compared to the tensile strength served to decrease the ratio of apparent-level brittle to ductile strength (**Table 4-2**). Further, the uniformity of the brittle-to-ductile strength ratio, as predicted by the finite element analyses for all $n=20$ specimens, was consistent with the cellular solid theory, which prescribed that this ratio depends only on the tissue-level tensile-compressive strength asymmetry ratio C and not at all on bone volume fraction or microarchitecture (see R in Equation 1).

Comparison of the apparent-level failure strains predicted by the model vs. measured by experiment confirmed that the finite element results bounded the real apparent-level trabecular bone behavior (**Figure 4-6**). There was good agreement between the experimental measurements of the apparent-level 0.2%-offset yield strain and the fully ductile predictions for those specimens having a bone volume fraction above about 0.20; at the lowest values of bone volume fraction (~ 0.10), the experimental measurements of the apparent-level 0.2%-offset yield strain fell to about half-way between the predicted yield strain for the fully ductile cases and the ultimate strain for the fully brittle cases.

4.4 Discussion

These computational results provide theoretical bounds on the effects of tissue-level ductility on apparent-level strength for human trabecular bone. One unexpected observation was the large magnitude of the effect — a two-fold change in the apparent-level strength — and another was its high degree of uniformity across the wide variety of specimens analyzed. The good agreement of the finite element results with those from our cellular solid analysis helps explain both of these unexpected results: if failure of individual trabeculae is dominated by large-deformation-related bending, then the ratio of the fully brittle to fully ductile apparent-level

strength is determined by the extension of plastic-type yielding across the cross-section of the individual trabeculae, an effect which is dominated by the ratio of compressive to tensile strength of the trabecular tissue and which is almost insensitive to bone volume fraction and microarchitecture. Taken together, these findings provide new insight into the theoretical effects of tissue-level ductility on the apparent-level trabecular bone strength.

The high degree of uniformity of the observed effect is noteworthy. While the main effect was largely constant across all specimens, the slight variation in the ratio of brittle to ductile apparent-level strength was partially explained by SMI ($r = -0.76$; $p < 0.01$) and bone volume fraction ($r = 0.66$; $p = 0.01$). Since SMI and bone volume fraction are significantly correlated to each other ($R^2 = 0.74$; $p < 0.001$), we speculate that due to its higher correlation, SMI might be the more mechanistic parameter. However, any effect of microarchitecture was small, as demonstrated by the small variation in the ratio of ductile to brittle strength observed across all 20 specimens despite a wide range of bone volume fraction and microarchitecture. Consistent with the finite element results, the analytical cellular solid theory prescribes that the ratio R of brittle to ductile apparent-level strength depends only on the tissue-level strength asymmetry ratio C and not at all on bone volume fraction or microarchitecture. The finite element results show that, for real trabecular microstructures, there is an influence of bone volume fraction and plate- versus rod-like microstructure on the mechanism by which post-yield behavior can influence apparent-level strength — but this is a small effect.

Analysis of the proportion and distribution of failed tissue helps explain the magnitude of the observed two-fold strengthening effect. Our results showed that the fully ductile behavior led to a 16-fold greater proportion of failed tissue compared to the fully brittle behavior, which translated to an almost two-fold higher apparent-level strength. The failure distribution patterns further indicate that there is more tissue-level failure mode by tension if the bone is fully brittle compared to fully ductile. Since bone tissue is weaker in tension than compression, brittle trabecular bone is therefore weaker than ductile bone because less tissue per unit mass of bone is required to fail in brittle bone, and because most of the failure that does occur in brittle bone is by the weaker tensile failure mode. Previous work has shown that the failure mechanisms for fully ductile tissue-level behavior for low bone volume fraction are strongly influenced by kinematic non-linear “large-deformation” effects [83, 96, 150], which render individual trabeculae more susceptible to tensile failure due to excessive bending. In contrast, for high bone volume fraction, the thick, plate-like trabeculae have a tendency to fail primarily in compression. This explains why, going from high to low bone volume fraction, we observed for the ductile bone a shift from compressive to tensile tissue-level failure modes.

Despite this new insight, we acknowledge that our analysis only provides theoretical bounds between two assumed extremes of tissue-level post-yield behavior and does not address the important question of how apparent-level strength could be affected by typical age-, population-, disease-, or treatment-related variations in real post-yield behavior. This remains a topic for future research. Despite our finding of the high degree of uniformity of the ratio of brittle-to-ductile strength, the comparison between our theoretical bounds and the real apparent-level yield strains suggests a possible interaction between bone volume fraction and ductility. In particular, at high bone volume fraction, the real tissue-level ductility may be sufficiently high as

to effectively be fully ductile. This would be consistent with the results from mechanical testing of individual trabeculae in tension which showed an average ultimate strain of about 8% [76], and also with results from time-elapsd micro-CT imaging studies of whale vertebral trabecular bone under compression testing [155], which showed individual trabeculae undergoing large deformations without actually fracturing. However, at low bone volume fraction, our results also suggest that low levels in the real tissue-level ductility in some individuals may reduce apparent-level strength. Consistent with this, there is much variation in reported measures of the ultimate strain of individual trabeculae, reaching values as low as 1.8% [76]. However, since only one study has been reported for tissue-level ductility for trabecular bone [76], more studies are needed in this area. In general, the effects of aging on the apparent-level strength of trabecular bone appear to be dominated by reductions in bone volume fraction (and associated changes in microarchitecture) [118]. One could speculate that if the ductility of trabecular tissue were to decrease with age, disease, or treatment in a subset of people — perhaps in those with reduced bone turnover (diminished remodeling rates) and low bone volume fraction who have accumulated mineralization, microdamage or crosslinks — then the data in **Figure 4-6** suggest there might be a potentially important role of such diminished tissue-level ductility in age-related reduction of bone strength, but this effect may only be important at low bone volume fraction.

The study has some limitations. First, the study was purely computational, and thus the model predictions await direct experimental validation. Second, although our models had sufficiently high spatial resolution for numerical convergence [148, 149], they did not include such micro-scale features as intra-specimen variation in mineral density and tissue material properties, or fine details of resorption spaces or microcracks. Although inclusion of such details would likely influence absolute values of any strength estimates [136, 156-160], it is not clear that their exclusion would appreciably influence the direct comparison between the two behaviors. On the one hand, it may be that such micro-scale effects might similarly influence the brittle and ductile failure mechanisms if failure of individual trabeculae is dominated more by overall load sharing across the trabecular network than by local material behavior; on the other hand, it is possible that fine geometric details of resorption spaces or microcracks might have a more deleterious “stress riser” effect in more brittle bone tissue. Clearly, additional research is required to resolve these issues. Third, to simulate the fully brittle case, we used an iterative quasi-nonlinear approach in which the elastic modulus of failed elements was reduced 100-fold after each step of the analysis. A more detailed way to simulate tissue-level brittle failure might include a 3D constitutive damage model within the framework of continuum mechanics [161-163]. Fourth, at the apparent level, we compared a 0.2%-offset yield strength (for ductile behavior) against an ultimate strength (for brittle behavior). Since the 0.2%-offset yield strength for human trabecular bone is highly correlated with the ultimate strength [151], the general trends here should remain valid, and the true ratio of fully brittle to fully ductile strength is likely lower than reported here. It is also possible that a reduction in tissue-level ductility might affect the ratio of apparent-level yield to ultimate strength. Finally, having established bounds of the effects of fully brittle vs. fully ductile tissue-level behavior on the apparent-level strength, it would now be interesting to explore intermediate cases of tissue-level ductility.

In summary, our computational study demonstrated that human trabecular bone is substantially weaker if the bone tissue is fully brittle compared to if it is fully ductile, reflecting an appreciable difference in the proportion and mode of tissue-level failure but an effect that was

otherwise constant across a wide range of bone volume fraction and microarchitecture.

Table 4-1: Specimen details for the final cohort.

Anatomic Site	No. of Specimens ⁺ (male/female)	Age (years)	Bone Volume Fraction (Mean \pm SD)
<i>Femoral Neck</i>	7 (4/3)	69 \pm 9	0.25 \pm 0.05
<i>Greater Trochanter</i>	3(3/0)	66 \pm 10	0.12 \pm 0.03
<i>Proximal Tibia</i>	4(4/0)	65 \pm 9	0.14 \pm 0.04
<i>Vertebral body</i>	6(4/2)	66 \pm 8	0.09 \pm 0.03
<i>Pooled</i>	20(15/5)	67 \pm 9	0.16 \pm 0.06

+ Number of trabecular bone cube specimens; altogether these specimens were taken from a total of 16 different cadavers

Table 4-2: The influence of variation in tissue-level strength asymmetry (C) on the ratio of brittle to ductile strength as predicted by both cellular solid theory and finite element analysis ($n=3$ specimens; $BV/TV = 8.8\%$, 17.2% , 26.8%).

Tissue-level			Apparent-level	
Compression (σ -comp) (MPa)	Tension (σ -tens) (MPa)	σ - comp/ σ - tens (C)	Brittle-to-Ductile strength	
			FE-prediction	Cellular solid theory
145.8	59.4	2.45	0.53 ± 0.03	0.47
102.6	59.4	1.73	0.57 ± 0.02	0.53
59.4	59.4	1.00	0.63 ± 0.02	0.67

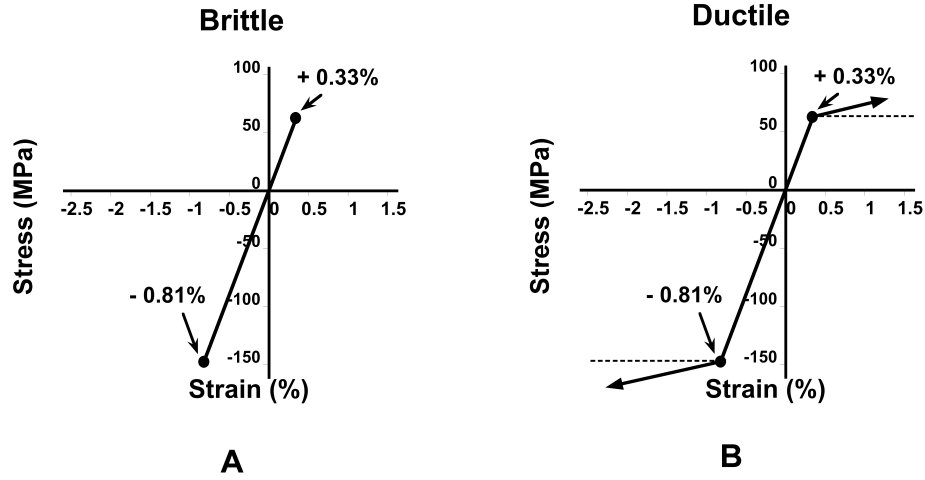


Figure 4-1: Material models depicting the stress-strain response at the tissue-level for: A) fully brittle, and B) fully ductile bone tissue.

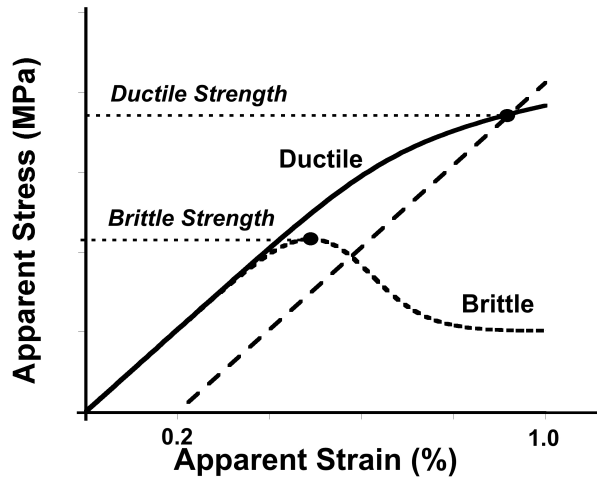


Figure 4-2: An example of a typical apparent-level stress-strain curve for trabecular bone corresponding to the fully ductile and fully brittle tissue-level behaviors, computed from the finite element analyses. For the ductile analysis, a 0.2%-offset criterion was used to define the apparent strength. For the brittle analysis, a 0.2%-offset criterion was not used because it exceeded the ultimate strain and thus an ultimate stress was used. The general shape of these curves did not depend on bone volume fraction.

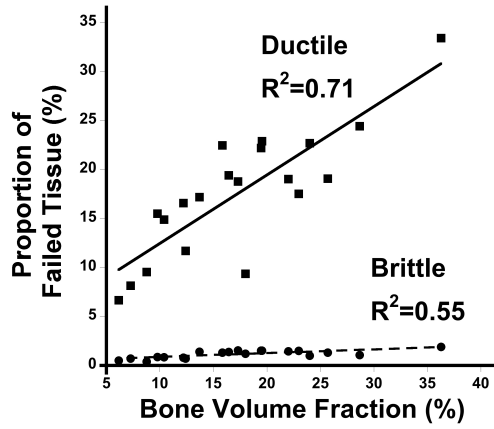


Figure 4-3: The variation in the proportion of failed tissue with bone volume fraction for brittle and ductile tissue-level behaviors.

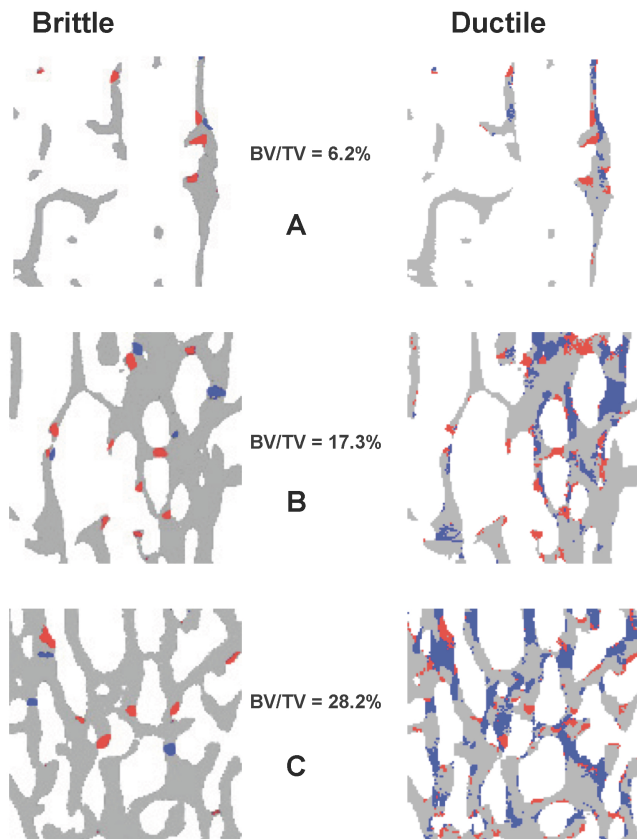


Figure 4-4: The spatial distribution of the failed tissue at the apparent-level strength for fully brittle and fully ductile behaviors for three different specimens: A) low bone volume fraction (6.2%); B) medium bone volume fraction (17.3%); and C) high bone volume fraction (28.2%). Blue: tissue failure in compressive mode; Red: tissue failure in tensile mode.

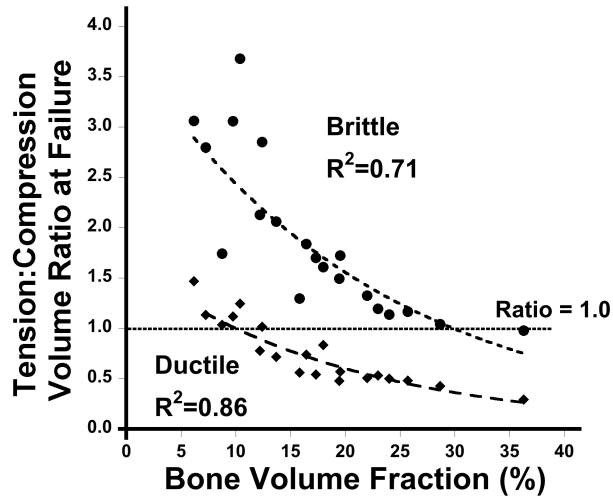


Figure 4-5: The ratio of the volume of failed tissue in tension to the volume of failed tissue in compression (at the apparent-level failure point) plotted versus the bone volume fraction, for the brittle and ductile behaviors. For brittle behavior, the ratio was greater than one for almost all specimens, reflecting a dominance of tensile failure mode at the tissue level. For ductile behavior, the ratio was less than one for most specimens, reflecting a dominance of compressive failure mode at the tissue level, particularly at bone volume fraction (>20%).

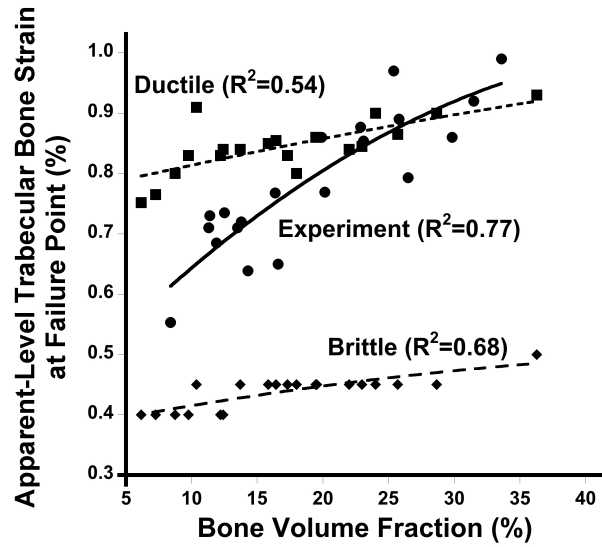


Figure 4-6: The variation in the apparent-level failure strain vs. bone volume fraction for simulated fully ductile ($R^2=0.54$) and fully brittle ($R^2=0.68$) behaviors from finite element analysis, and for real specimens from mechanical testing ($R^2=0.77$).

5. EFFECT OF TISSUE-LEVEL DUCTILITY ON VERTEBRAL AND FEMORAL STRENGTH

5.1 Introduction

The ductility of bone tissue is a measure of its ability to deform prior to fracture, and it varies substantially across the vertebrates. For example, bulla in Fin whale is essentially glass-like, fully brittle in nature, whereas, antler from Red deer can sustain extremely large deformations prior to fracturing; the human bone tissue ductility lies somewhere in between [164]. Within the humans alone, tissue-level ductility spans a large range — from 0.4-4.1% in cortical tissue [25] and 1.8-20% in trabecular tissue [76]. However, little is known regarding how such extreme variations in tissue-level ductility across the vertebrates in general and in humans in particular impacts the whole-bone strength in these organisms. Understanding the role of tissue-level ductility in the whole-bone failure behavior is key to gaining insight into the etiology of osteoporotic hip fractures in the humans [165, 166]. Addressing this issue is also relevant from an evolution perspective to understand how stark variations in tissue-level ductility across the vertebrates translate into different mechanical functions for their bones.

This fundamental issue has been previously investigated in human trabecular bone [78]. Theoretical bounds for the influence of tissue-level ductility on apparent-level trabecular bone strength were derived, which indicated that trabecular bone strength can vary about two-fold depending on whether the tissue fails in a fully ductile versus fully brittle manner. Even so, it remains to be seen as to how differently will tissue-level ductility manifest itself on whole bones, given the vast heterogeneity in whole-bone geometry and morphology across the population [23, 33, 34]. Further, the interaction between cortical and trabecular compartments, and the nature of external loading on the whole bones is also expected to alter their micromechanics, and might mediate the relationship between tissue-level ductility and whole-bone strength.

We, therefore, performed non-linear finite element analyses of the human whole-proximal femurs and vertebrae, to investigate how the whole-bone strength is altered when the manner in which tissue deforms is changed from fully ductile to fully brittle — the two hypothetical extremities of tissue-level ductility. Computer simulations make it feasible to compare the effects of tissue-level ductility on whole-bone strength in a highly controlled and pairwise manner, which is not possible with experiments alone due to destructive nature of strength testing. In this way, we provide theoretical bounds for the influence of tissue-level ductility on whole-bone strength.

5.2 Methods

Specimen Preparation and Imaging

This investigation was performed on sixteen human proximal femurs (age = 76 ± 10 years, range = 62-93 years; n = 12 female, n = 4 male) and twelve thoracic ninth (T9) vertebral bodies (age = 77 ± 11 years; n = 3 female, n = 9 male) that were obtained fresh-frozen from human cadavers, with no medical history of metabolic bone disorders. High-resolution images were acquired of each intact femur (XtremeCT; isotropic voxel size of 61.5- μm , Scanco Medical AG; Brüttisellen, Switzerland) and vertebra (micro-CT, isotropic voxel size of 30- μm , Scanco 80; Scanco Medical AG; Brüttisellen, Switzerland). The femur and vertebra images were coarsened to 82- μm and 60- μm voxel size, respectively, to facilitate computational analysis, and the hard tissue and marrow were segmented using a global threshold value. The trabecular and

cortical compartments within the whole bones were also identified [45, 167], using a two-dimensional ray-based search algorithm previously developed for the vertebral body [98], and modified by adding more search directions to account for the geometric complexity of the femur (IDL software suite, ITT Visual Information Solutions, Boulder, CO, USA).

Finite Element Modeling

Voxel-based finite element models [82] were generated for each specimen by converting each image voxel in the three-dimensional volumes of the bones to an 8-noded brick element (82- μm element size for femurs and 60- μm for vertebrae).

In each model, all finite elements were assigned the same tissue-level elastic and yield properties, having an isotropic elastic modulus of 7.3 GPa for the femurs and 5 GPa for the vertebra, a Poisson's ratio of 0.3, and yield strains of 0.81% in compression and 0.33% in tension [77]. The tissue-level elastic modulus of 7.3 GPa for the whole-femur and 5 GPa for whole-vertebra models were computed in our previous studies [45, 84] by calibrating the finite element-estimated 0.2%-offset yield strength — assuming fully ductile tissue-level behavior — with the corresponding experimentally measured strength to ensure $Y=X$ agreement. The difference in these calibrated values of elastic moduli is due to the different element sizes (60 μm for vertebra and 82 μm for femur) used in these models. For both types of analyses, kinematic large-deformation geometric non-linearity was included in the constitutive model [83, 96]. For computational efficiency, the bone tissue in the superior portion of the femoral head was not allowed to fail so as to eliminate spurious stress oscillations near the boundary conditions.

For each model, two separate non-linear finite element analyses were performed to simulate fully ductile and fully brittle tissue-level failure behaviors (**Figure 5-1**); the procedure to simulate fully ductile and fully brittle tissue-level failure behaviors has been described elsewhere in detail [78]. For the fully ductile case, we assumed tissue-level failure by yielding, using a rate-independent elasto-plasticity type model [130]. Such yielding comprised a modified von-Mises criterion with tension-compression strength asymmetry [37, 91], which was achieved by introducing pseudo-kinematic hardening to shift the yield envelope (**Figure 5-1a**). This type of tissue-level material behavior is well validated, and has been used in several studies on isolated trabecular bone cubes and cores [83, 116, 150, 168]. For the fully brittle case (**Figure 5-1b**), element yielding was not allowed and instead we used a quasi-nonlinear approach to simulate brittle fracture of any elements that exceeded the assumed tissue-level yield strengths in either tension or compression. In particular, a non-linear analysis was performed to a specified structure-level strain; stresses were computed at each element centroid, as was the overall structure-level reaction force for the whole specimen. Once either the maximum or minimum principal stress at any element centroid exceeded the assumed respective tissue-level tensile or compressive yield strength, that element was assumed to fail in a brittle manner and we reduced its elastic modulus 100-fold for subsequent analyses. Using these reduced properties in all such failed elements, a new elastic analysis was then performed for the whole specimen to an incrementally higher structure-level strain. This whole process was repeated until we generated an overall structure-level force-strain curve that displayed an ultimate point. Typically for each of these fully brittle analyses, 10 increments of structure-level strain were applied, and thus 10 non-linear analyses were performed. A typical ductile and brittle analysis for the femur during a

sideways fall had a runtime of 14 and 10 hours, respectively, with 2896 processors in parallel.

Displacement-type boundary conditions were applied both to the femurs and vertebrae (**Figure 5-2**). The proximal femurs were subjected to two different kinds of loading configurations: 1) a 15° sideways fall on the greater trochanter and 2) stance loading. To simulate a sideways fall on the greater trochanter, a structure-level compressive strain of 1.6% was applied to the medial aspect of the femoral head via a simulated layer of PMMA (elastic modulus 2.5 GPa; Poisson's ratio 0.3), this loading being sufficient to reach the 0.2%-offset yield point of each femur (**Figure 5-2a**). The layer of PMMA at the greater trochanter was constrained in the vertical direction to simulate contact between the trochanter and the floor. The distal end of the diaphysis was held fixed. In stance loading, a structure-level compressive strain of 2.4% was applied to the proximal aspect of the femoral head via a layer of PMMA such that the displacement vector made an angle of 20° with the femoral shaft (**Figure 5-2b**). The distal end of the diaphysis was held fixed. The vertebrae were subjected to uniaxial compression loading with a structure-level strain of 1% applied via layers of PMMA (**Figure 5-2c**).

Substantial computational infrastructure was required to perform non-linear finite element analyses. These simulations represented a technically challenging problem because of the huge size of each finite element model, further magnified by the inclusion of multiple bones (28 bones, two analyses per bone). Each finite element model contained up to 500 million degrees of freedom, and was solved using an implicit, parallel finite element framework [93]. Computer simulations were performed on the supercomputing resources (Stampede and Ranger) available at the Texas Advanced Computing Center, requiring a total CPU time of 325 years (a typical femur analysis required 12 hours of runtime using 2896 processors, and a typical vertebra analysis required 10 hours of runtime using 2172 processors).

Outcomes and Statistical Analyses

The main quantitative outcomes were the whole-bone strengths for the femurs and vertebrae. The whole-bone strength for fully ductile analysis was obtained from the computed structure-level force-strain curves using a 0.2%-offset criterion. Such measures of structure-level yield strength have been well validated previously using biomechanical testing both for the vertebra [45, 84] and femur [45, 84]. The whole-bone strength for fully brittle analysis was defined as the maximum load on the computed structure-level force-strain curve. A structure-level 0.2%-offset yield strength was not used for these brittle analyses since the corresponding yield strain was greater than the ultimate strain (**Figure 5-3**), both for the femurs and vertebra. The nature of structure-level force-strain characteristic curve was similar for the femurs and vertebra. In the subsequent sections, we will adopt the terminology “ductile strength” and “brittle strength” to refer to the whole-bone strength corresponding to the fully ductile and fully brittle tissue-level behaviors, respectively.

To characterize microstructural failure mechanisms, we quantified the proportion of failed tissue (at structure-level failure of the bone) by accessing the number and loading modes (tensile versus compressive) of the failed Gauss points in each finite element. The total proportion of failed tissue was defined as the number of Gauss points exceeding the assumed tissue-level failure (yield or fracture) point divided by the total number of Gauss points in the

model (excluding the PMMA). A similar calculation was performed for each of the cortical and trabecular compartments. In the ductile analysis, the simulated tissue failure occurred via *yielding* while in the brittle analysis, tissue failure occurred via *fracture*. However, for simplicity, we henceforth adopt the terminology '*failed tissue*' to denote failed tissue regardless of whether it failed by yielding or fracture.

Regression analysis was used to determine the correlation between the brittle and ductile strength of the bones. Mann-Whitney U test was performed to assess the effect of anatomic site (femur versus vertebra) and loading configuration (sideways fall versus stance) on the ratio of brittle to ductile strength, the relative amount of cortical versus trabecular tissue failure, and the relative amount of tensile versus compressive tissue failure. All statistical tests (JMP 10; SAS Institute, Cary, NC USA) were considered significant at $p < 0.05$.

5.3 Results

Changing the assumed tissue-level failure behavior from fully ductile to fully brittle substantially reduced whole-bone strength, both at the hip and spine (**Figure 5-4**). Whole-bone strengths for the fully ductile tissue-level failure behaviors spanned a large range, both at the hip and spine, with the weakest bone being approximately 5-fold weaker than the strongest bone (**Figure 5-4**). On average, the ratio of brittle to ductile strength was 0.61 ± 0.02 (mean \pm SD) for the vertebra for uniform compression loading, and 0.43 ± 0.04 and 0.62 ± 0.02 for the femur during a sideways fall and stance loading, respectively. This ratio was relatively uniform across all specimens of an anatomic site subjected to similar kind of loading. The brittle-to-ductile strength ratio was statistically similar for the vertebra in uniaxial compression and femur in stance loading ($p = 0.12$), but was significantly lower for the femur during a sideways fall ($p < 0.0001$).

Consistent with the uniformity of these strength ratios across bones, there was a high correlation between the brittle vs. ductile strengths both for the vertebra ($R^2 = 0.99$) and for the femur ($R^2 = 0.99$ stance; $R^2 = 0.96$ for fall). Further, there was no significant correlation between the brittle-ductile strength ratio and the measures of bone morphology (see **Table 5-1**, **Table 5-2** in Appendix).

Changing the tissue-level failure behavior from fully ductile to fully brittle also altered the microstructural failure mechanisms, with different effects observed in the spine vs. hip. The amount of failed tissue that led to structure-level failure of the bone was, on average, ten-fold lower for the vertebrae and five-fold lower for the femurs for the fully brittle compared to fully ductile tissue-level failure behavior (**Figure 5-5**). The locations of tissue-level failure for the fully ductile tissue subsumed the locations of tissue-level failure for the fully brittle tissue (**Figure 5-6**). Computing the amount of failed tissue in the cortical and trabecular compartments (**Figure 5-5a**) revealed that, after changing the tissue from fully ductile to fully brittle, the relative amount of trabecular versus cortical tissue failure remained unaltered in the hip, both for a sideways fall and stance loading ($p > 0.05$ for both), but increased four-fold in the spine ($p < 0.0001$). Evaluating the mode (i.e. tension vs. compression) of tissue-level failure (**Figure 5-5b**) demonstrated that, after changing the tissue from fully ductile to fully brittle, the relative amount

of tensile versus compressive failure increased significantly in the hip (2.5-fold increase for fall; $p < 0.0001$, and 1.5-fold increase for stance; $p = 0.001$), but was unaltered in the spine ($p > 0.05$).

5.4 Discussion

These results indicate that there can be a 40-60% difference in the whole-bone strength when the tissue-level failure behavior is assumed fully ductile compared to fully brittle. It is further elucidated that the role of tissue-level ductility is relatively uniform across all the specimens of an anatomic site subjected to similar kind of loading, suggesting that this effect might depend little on the bone geometry or morphology. However, the nature of external loading on the femur regulates the relationship between tissue-level ductility and whole-bone strength, the effect being greater during a sideways fall compared to stance loading of the femur. This study also provides mechanistic insight into the interaction between tissue-level ductility and structural redundancy in the bone by demonstrating that whole-bone failure requires five- to ten-fold more tissue to fail when the tissue is assumed fully ductile compared to when it deforms in a fully brittle manner. This finding illustrates that increase in bone fragility as a consequence of diminished structural redundancy may not necessarily be a consequence of only microstructural deterioration in the bone but may also occur with increase in tissue-level brittleness. Taken together, this study provides theoretical bounds on the influence of tissue-level ductility on whole-bone strength, and suggests that a complete embrittlement of the bone tissue can reduce the whole-bone strength by about 50% — an effect that is moderately regulated by external loading.

From a multi-scale strength perspective, relating tissue-level ductility to whole-bone strength is a relevant structure-function problem in which a material property at micron scale can influence a structural property at centimeter scale. Previous work conducted on this topic using isolated trabecular bone cubes has suggested that bone strength can vary up to two-fold depending on whether the bone tissue fails in a fully ductile versus fully brittle manner, the effect being independent of the bone volume fraction and microarchitecture of the trabecular bone [78]. However, whole bones are structurally complicated, in part due to the interaction between cortical and trabecular compartments [167, 169] that are microstructurally distinct [170, 171]. Further, the need to analyze multiple bones, from different anatomic sites — hip and spine — stems from substantial differences in the bone size [172], shape, external geometry, and internal microstructure [124, 126, 173] — and thus micromechanics — between these bones. All these factors, including the external loading configuration, might mediate the relationship between whole-bone strength and tissue-level ductility. It is in this spirit that we consider a heterogeneous cohort of bones and test them under multiple loading configurations.

A noteworthy finding of this investigation is the similarity in the role of tissue-level ductility in whole bone versus trabecular bone failure behavior despite notable differences in their size, shape, and morphology. Moreover, the uniformity in the effect of tissue-level ductility across all specimens — subjected to similar kind of loading — suggests that this effect might depend little on the bone external geometry or morphology, but accentuates during a sideways fall loading of the femur compared to stance. Overall, this study indicates that in theory the post-yield deformation of bone tissue can have notable impact on the whole-bone strength, especially when the tissue-level failure behavior is drastically affected. Although such extreme variations in

the ability of the bone tissue to deform are rare, they are observed under special circumstances, for example, as a consequence of disorders like osteogenesis imperfecta that occurs due to defect in type I collagen [174], or, when the bone is subjected to high doses of antiresorptive drug therapies like bisphosphonates that might lead to prolonged suppression of bone turnover and excessive mineralization of the bone tissue [175].

Analysis of the amount and distribution of failed tissue demonstrates a relationship between tissue-level ductility and structural redundancy in the bones. The amount of tissue-level failure that led to structure-level failure for the hip or spine was about five- to ten-folds lower when the tissue was assumed fully brittle compared to when it behaved in a fully ductile fashion. This indicates that the quantity of load-bearing tissue in the structure — that ultimately fails due to overload — is not only determined by bone mass, but is also contingent on the extent to which the tissue can deform prior to fracture. In addition, the regions of tissue-level failure within the bones were not overtly sensitive to the level of ductility, and considerable overlap was observed in the failed regions despite extreme alteration in the post-yield deformation characteristic of the tissue. Prior investigations on understanding the microstructural failure mechanisms in human bones have elucidated that microstructural deterioration — even after accounting for the effects of bone mass or bone mineral density — might lead to diminished structural redundancy in the bone, increasing bone fragility [45, 84]. From that viewpoint, this study demonstrates that increase in tissue-level brittleness might also be a potential mechanism that affects structural redundancy in the bone — and thus bone fragility, independent of the effect of microstructure.

This study also provides mechanistic insight into the role of tissue-level ductility in altering relative cortical versus trabecular tissue failure in the bone. On changing the manner of tissue deformation from fully brittle to fully ductile, it was established that the relative amount of cortical to trabecular tissue failure was unaltered in the hip, both for sideways fall and stance loading, but was altered for the spine. This fundamental difference between the hip and spine is essentially due to the different microstructural failure mechanisms in these bones. Whereas, trabecular tissue failure completely dominates the mechanisms of whole-vertebra failure regardless of the vertebral strength [84, 176], cortical tissue failure plays a prominent role during failure of the stronger femurs [45]. Therefore, any reduction in tissue-level ductility in the vertebra essentially has a greater impact on trabecular tissue failure but only a marginal impact on cortical tissue failure. In contrast, it seems to have an appreciable effect on both trabecular and cortical tissue failure in the femur. This finding clearly begs the question as to whether the change in tissue-level ductility would modify cortical-trabecular load-sharing in the vertebra, but not in the femur.

This study has a few limitations that must be realized while interpreting its findings. First, we have only simulated the two hypothetical extreme cases of tissue-level ductility: fully ductile and fully brittle. Given the large size effect of this variation and the fact that very few individuals in any population are expected to have extremely brittle or ductile bones, future studies must investigate the influence of typical population-variations in ductility on whole-bone strength. For example, limited data available on the measurements of human cortical and trabecular tissue-level ultimate strains have suggested that trabecular tissue ultimate strains typically vary between 1.8 – 20% [28, 76], and cortical tissue ultimate strain vary between 0.4 – 4.1% [25]. Therefore,

studies must be designed with the aim of simulating ultimate strains within these ranges of values. Moreover, the distinction between ductility in the cortical and trabecular tissue is also potentially important, since it is understood — albeit from a very limited data — that real trabecular tissue is more ductile than cortical tissue. This raises the possibility that whole-bone strength may be more influenced by ductility changes in the cortical tissue than in the trabecular tissue. None of these issues have been explored yet. Second, due to the limited sample size, care must be taken when generalizing the findings of this study. Although the samples of bones in this study spanned a wide range of strengths, and thus were sufficiently diverse to support the main findings of this study, it is always desirable to increase sample size to confirm the reported findings and to better probe the behavior of those femurs that reveal unusual characteristics. Third, in order to simulate a sideways fall or stance loading of the femur, we only considered specific cases of bone orientation such as the 15° internal rotation of the femur during fall or an angle of 20° between the loading direction and femoral shaft for stance. While these cases represent the most commonly observed loading orientations for a sideways fall [177, 178] or stance [107, 179], the physiological femur orientation is subject to vary across the population or between men versus women. Changing these assumptions as well as assuming intra- or inter-bone variation in tissue-level material properties will undoubtedly affect the impact of tissue-level ductility on bone strength, and perhaps will also alter the microstructural failure mechanisms.

In summary, we have shown through the use of massively-parallel, non-linear finite element simulations that the ability of the bone tissue to deform in a fully ductile versus fully brittle manner can have a substantial effect on the whole-bone strength, both at the hip and spine. Whereas this effect was relatively uniform across all specimens of an anatomic site subjected to similar kind of loading, it was significantly greater for the femurs during a sideways fall compared to stance loading. By providing mechanistic insight into whole-bone failure behavior, we provide the first the quantitative assessment of the different ways in which tissue-level ductility manifests itself on whole-bone strength — in terms of the cortical versus trabecular tissue failure and the mode of tissue-level failure. This study elucidates that increase in bone fragility as a consequence of diminished structural redundancy may not only be a consequence of microstructural deterioration but may also occur with increase in tissue-level brittleness.

5.5 Appendix

We determined the correlations between the ratio of brittle to ductile strength and selected measures of bone morphology, for both femurs and vertebra. Standard measures of bone volume and geometry were derived from the original micro-CT scans of the bones. Integral bone volume for the whole-bone was calculated as the total volume of all bone voxels in the whole-bone. Cortical and trabecular bone volume were defined as the total volume of bone voxels present in the cortical and trabecular compartments, respectively. For the femur, femoral neck axis length, neck-shaft angle, minimum femoral neck cross-sectional area, minimum femoral neck areal moment of inertia, and femoral head diameter, were measured as per published guidelines [128, 180, 181]. For the vertebra, we measured cross-section area of the mid-sagittal section, and the curvature [167].

The correlations between the brittle-to-ductile strength ratio and the measures of bone volume and geometry were not statistically significant ($p>0.05$), both for femurs (Table 5-1) and vertebrae (Table 5-2). This finding suggests that the effect of tissue-level failure behavior on whole-bone strength depends little on the bone morphology.

Table 5-1: Characteristics of the study population (mean, standard deviation) for the femurs (n=16) and correlation coefficients between selected outcomes and the brittle-to-ductile strength, both for a sideways fall and stance loading of the femurs.

Outcomes and variables (units)	Sample characteristics (n = 16)		Brittle-to-ductile strength	
	mean	SD	femur stance	femur fall
			<i>Pearson correlation coefficient (r)</i>	
Brittle-to-ductile strength femur stance	0.62	0.02	1.00	0.24
Brittle-to-ductile strength femur fall	0.43	0.04	0.24	1.00
Ductile strength stance (kN)	7.72	2.23	0.16	0.40
Ductile strength fall (kN)	2.62	1.02	0.03	0.31
<i>Morphology parameters</i>				
Total hip integral bone volume (cm ³)	42.8	8.31	0.01	0.10
Total hip cortical bone volume (cm ³)	17.3	3.68	0.11	-0.01
Total hip trab bone volume (cm ³)	25.5	5.34	-0.07	0.15
Femoral neck integral volume (cm ³)	7.93	2.16	0.53	0.28
Femoral neck cortical volume (cm ³)	3.28	0.99	0.47	0.06
Femoral neck trab volume (cm ³)	4.64	1.46	0.47	0.37
Trochanter integral volume (cm ³)	21.5	4.71	-0.30	0.11
Trochanter cortical volume (cm ³)	11.3	2.51	-0.12	0.06
Trochanter trabecular volume (cm ³)	10.2	2.70	-0.41	0.14
Total hip trab/cortical volume ratio	1.49	0.26	-0.22	0.16
Femoral neck trab/cort volume ratio	1.45	0.33	0.05	0.20
Trochanter trab/cortical volume ratio	0.91	0.20	-0.36	0.16
<i>Geometry parameters</i>				
Head diameter (cm)	2.21	0.13	-0.30	-0.15
Neck-axis length (cm)	6.24	4.05	0.25	-0.01
Neck-shaft angle (degrees)	126	5.13	0.35	-0.14
Neck cross-sectional area (cm ²)	7.10	1.14	0.05	-0.18
Neck areal moment of inertia (cm ⁴)	4.57	1.66	0.05	-0.15

Bolded values have $p < 0.05$. SD: standard deviation. $r = 0.64$ is the statistical significant limit.

Table 5-2: Characteristics of the study population (mean, standard deviation) for the vertebrae (n=12) and correlation coefficients between selected outcomes and the brittle-to-ductile strength for uniaxial compression loading of the vertebra.

Outcomes and variables (units)	Sample characteristics (n = 12)		Brittle-to-ductile strength
	mean	SD	<i>Pearson correlation coefficient (r)</i>
Brittle-to-ductile strength	0.61	0.02	1.00
Ductile strength (kN)	5.06	1.97	-0.29
<i>Morphology parameters</i>			
Total spine integral bone volume (cm ³)	4.82	1.33	-0.42
Total spine cortical bone volume (cm ³)	0.65	0.18	-0.49
Total spine trab bone volume (cm ³)	2.29	0.72	-0.42
Total spine trab/cortical volume ratio	3.58	1.04	-0.05
Vertical BV/TV	0.08	0.02	-0.32
Cortical thickness (mm)	0.42	0.09	-0.55
<i>Geometry parameters</i>			
Curvature (degree)	18.2	4.89	-0.21
Mid-sagittal cross-sectional area (cm ²)	1.79	0.49	-0.36

Bolded values have $p < 0.05$. SD: standard deviation. $r = 0.59$ is the statistical significant limit.

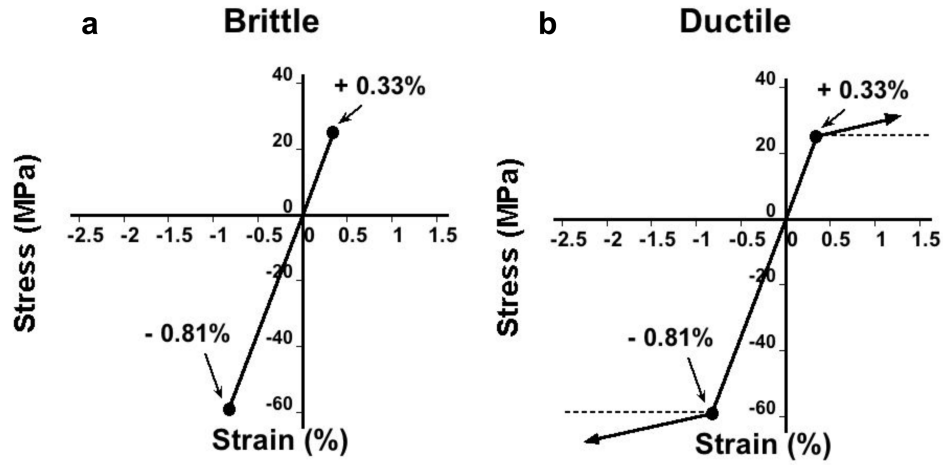


Figure 5-1: Material models depicting the stress–strain response at the tissue-level for: a) fully brittle, and b) fully ductile bone tissue.

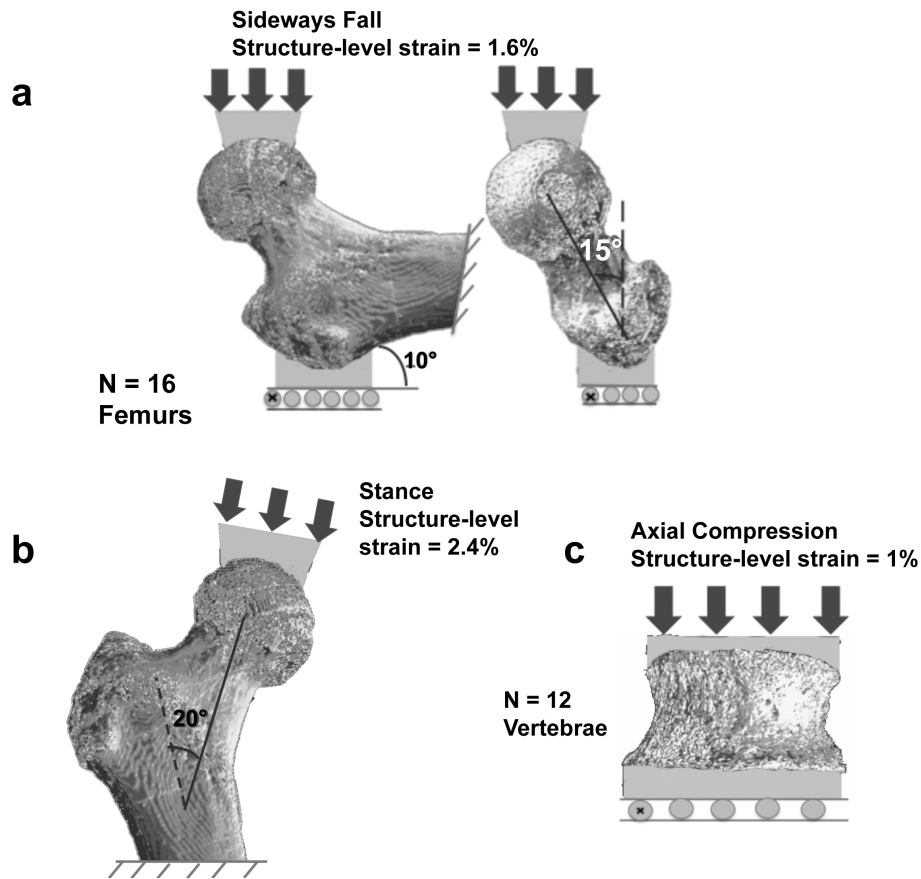


Figure 5-2: Boundary conditions used in finite element analysis to simulate: a) a sideways fall of the femur, b) stance loading of the femur, and c) uniaxial compression loading of the vertebrae.

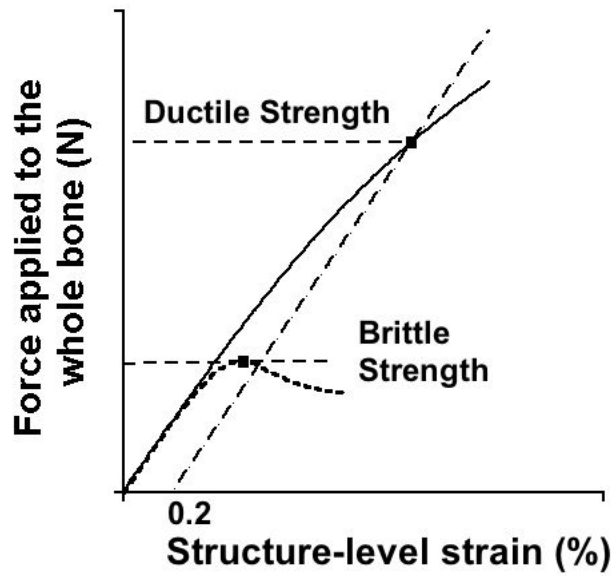


Figure 5-3: An example of a typical apparent-level stress–strain curve for trabecular bone corresponding to the fully ductile and fully brittle tissue-level behaviors, computed from the finite element analyses. For the ductile analysis, a 0.2%-offset criterion was used to define the apparent strength. For the brittle analysis, a 0.2%-offset criterion was not used because it exceeded the ultimate strain and thus an ultimate stress was used. The general shape of these curves did not depend on the anatomic site or loading configuration.

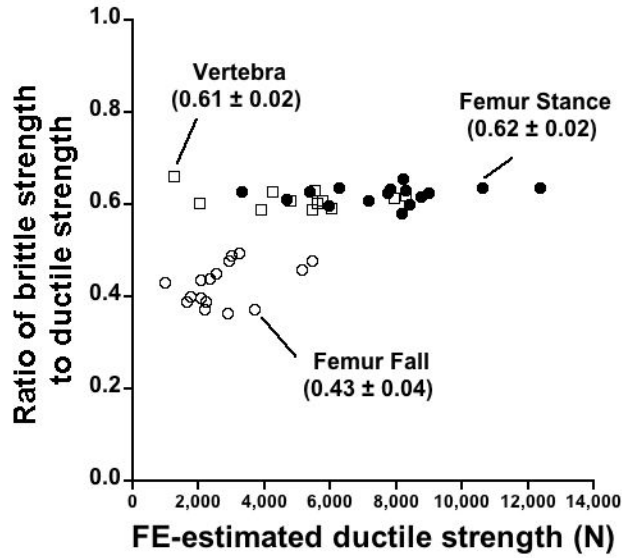


Figure 5-4: Variation in the ratio of whole-bone brittle to ductile strength across the specimens. The ratio was relatively uniform across all specimens but at the hip was larger for fall than stance loading. The specimens spanned a wide range in ductile (and brittle) strength indicating substantial heterogeneity in the bone external geometry and internal microstructure across the cohort.

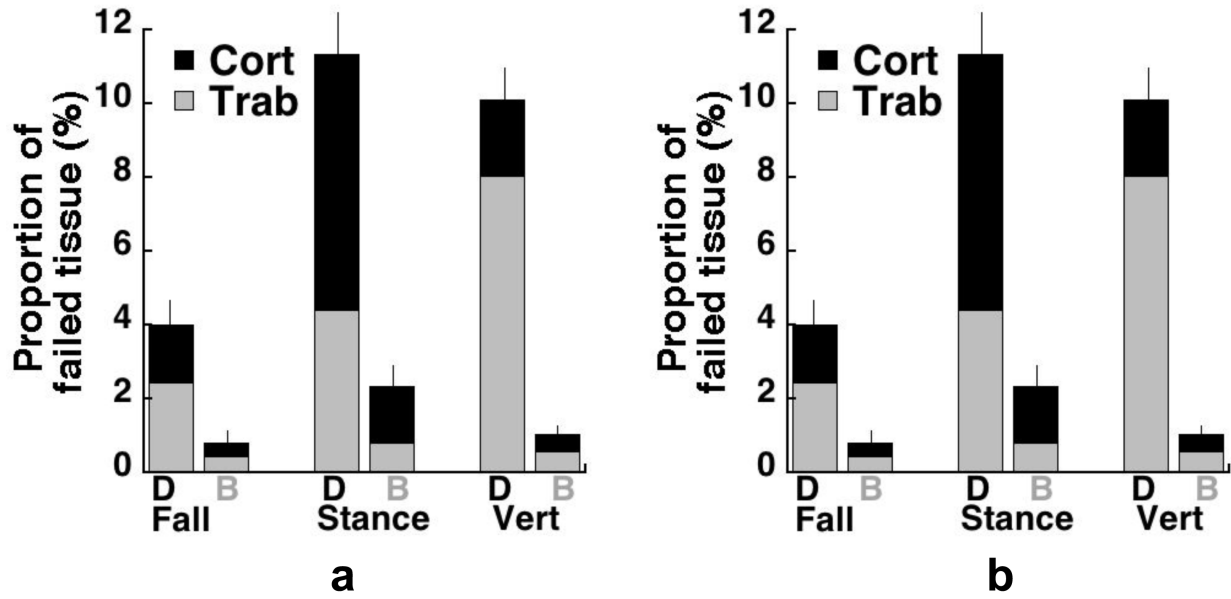


Figure 5-5: Variation in the total proportion of failed tissue when the tissue-level behavior is changed from fully ductile (D) to fully brittle (B): a) the contributions of cortical and trabecular tissue failure have been shown separately; b) the contributions of tensile and compressive tissue failure have been shown separately. In all cases, the total amount of failed tissue was much less for fully brittle behavior. Bars show 95% confidence interval.

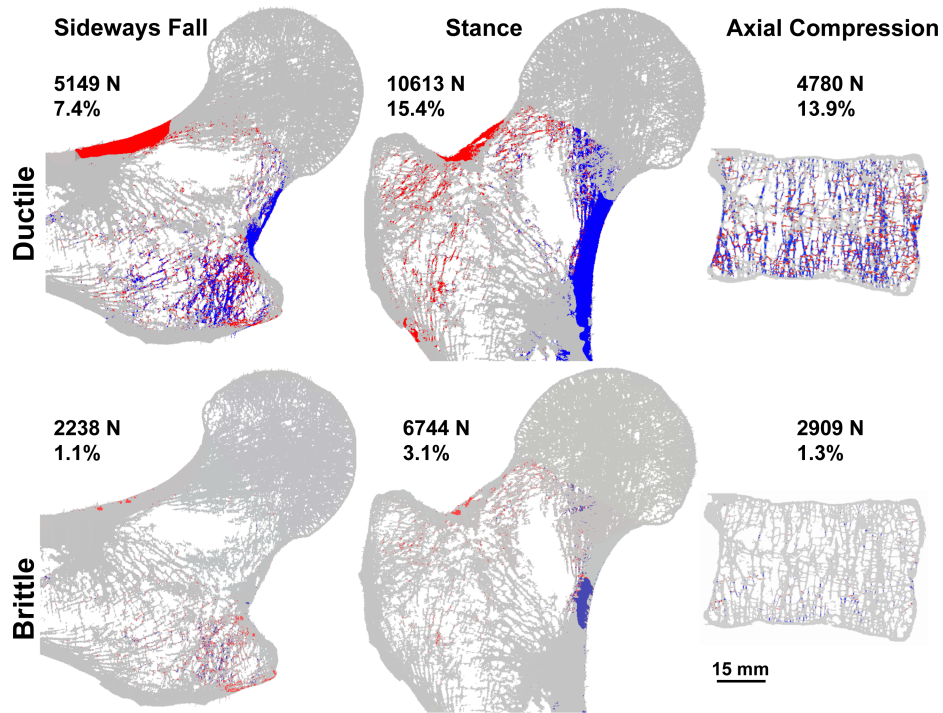


Figure 5-6: Mid-frontal sections of one proximal femur and mid-sagittal sections of one vertebra. (Colors depict locations of tissue-level failure. Blue: Compression. Red: Tension. Grey: No Failure). The amount of tissue-level failure (shown in %) required for overall bone failure was 5 to 10 times lower when the bone tissue was assumed to be fully brittle (bottom row) versus fully ductile (top row). Bone strength values are shown in Newton, N.

6. INFLUENCE OF TYPICAL POPULATION-VARIATIONS IN TISSUE-LEVEL DUCTILITY ON THE FEMORAL STRENGTH

6.1 Introduction

The ductility of bone tissue is a measure of its ability to deform before it eventually breaks and fractures. It is known to decrease with age for the cortical tissue [25], and varies appreciably across the population for the trabecular tissue [28, 76]. To date, only a few studies have measured ultimate strains for either trabecular or cortical tissue due to technical challenges associated with failure testing of the small samples of bone tissue [182]. This limited data indicates that real trabecular tissue is much more ductile than cortical tissue (**Figure 1-7**).

The ductility of bone tissue is a unique element of bone quality that is expected to influence bone fragility [20]. Therefore, understanding the role of tissue-level ductility in whole-femur failure behavior is essential to better understand the etiology of hip fractures. It was recently elucidated that varying the tissue-level failure behavior between the extreme cases of fully ductile and fully brittle tissue reduces the whole-bone strength by 40 – 60% — an effect that was uniform across all specimens of an anatomic site, but was relatively significant for femurs during a sideway fall than stance loading [183]. However, this study only simulated the hypothetical extreme cases of ductility, and also assumed same ductility for both the cortical and trabecular tissue. Making a distinction between cortical and trabecular tissue ductility is potentially important so as to determine their individual roles in the whole-bone failure behavior, and the etiology of hip fractures.

To address this issue, we used non-linear finite element analyses and conducted a parameter study by systematically varying the tissue-level ultimate strains to investigate how typical population-variations in tissue-level ductility influence femoral strength, and whether such variations in ductility are more influential for the cortical or trabecular bone — potentially important factors in the etiology of age-related hip fractures. In this way, we determined how the variation in femoral strength due to variations in only tissue-level ductility compare with typical inter-bone variations in the femoral strength across the population.

6.2 Methods

Specimen Preparation and Imaging:

This investigation was performed on four human proximal femurs (age = 67 ± 1 years, range = 66-68 years; n = 3 female, n = 1 male) that were obtained fresh-frozen from human cadavers, with no medical history of metabolic bone disorders. We used only four femurs because our previous investigation, which included 16 human femurs and 12 vertebrae, had concluded that the effect of tissue-level ductility on whole-bone strength is almost constant across all specimens of an anatomic site subjected to similar kind of loading [183]. High-resolution images were acquired of each intact femur (XtremeCT; isotropic voxel size of 61.5- μm , Scanco Medical AG; Brüttisellen, Switzerland) and vertebra (micro-CT, isotropic voxel size of 30- μm , Scanco 80; Scanco Medical AG; Brüttisellen, Switzerland). The femur images were coarsened to 82 μm to facilitate computational analysis, and the hard tissue and marrow were segmented using a global threshold value. The trabecular and cortical compartments were also identified, using a two-dimensional ray-based search algorithm [98] previously developed for the vertebral body, and modified by adding more search directions to account for the geometric

complexity of the femur (IDL software suite, ITT Visual Information Solutions, Boulder, CO, USA).

Finite Element Modeling:

Voxel-based finite element models [82] were generated for each specimen by converting each image voxel in the three-dimensional volumes of the bones to an 8-noded brick element (82 μm element size for femurs). Displacement-type boundary conditions were applied to the proximal femurs to simulate a sideways fall on the greater trochanter (**Figure 6-1**). This loading configuration was chosen because tissue-level ductility is understood to have a greater impact on whole-bone strength for a sideways fall compared to stance loading [183]. For each femur, we performed a parameter study, in which the varied parameter was the assumed value of the tissue-level ultimate strain, both for the cortical and trabecular tissue. All other tissue-level properties were kept constant: all finite elements were assigned the same hard tissue material properties, having an isotropic elastic modulus of 7.3 GPa [45], a Poisson's ratio of 0.3, and yield strains of 0.81% in compression and 0.33% in tension [77]. The effective elastic modulus of 7.3 GPa for whole-femur models was determined by calibrating the finite element-estimated 0.2%-offset yield strength — assuming fully ductile tissue-level behavior — with the corresponding experimentally measured strength to ensure $Y=X$ agreement [45]. Our material constitutive model included kinematic large-deformation geometric non-linearity effects [83, 96].

The material model for both cortical and trabecular tissue was bilinear in nature and assumed identical tissue-level elastic and yield properties (**Figure 6-2**), the only difference being the tissue-level ultimate strains. The trabecular and cortical tissue ultimate strains simulated in this study were chosen based on the values reported by Hernandez [76] and McCalden [25], respectively (**Figure 1-7**). Hernandez performed tensile testing on 231 samples of single trabeculae ($n=32$ donors; age: 20-93 years) extracted from human vertebra and found high inter- and intra-donor variability in the trabecular tissue ultimate strains (range: 1.8–20%, mean \pm SD = $8.8 \pm 3.7\%$), with no association between the donor age and trabecular tissue ductility. Although, recently Carretta [28] also performed failure testing on trabeculae extracted from the human femurs, they did so only for 32 trabeculae ($n=2$ donors) and moreover reported ultimate strains within the range specified by Hernandez. To measure cortical tissue ultimate strains (range: 0.4 – 4.1%; mean \pm SD = $2.2 \pm 0.9\%$), McCalden performed a comprehensive study on 235 cortical specimens ($n=47$ donors; age: 20-102 years) and reported an age-related decline in cortical ductility. Nine combinations (3 cortical \times 3 trabecular) of tissue-level ultimate strains were simulated for each femur: the mean value and the mean \pm 1SD values. On account of higher variability in the trabecular tissue ductility, we also simulated mean \pm 2SD values of trabecular ultimate strains for one femur that was randomly chosen from the cohort, making it a total of fifteen combinations (3 cortical \times 5 trabecular) of tissue-level ultimate strains for this bone (**Table 6-1**). Additionally, the ultimate strain of the bone tissue was assumed to be the same in both tension and compression.

For each finite element model, and for each combination of tissue-level ultimate strain, a non-linear finite element analysis was performed using an iterative quasi-nonlinear approach. Per iteration, a fully non-linear finite element analysis was performed to a specified structure-level strain using a fully ductile material model that could by itself only simulate element-level

yielding, but not fracture. However, after each iteration, stresses were computed at each element centroid, and once either the maximum or minimum principal stress at any element centroid exceeded the assumed respective tissue-level tensile or compressive ultimate strength, the element was assumed to have fractured. We reduced its elastic modulus 100-fold for subsequent analyses. Using these reduced properties in all such fractured elements, a new non-linear analysis was then performed for the whole specimen to an incrementally higher structure-level strain. This whole process was repeated until we generated an overall structure-level force–strain curve that had exceeded its 0.2%-offset yield strength. Typically for each of these quasi-nonlinear analyses, 8 to 10 increments of structure-level strains were applied, meaning that 8 to 10 non-linear finite element analysis iterations were performed per specimen per combination of tissue-level ultimate strains.

Models contained up to 500 million degrees of freedom and were solved using an implicit, parallel finite element framework. Computer simulations were performed on the supercomputing resources (Stampede and Ranger) available at the Texas Advanced Computing Center, requiring a total CPU time of 325 years (a typical femur analysis required 12 hours of runtime using 2896 processors, and a typical vertebra analysis required 15 hours of runtime using 2172 processors).

Outcomes and Statistical Analyses

The main quantitative outcomes were the femoral strengths. The femoral strength was obtained from the computed structure-level force-strain curves using a 0.2%-offset criterion. Such measures of structure-level yield strength have been well validated previously in experiments and are highly correlated with ultimate strength [45]. To characterize the microstructural failure mechanisms, we quantified the proportion of yielded and fractured tissue (at structure-level strength) by accessing the number and loading modes (i.e., tension versus compression) of the yielded and fractured Gauss points in each finite element. The total proportion of yielded tissue was defined as the number of Gauss points exceeding the assumed tissue-level yield strength divided by the total number of Gauss points in the model (excluding the PMMA). A similar calculation was performed to calculate the proportion of fractured tissue. For simplicity, we henceforth adopt the terminology ‘*failed tissue*’ to denote all the bone tissue that has failed either by yielding or fracture. The total proportion of failed tissue in the cortical and trabecular compartments were also computed.

Percentage variations in the femoral strength and the amount of failed (yielded and fractured) tissue with the variation in tissue-level ductility were computed. Distinction was also made between the tissue-level failures in the cortical versus trabecular compartment. All statistical tests (JMP 10; SAS Institute, Cary, NC USA) were considered significant at $p < 0.05$.

6.3 Results

Across the four bones, the femoral strength for the mean values of the tissue-level ultimate strains (cort: 2.2%, trab: 8.8%) spanned a large range (1,735 N – 4,100 N), the strongest bone being approximately 2.5-fold stronger than the weakest bone. When the cortical and trabecular tissue ultimate strains were simultaneously varied by ± 1 SD about their mean values

there was only a 10-12% variation in the femoral strength (**Figure 6-3**). Altering only the cortical tissue ultimate strain by ± 1 SD about its mean varied the femoral strength by $4\pm 1\%$ (**Figure 6-4a**), whereas, a ± 1 SD variation in only the trabecular tissue ultimate strain altered the femoral strength by $7\pm 1\%$, these variations being almost constant across the bones (**Figure 6-4b**). Additionally, varying only the trabecular tissue ultimate strain for one bone by ± 2 SD about its mean varied the femoral strength by $16\pm 2\%$ (**Figure 6-4b**).

The majority of the tissue-level failure in the bone at its structure-level failure occurred by tissue-level yielding compared to fracture. Across the four bones, for the mean values of the tissue-level ultimate strains, $96\pm 1\%$ of the total tissue-level failure occurred by yielding while only $4\pm 1\%$ occurred by fracture (**Figure 6-5a**). When the cortical and trabecular tissue ultimate strains were simultaneously varied by ± 1 SD about their mean values, there was only a $6\pm 1\%$ variation in the relative proportion of yielded to failed tissue in the femurs (**Figure 6-5b**), the variations being substantially higher for -1 SD change in the ultimate strains compared to +1 SD change. Altering only the cortical tissue ultimate strain by ± 1 SD about its mean varied the relative proportion of the yielded to failed tissue by $5\pm 1\%$ whereas a ± 1 SD variation in only the trabecular tissue ultimate strain altered the femoral strength by just 1% (**Figure 6-5b**). However, altering only the trabecular tissue ultimate strain by ± 2 SD about its mean value varied the relative proportion of yielded to failed tissue by $8\pm 2\%$, the variations being substantially higher for -1 SD change in the trabecular tissue ultimate strain compared to +1 SD change (**Figure 6-5b**).

The effect of varying cortical and trabecular tissue-level ultimate strains on the total proportion of tissue-level failure in the bone differed between the bones (**Figure 6-6**). When the cortical and trabecular tissue ultimate strains were simultaneously varied by ± 1 SD about their mean values, there was a 30-45% variation in the total proportion of tissue-level failure in the bone. Across the four bones, altering only the cortical tissue ultimate strain by ± 1 SD about its mean changed the total proportion of tissue-level failure by $12\pm 5\%$ (**Figure 6-6a**), whereas, a ± 1 SD change in only the trabecular tissue ultimate strain varied the total proportion of tissue-level failure by $22\pm 4\%$ (**Figure 6-6b**). On average, variation in the amount of total tissue-level failure was always greater with the change in trabecular ultimate strain compared to cortical ultimate strain.

6.4 Discussion

In the current study, we sought to determine the influence of typical population variations in tissue-level ductility on the overall bone strength using micro-CT-based, nonlinear finite element analysis of the whole-proximal femurs. Computer simulations made it feasible to compare the effects of varying tissue-level failure behavior on whole-bone strength in a highly controlled and pairwise manner, which is infeasible with experiments alone due to destructive nature of strength testing. Femoral strength was estimated for several combinations of the simulated cortical and trabecular tissue-level ultimate strains, and it was found that typical population variations in tissue-level ductility account for only 10-12% of the femoral strength during a sideways fall on the greater trochanter — the typical variations in trabecular ductility having a larger effect than the typical variations in cortical ductility. In comparison, the inter-

bone variation in femoral strength across the population was quite substantial, the strongest femur being 2.5-fold stronger than the weakest femur. Elucidating the microstructural failure mechanisms at the structure-level failure revealed that the majority of the tissue-level failure in the bone occurred by yielding and tissue-level fracture gained mechanistic relevance only when the trabecular ductility was considerably low — by up to 2 SD below its mean. Further, it was also elucidated that the variations in trabecular ductility influence the amount of tissue-level failure more than the variations in cortical ductility. Taken together, these findings provide new insight into the relative role of typical population-variations in cortical and trabecular tissue-level ductility in the whole-bone strength and the underlying microstructural failure mechanisms.

The most interesting finding of this study is the modest impact of typical population variations in tissue-level ductility on the femoral strength for a sideways fall loading of the femur. It is well appreciated that the fundamental determinants of bone strength are the bone mass, morphology, and the tissue-level materials properties [22, 24]. However, currently there is little understanding of which of these factors is the most influential in explaining the vast variations in bone strength that is typically across elderly populations. Of these key factors, studies have mainly focused on investigating the role of bone mass [184], geometry [185], and microstructure [45] during hip fractures. For example, DXA-derived bone mineral density, a measure of bone mass and a clinical predictor of fracture risk, has been shown to explain approximately 50-70% of the variations in the bone strength [58, 86]. Similarly, the proportion of trabecular to cortical bone in the neck [45], the cortical bone morphological parameters like thickness and porosity [50, 51], the trabecular bone volume fraction, and the femoral head diameter and neck-shaft angle [127], are examples of some of the measures of bone microstructure and geometry that are known to have substantial association with the femoral strength. In contrast, little has been done to explore the role of tissue-level ductility — a key aspect of tissue-level material behavior — in whole-bone strength. Recently, it was reported that altering the tissue-level failure behavior from fully ductile to fully brittle can substantially impact the whole-bone failure behavior and can reduce the femoral strength by an almost constant amount of 60% during a sideways fall loading [183]. However, it is clear from the ultimate strain measurements of the real bone tissue that it is neither fully ductile nor fully brittle, and that trabecular tissue might be much more ductile than the cortical tissue (**Figure 1-7**). Therefore, assuming the same values of ductility for both cortical and trabecular tissues — as in our previous study — might lead to unreasonable alteration in the overall micromechanics of the femur. This study is therefore relevant in the sense that it is the first investigation to simulate the real values of tissue-level ultimate strains, and to suggest that typical population variations in the tissue-level ductility may account for only modest variations in femoral strength compared to between-population variations in bone mass or morphology.

Acknowledging the distinction between the tissue-level failure properties of the cortical and trabecular bone enabled us to investigate their relative importance on the overall structure-level failure behavior of the femurs. The findings in this study clearly demonstrate that variations in the trabecular ductility have a greater influence on the femoral strength and the tissue-level failure compared to variations in the cortical tissue ductility. This is an interesting outcome since the general understanding dictates that cortical bone is the major load-carrying component in the human femur [62, 63, 103, 105, 112], and thus variations in the failure properties of the cortical

tissue would be expected to have a potentially greater impact on the overall bone strength compared to variations in the failure properties of the trabecular tissue. However, given that tissue-level failure generally initiates in the trabecular bone during a sideways fall loading of the femur and quantitatively exceeds the cortical tissue-level failure regardless of the bone strength [45], the findings presented here are not entirely unexpected. Despite this, it is clear that there is only a modest difference between the relative influence of trabecular and cortical tissue ductility on the femoral strength. Overall this finding suggests that environmental or therapeutic factors that affect trabecular tissue ductility more than cortical tissue ductility might be of greater relevance in understanding the etiology of fall-related hip fractures since they might have a greater impact on the overall femoral strength.

The ability of our computer models to simulate both fracture and yielding of the bone tissue makes it feasible to evaluate their relative roles at the microstructural level. Our analyses suggest that an overwhelming majority of the tissue-level failure occurs by yielding whereas only a marginal proportion of the tissue fails by fracture. This finding seems to be consistent with the experimental observations by Fyhrie and colleagues [120] who reported a low incidence of microfracture (tissue-level fracture) of vertically oriented trabeculae in the trabecular bone, even after a substantial mechanical overload. Previously, Yeh and Keaveny [186], using finite element analysis, made a similar observation and suggested that if the ultimate strain of individual trabeculae was greater than 2%, microdamage (tissue-level yielding) rather than microfracture would be the primary mode of damage accumulation in the trabecular bone. In complete agreement with Yeh, we found that when the trabecular tissue ductility was reduced to 1.4% — that is, two SD below its mean — there was a marked increase in the tissue-level fracture within the bone and 20-30% of the overall tissue-level failure occurred by fracture. However, since human trabecula are understood to be highly ductile across the majority of the population [76], and are capable of withstanding large deformations prior to fracture [155], the findings reported in this study clearly support the assertion that tissue-level fracture is rare.

There are certain limitations in this study that should be realized while interpreting the results. Most importantly, this study has been performed on only four human cadaveric femurs. Due to the limited sample size, findings of this study must be generalized with utmost caution. Although the four bones considered in this study are diverse, and span a wide range in strength, it is always desirable to increase the sample size to confirm the reported findings. The choice of using only four femurs was based on the outcome of our previous study, with sixteen cadaver femurs and twelve vertebrae, which had concluded that the effect of tissue-level ductility on whole-bone strength is almost constant across all specimens of an anatomic site subjected to similar kind of loading [183]. Secondly, we have only simulated a sideways fall loading of the femur in this study — and that too a specific case of femur physiological orientation in which the bone is internally rotated by an angle of 15° in the transverse plane. It is expected that the underlying failure mechanisms will drastically change when the nature of external loading on the bone is altered, and so will the role of cortical versus trabecular bone in the whole-bone strength. Even so, it seems highly unlikely that these changes would have any major repercussions in the modest role of tissue-level ductility variations in the femoral strength. Finally, in this study we have only varied the cortical and trabecular tissue ductility by ± 1 SD about its mean except for one femur for which we have also simulated the ± 2 SD variations in the trabecular tissue

ductility. Statistically, a variation of 1 SD about the mean covers only 68% of the total population variations whereas a 2 SD change accounts for 95% of the variations across the population. Although a higher variation in tissue-level ductility would certainly accentuate the corresponding variations in the femoral strength, we believe that those variations would still be modest in comparison to the multiple-fold variations in strength that are typically observed across any elderly population.

Table 6-1: The combinations of tissue-level ultimate strains that were simulated.

Cort (%)	Trab (%)	mean - 2SD ⁺	mean - 1SD	mean	mean + 1SD	mean + 2SD ⁺
		1.4	5.1	8.8	12.5	16.2
mean - 1SD	1.3	1.3	1.3	1.3	1.3	1.3
		1.4	5.1	8.8	12.5	16.2
mean	2.2	2.2	2.2	2.2	2.2	2.2
		1.4	5.1	8.8	12.5	16.2
mean + 1SD	3.1	3.1	3.1	3.1	3.1	3.1

⁺ the values of trabecular tissue ultimate strains that were simulated only for one femur.

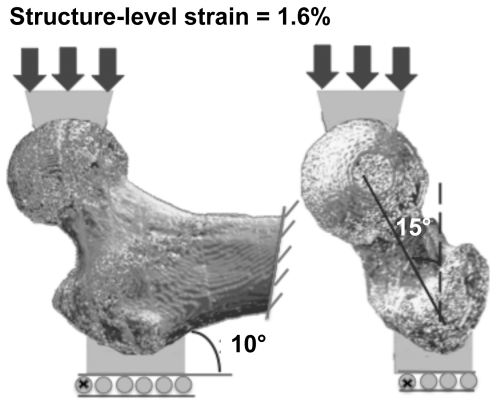


Figure 6-1: Boundary conditions used in finite element analysis to simulate a sideways fall. The femoral diaphysis axis is set to an angle of 10° with respect to the horizontal (left), and the femur is internally rotated by an angle of 15° (right).

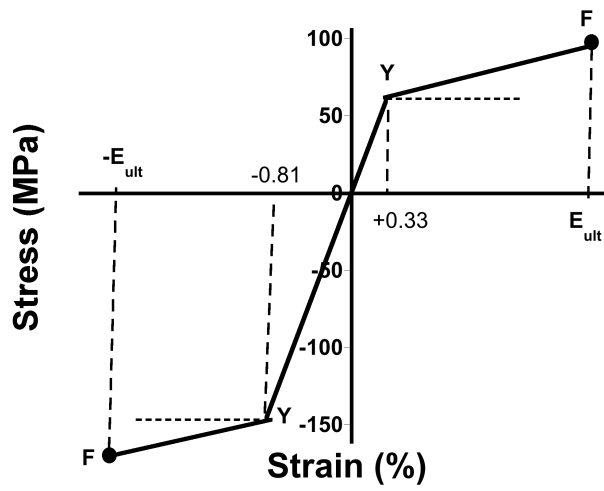


Figure 6-2: Material model depicting the stress–strain response at the tissue-level for both the cortical and trabecular tissue. E_{ult} represents the tissue-level ultimate strain. It was assumed same in tension and compression, and was different for the cortical vs. trabecular tissue. Y represents the tissue-level yield point and F represents tissue-level ultimate point.

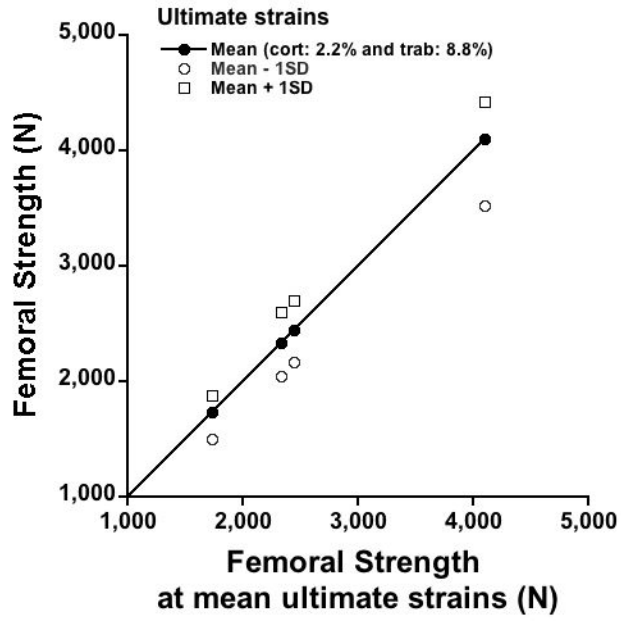


Figure 6-3: Variation in the femoral strength on simultaneously altering the trabecular and cortical tissue-level ultimate strains by ± 1 SD about their mean values.

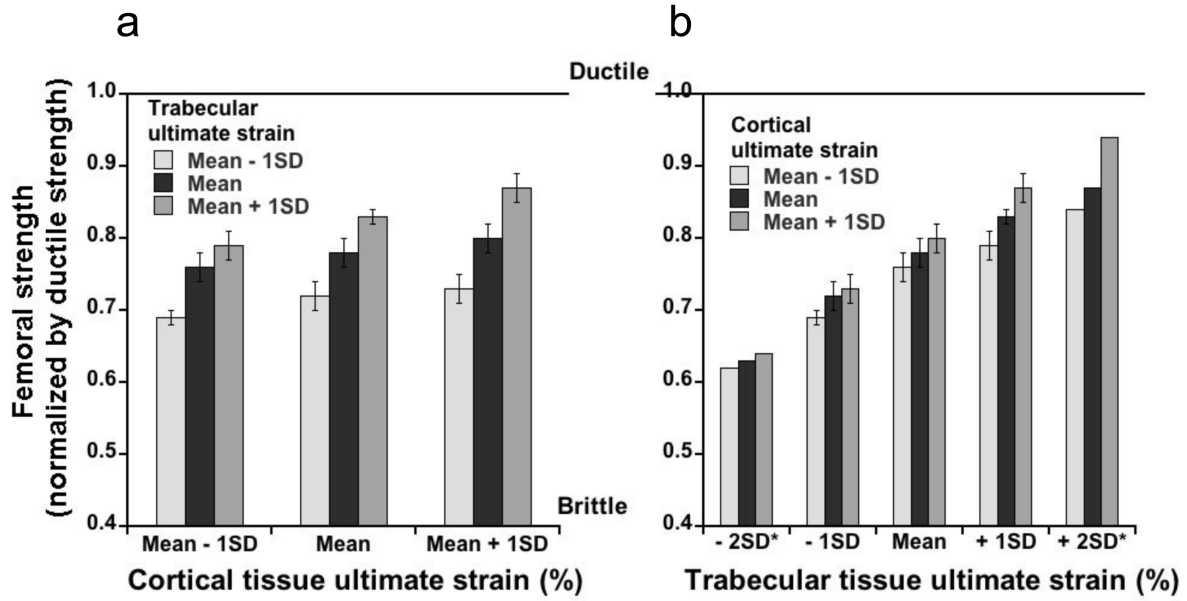


Figure 6-4: Variation in the femoral strength on altering a) only the cortical tissue-level ultimate strain by ± 1 SD, b) only the trabecular tissue-level ultimate strain by ± 1 SD and ± 2 SD. * represents the values of trabecular tissue ultimate strains that were simulated for only one femur.

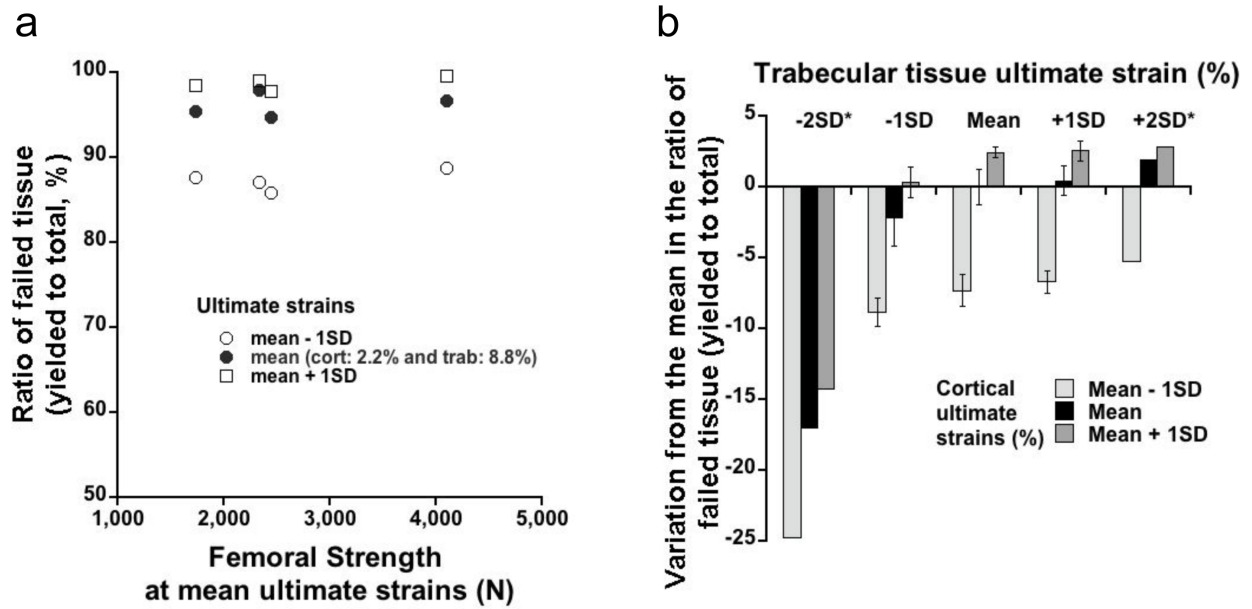


Figure 6-5: Variation in the relative proportion of yielded to failed tissue in the bone when a) both the cortical and trabecular tissue-level ultimate strains are simultaneously varied by ± 1 SD, b) only the trabecular tissue-level ultimate strain is varied by ± 1 SD and ± 2 SD. * represents the value of trabecular tissue ultimate strains that were simulated for only one femur.

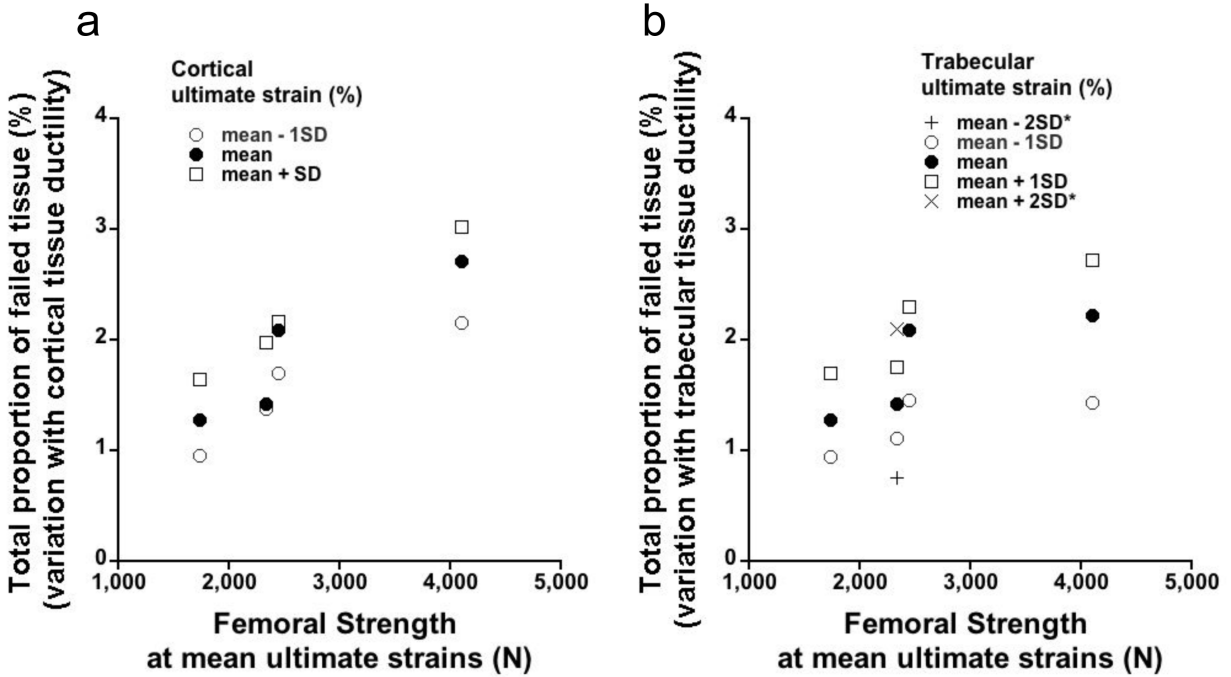


Figure 6-6: Variation in the total proportion of tissue-level failure when a) only the cortical tissue-level ultimate strain is varied by ± 1 SD, keeping the trabecular tissue ultimate strain fixed at its mean (8.8%), b) only the trabecular tissue-level ultimate strain is varied by ± 1 SD and ± 2 SD keeping the cortical tissue ultimate strain fixed at its mean (2.2%). * represents the values of trabecular tissue ultimate strains that was simulated for only one femur.

7. CONCLUSIONS

The overall goal of this research was to enhance the current understanding of the micromechanics of human proximal femur and the etiology of hip fractures. The findings of this research are relevant both from scientific and clinical viewpoints. From a basic-science perspective, substantial insight was gained into the microstructural failure mechanisms of the proximal femur and how they vary with the degree of structural redundancy in the bone. Patterns of load-sharing and load-transfer between the cortical and trabecular compartments in the human femoral neck were elucidated so as to determine the relative contributions of these compartments to the load-carrying capacity of the femur. This research also provided key mechanistic understanding of the relationship between tissue-level failure behavior and structure-level bone strength. From a clinical perspective, the results of this research have provided novel insight regarding morphological measures of femoral strength and the diagnosis of hip fractures.

In Chapter two, the relative role of cortical versus trabecular bone in the load-carrying capacity of the proximal femur was investigated. This is a fundamental but poorly understood issue in both basic-science and clinical biomechanics. However, little research has been done to directly quantify cortical-trabecular load-sharing in the femoral neck. We addressed this issue using micro-CT-based, linear, elastic finite element analysis of the whole-proximal femurs. Axial and bending load-sharing in the femoral neck were quantified and the associated spatial distributions of stress were elucidated for two separate loading configurations of the femur — a sideways fall and stance. For both loading modes, we found consistent patterns of load-transfer in the proximal portion of the femoral neck and patterns of uniform load-sharing in the distal portion. The pattern of normal stress distribution in the distal neck, where the highest (tensile and compressive) stresses occurred in the cortex—farthest away from the neutral axis of the bone—was indicative of fully-developed, beam-bending behavior distally, consistent with a region of relatively uniform load-sharing along the neck. In contrast, the highest normal stresses in the proximal neck occurred in the trabecular bone, consistent with a region of load-transfer. These findings are relevant since they provide unique insight into the micromechanics of the femoral neck, and clearly elucidate the mechanisms by which high stresses can develop in the cortical and/or trabecular bone tissue within the femoral neck.

Combining the latest advances in micro-CT imaging, high-resolution finite element modeling, and biomechanical testing to improve understanding of the etiology of hip fractures, Chapter three aimed at elucidating failure mechanisms of the human proximal femur during a sideways fall impact. In this investigation, we first performed micro-CT-based, geometrically and materially non-linear finite element analysis on cadaveric human femurs to estimate the femoral strength, and the amount and location of tissue-level failure at structure-level failure of the bone. The same femurs were also biomechanically tested in the lab to determine their failure load. A very high correlation was obtained between the experimentally measured and finite element-estimated measures of femoral strength, supporting the validity of the finite element simulations used in this dissertation. Computer simulations revealed that failure of a tiny proportion of the bone tissue led to initial structure-level failure of the femur. Interestingly, it was consistently observed across all the femurs that trabecular tissue failure occurred earlier and was more prominent than cortical tissue failure, and dominated in the very weakest femurs. A noteworthy finding in this chapter was that femurs with low measured strength relative to their

areal BMD had a low proportion of trabecular bone compared to cortical bone in the femoral neck and thus low structural redundancy.

The results presented in Chapter three are key to advancing the field of bone biomechanics beyond the current limitations imposed by bone mineral density. The findings in this chapter lead to the hypothesis that the proportion of trabecular bone compared to cortical bone in the femoral neck is a morphological measure of structural redundancy in the femur and we recommend that this hypothesis be tested in a large clinical study, consisting of participants from different age groups, genders, and races. If true, it would provide a better alternative for fracture risk assessment compared to the DXA-derived bone mineral density, which is currently the clinical gold-standard. In this context, one other key challenge perhaps for the researchers would be to develop an imaging modality that would make it feasible to obtain morphological measurements in a clinical setting.

Taken together, the results from Chapters two and three have practical implications regarding the relative importance of cortical vs. trabecular bone for *in vivo*, morphological analysis of femoral strength and fracture risk. Although Chapter two suggested that cortical bone has a substantial load-bearing role for the majority of the length of the femoral neck, findings in Chapter three indicated that measures of cortical bone microstructure such as the “femoral neck cortical mass” were only weakly associated with variations in femoral strength across individuals. Our findings also indicated that the role of trabecular microstructure was mediated by bone mass and density. *In vivo*, morphological assessment of femoral strength and fracture risk should therefore focus on the aspects of the microstructure that satisfy following criteria: 1) They are significant predictors of femoral strength even after adjusting for bone mineral density; 2) They reflect the biomechanical behavior of the femur; and 3) They exhibit wide variations across individuals. In light of these findings, we suggested a new determinant of femoral strength that satisfies these criteria: the proportion of trabecular bone compared to cortical bone in the femoral neck. Apart from the clinical significance of this work, the analysis of the deformation and failure mechanisms in the femur is an important step in understanding the etiology of hip fractures.

In Chapters four to six, we explored the influence of tissue-level ductility — an important aspect of bone quality and a determinant of bone fragility — on bone strength, for isolated trabecular bone cubes and whole bones. This is an important multi-scale issue that relates a material property at lower scale (microns) to a structural property at higher scale (millimeter or centimeter, depending on the sample). The rationale for using samples from multiple length scales was to understand whether tissue-level failure behavior manifests itself differently for different structures. Given that whole bones possess greater morphological and geometrical heterogeneity compared to cube-shaped samples of trabecular bone and are exposed to different kinds of external loading conditions within the physiological environment, the main objectives for these chapters were to understand how bone morphology, overall external geometry, and the nature of external loading mediate the relationship between tissue-level ductility and overall bone strength. The findings presented in these chapters are clinically relevant since they indicate how the age-, disease-, and treatment-related variations in cortical and/or trabecular tissue ductility would impact hip fragility.

Chapter four is the only study in this Dissertation that was performed on cube-shaped, isolated trabecular bone samples. The main objective in this chapter was to comprehend the role of tissue-level post-yield behavior on the apparent-level strength of trabecular bone. To gain insight, we compared the apparent-level strength of trabecular bone for the hypothetical cases of fully brittle (fracture with no tissue ductility) versus fully ductile (yield with no tissue fracture) failure behavior of the trabecular tissue. It was found that the apparent-level ultimate strength for the brittle behavior was only about half the value of the apparent-level 0.2%-offset yield strength for the ductile behavior, and the ratio of these brittle to ductile strengths was almost constant, approximately 56%. As a result of this small variation, although the ratio of brittle to ductile strengths was positively correlated with the bone volume fraction (BV/TV) and structure model index (SMI), these effects were small. Chapter four therefore concluded that the apparent-level strength behavior of human trabecular bone can vary appreciably depending on whether the tissue fails in a fully ductile versus fully brittle manner, and this effect is largely constant despite appreciable variations in bone volume fraction and microarchitecture.

Akin to Chapter four, in Chapter five we derived theoretical bounds for the variations in whole-bone strength. The sample cohort was extremely diverse and heterogeneous, and consisted of human proximal femurs and vertebrae. The femurs were virtually tested for two different loading configurations — a sideways fall and stance. Using massively-parallel finite element simulations on whole bones, it was revealed that there was a 40-60% reduction in bone strength when the manner in which tissue deforms was altered from fully ductile to fully brittle. The results of this chapter elucidated that the relationship between tissue-level ductility and whole-bone strength depends little on the bone geometry or morphology, but varies with the nature of external loading. The findings in Chapters four and five are of special interest from a clinical perspective since they suggest that it might be important to essentially identify those individuals who have extremely low levels of tissue ductility since they would have very low bone strength and therefore would be highly vulnerable to fragility fractures.

Chapter six was aimed at understanding how typical population-variations in tissue-level ductility influence femoral strength, and whether such variations in ductility are more influential for the cortical or trabecular bone. To answer these questions, a parameter study was conducted using micro-CT-based finite element analysis of four human proximal femurs. For each femur, combinations of tissue-level ultimate strains were simulated: the mean value and the mean \pm 1SD value, separately for the cortical and trabecular bone. The results indicated that there was only a 10–12% variation in the femoral strength when the cortical and trabecular tissue ultimate strains were simultaneously varied by one standard deviation about their mean values, typical variations in only the trabecular ductility had a larger effect on the femoral strength compared to typical variations in only the cortical ductility. Mechanistically, the failure mechanisms were dominated by tissue-level yielding compared to fracture, with 96% of the tissue-level failure occurring by yielding and 4% by fracture at the mean values of tissue-level ultimate strains. However, when the trabecular ductility was reduced to two standard deviations below its mean, about 20-30% of the tissue-level failure occurred via fracture. Overall, the findings in this chapter suggest that, typical population-variations in tissue-level ductility have only a modest influence on the whole-femur failure behavior, the trabecular ductility being more influential than the cortical ductility.

While interpreting the findings of Chapter six, it must be appreciated that very few studies have reported ultimate strains for the trabecular tissue. Although these investigations have tested a large cohort of trabeculae from multiple donors — given the challenges associated with failure testing of small bone samples — their findings may still not be truly representative of the entire population. In this context, one key challenge for researchers in bone biomechanics now lies in conducting further studies on measuring mechanical properties of the bone tissue, to verify the existing findings and to generate new data that will also essentially help determine if tissue-level ductility for trabecular bone varies with such factors as aging, diseases or treatments.

There research presented in this Dissertation has several strengths. First, the massively parallel, geometrically and materially non-linear simulations of failure of whole-proximal femurs (up to 800 million degrees of freedom) incorporating the latest advances in efficient solver algorithms [93] and state-of-the-art supercomputing technology places this research at the forefront of current efforts in computational bone mechanics. Second, this research used both high-resolution finite element modeling and biomechanical testing in order to exploit the unique capabilities of each technique. This combined approach provided new insight into micromechanics of the whole-proximal femur, a feature that differentiates this research from recent work that either used clinical-CT-based finite element models or simply considered statistical correlations when studying structure-function relationships in the whole femurs [133, 187]. Third, we analyzed multiple femurs, exhibiting a wide range of bone morphology, thereby accounting for biological heterogeneity and providing a reasonable degree of external validity to the computer simulations. Fourth, we performed high-resolution micro-CT imaging (61.5- μm spatial resolution) to reduce partial volume effects on the accuracy of microstructure measurements in the trabecular bone and to capture cortical thickness and porosity. Failure to do so could pose a serious challenge in elucidating microstructural deformations during mechanical overload of the bone. For example, large-deformation effects in trabecular bone such as the bending and buckling of slender, rod-like trabeculae, and the potential buckling of thin superior-lateral cortex [50] are key mechanisms that influence hip fragility. Currently, a large body of literature that uses clinical-CT scans to understand the etiology of age-related fractures and estimate treatment efficacy fails to capture these effects.

Future work in two potential areas is recommended to extend the relevance of the work presented in this dissertation. One important area is improving the current non-linear finite element analysis approach. The findings in Chapters two to six, for most part, are limited only to structure-level yielding, which essentially exhibits only initial failure of the bone; however, the biomechanical mechanisms of structure-level post-yield behavior and eventual fracture might be equally relevant and insightful, and must be probed to further the current understanding of hip fracture etiology. In this regard, development of a tissue-level material model incorporating damage so as to capture the softening behavior of trabecular tissue may be a necessary step towards capturing the ultimate strength of the femur using computational modeling. Segmentation of micro-CT scans of whole bones is another critical issue, and currently there is no objective way of thresholding these scans. This dissertation used global threshold segmentation to identify bone voxels in grey-scale images acquired via micro-CT scanning. Use of more advanced segmentation algorithms based on local adaptive threshold strategy [188] is

recommended to improve the accuracy of femoral strength predictions, since subtle differences in thresholding can result in substantial errors in micro-CT-derived mechanical properties [77].

Another area of future research is performing morphometric analysis in well-defined regions of interest (ROI) within the femur to identify biomechanics-based structural determinants of femoral strength. It is recommended that the ROI be chosen in the vicinity of finite element-predicted locations of failed tissue. For example, for a sideways fall on the hip, the locations of tissue-level failure were trabecular bone at subcapital neck and greater trochanter, and inferior-medial and superior-lateral cortices (Chapter two). Microarchitecture parameters of trabecular (trabecular thickness, spacing, BV/TV, connectivity, structural model index, degree of anisotropy, etc) and cortical (thickness, porosity) bone must be computed in the ROI using direct 3D algorithms, and statistical relationship between these parameters and femoral strength must be determined. In this way, the parameters that come out as significant predictors of femoral strength even after adjusting for the effects of BMD will be regarded as the biomechanics-based structural determinants of femoral strength. To date, microarchitectural analyses in the femurs haven't had much success in identifying structural determinants of bone strength beyond BMD perhaps because they haven't focused on a target ROI but rather on the entire bone. It is also recommended that Individual Trabecular Segmentation (ITS) technique [189] must be applied to the ROI to classify the contained trabeculae by their absolute orientation with respect to this principal trabecular orientation: axial (0–30°), oblique (31–60°), or transverse (61–90°). Inspired from the previous work on vertebra [190], it is recommended that the role of bone volume fraction of “axially-oriented trabeculae” as a potential structural determinant of femoral strength must be tested. The effect of trabecular orientation on hip fragility hasn't been studied before — and thus, this is an exciting topic for future work. Finally, this dissertation focused primarily on osteoporotic bones. Investigating failure mechanisms in a large cohort consisting only of osteopenic bones will be of high clinical significance since current clinical diagnosis tools fail to identify osteopenic individuals who are at high risk of fracture.

In closure, this research improves current understanding of the micromechanics of the human proximal femur and provides new insight into the etiology of age-related hip fractures. Chapter one answered fundamental questions regarding the relative role of cortical vs. trabecular bone in load-carrying capacity of the femoral neck. The study in Chapter two elucidated microstructural failure mechanisms during a sideways fall loading of the hip and identified a novel, morphological determinant of femoral strength. Chapters four and five provided theoretical bounds on the effect of tissue-level ductility on bone strength and indicated that this effect depends little on the bone geometry or morphology. Chapter six suggested that typical population-variations in tissue-level ductility have a relatively modest impact on the femoral strength compared to across-population variations in bone mass or microstructure. This dissertation also outlines areas of research to further advance our understanding of hip fracture etiology and describes a systematic approach to perform morphometric analysis for identifying biomechanics-based structural determinants of femoral strength.

8. REFERENCES

1. Aloia, J.F., et al., *Aging bone loss from the femur, spine, radius, and total skeleton*. Metabolism, 1990. **39**(11): p. 1144-50.
2. Ettinger, M.P., *Aging bone and osteoporosis: strategies for preventing fractures in the elderly*. Arch Intern Med, 2003. **163**(18): p. 2237-46.
3. Richelson, L.S., et al., *Relative contributions of aging and estrogen deficiency to postmenopausal bone loss*. N Engl J Med, 1984. **311**(20): p. 1273-5.
4. Cummings, S.R. and L.J. Melton, *Epidemiology and outcomes of osteoporotic fractures*. Lancet, 2002. **359**(9319): p. 1761-7.
5. Rachner, T.D., S. Khosla, and L.C. Hofbauer, *Osteoporosis: now and the future*. Lancet, 2011. **377**(9773): p. 1276-87.
6. Johnell, O. and J. Kanis, *Epidemiology of osteoporotic fractures*. Osteoporos Int, 2005. **16 Suppl 2**: p. S3-7.
7. Burge, R., et al., *Incidence and economic burden of osteoporosis-related fractures in the United States, 2005-2025*. J Bone Miner Res, 2007. **22**(3): p. 465-75.
8. Feldstein, A.C., et al., *Incidence and demography of femur fractures with and without atypical features*. J Bone Miner Res, 2012. **27**(5): p. 977-86.
9. Kramer, A.M., et al., *Outcomes and costs after hip fracture and stroke. A comparison of rehabilitation settings*. JAMA, 1997. **277**(5): p. 396-404.
10. Cooper, C., et al., *Secular trends in the incidence of hip and other osteoporotic fractures*. Osteoporos Int, 2011. **22**(5): p. 1277-88.
11. Melton, L.J., 3rd, *Epidemiology of hip fractures: implications of the exponential increase with age*. Bone, 1996. **18**(3 Suppl): p. 121S-125S.
12. Gullberg, B., O. Johnell, and J.A. Kanis, *World-wide projections for hip fracture*. Osteoporos Int, 1997. **7**(5): p. 407-13.
13. Lane, N.E., *Epidemiology, etiology, and diagnosis of osteoporosis*. Am J Obstet Gynecol, 2006. **194**(2 Suppl): p. S3-11.
14. Braithwaite, R.S., N.F. Col, and J.B. Wong, *Estimating hip fracture morbidity, mortality and costs*. J Am Geriatr Soc, 2003. **51**(3): p. 364-70.

15. Haentjens, P., et al., *Meta-analysis: excess mortality after hip fracture among older women and men*. *Ann Intern Med*, 2010. **152**(6): p. 380-90.
16. Khosla, S. and L.J. Melton, 3rd, *Clinical practice. Osteopenia*. *N Engl J Med*, 2007. **356**(22): p. 2293-300.
17. Kanis, J.A., *Diagnosis of osteoporosis and assessment of fracture risk*. *Lancet*, 2002. **359**(9321): p. 1929-36.
18. Leslie, W.D., et al., *Fracture risk assessment without bone density measurement in routine clinical practice*. *Osteoporosis International*, 2012. **23**(1): p. 75-85.
19. Schuit, S.C., et al., *Fracture incidence and association with bone mineral density in elderly men and women: the Rotterdam Study*. *Bone*, 2004. **34**(1): p. 195-202.
20. Hernandez, C.J. and T.M. Keaveny, *A biomechanical perspective on bone quality*. *Bone*, 2006. **39**(6): p. 1173-81.
21. Bouxsein, M.L., *Bone quality: where do we go from here?* *Osteoporos Int*, 2003. **14 Suppl 5**: p. S118-27.
22. Seeman, E. and P.D. Delmas, *Bone quality--the material and structural basis of bone strength and fragility*. *N Engl J Med*, 2006. **354**(21): p. 2250-61.
23. Keaveny, T.M., et al., *Biomechanics of trabecular bone*. *Annu Rev Biomed Eng*, 2001. **3**: p. 307-33.
24. Turner, C.H., *Biomechanics of bone: determinants of skeletal fragility and bone quality*. *Osteoporos Int*, 2002. **13**(2): p. 97-104.
25. McCalden, R.W., et al., *Age-related changes in the tensile properties of cortical bone. The relative importance of changes in porosity, mineralization, and microstructure*. *J Bone Joint Surg Am*, 1993. **75**(8): p. 1193-205.
26. Zimmermann, E.A., et al., *Age-related changes in the plasticity and toughness of human cortical bone at multiple length scales*. *Proceedings of the National Academy of Sciences of the United States of America*, 2011. **108**(35): p. 14416-14421.
27. Macdonald, H.M., et al., *Age-related patterns of trabecular and cortical bone loss differ between sexes and skeletal sites: a population-based HR-pQCT study*. *J Bone Miner Res*, 2011. **26**(1): p. 50-62.
28. Carretta, R., et al., *Within subject heterogeneity in tissue-level post-yield mechanical and material properties in human trabecular bone*. *J Mech Behav Biomed Mater*, 2013. **24**: p. 64-73.

29. Bartel, D.L., D.T. Davy, and T.M. Keaveny, *Orthopaedic biomechanics - Mechanics and design in musculoskeletal systems*, 2006, Pearson Prentice Hall: Upper Saddle River, NJ. p. 71-120.
30. Weiner, S. and H.D. Wagner, *The material bone: Structure mechanical function relations*. Annual Review of Materials Science, 1998. **28**: p. 271-298.
31. Rho, J.Y., L. Kuhn-Spearing, and P. Zioupos, *Mechanical properties and the hierarchical structure of bone*. Medical Engineering and Physics, 1998. **20**(2): p. 92-102.
32. Cooper, D.M., et al., *Comparison of microcomputed tomographic and microradiographic measurements of cortical bone porosity*. Calcif Tissue Int, 2004. **74**(5): p. 437-47.
33. Bell, K.L., et al., *Regional differences in cortical porosity in the fractured femoral neck*. Bone, 1999. **24**(1): p. 57-64.
34. Fazzalari, N.L., et al., *Antero-postero differences in cortical thickness and cortical porosity of T12 to L5 vertebral bodies*. Joint Bone Spine, 2006. **73**(3): p. 293-7.
35. Hildebrand, T., et al., *Direct three-dimensional morphometric analysis of human cancellous bone: microstructural data from spine, femur, iliac crest, and calcaneus*. J Bone Miner Res, 1999. **14**(7): p. 1167-74.
36. Ding, M., A. Odgaard, and I. Hvid, *Accuracy of cancellous bone volume fraction measured by micro-CT scanning*. J Biomech, 1999. **32**(3): p. 323-6.
37. Bayraktar, H.H., et al., *Comparison of the elastic and yield properties of human femoral trabecular and cortical bone tissue*. J Biomech, 2004. **37**(1): p. 27-35.
38. Huiskes, R., et al., *Effects of mechanical forces on maintenance and adaptation of form in trabecular bone*. Nature, 2000. **405**(6787): p. 704-6.
39. Eriksen, E.F., *Cellular mechanisms of bone remodeling*. Rev Endocr Metab Disord, 2010. **11**(4): p. 219-27.
40. Boivin, G. and P.J. Meunier, *Changes in bone remodeling rate influence the degree of mineralization of bone*. Connect Tissue Res, 2002. **43**(2-3): p. 535-7.
41. Parfitt, A.M., *Bone remodeling and bone loss: understanding the pathophysiology of osteoporosis*. Clin Obstet Gynecol, 1987. **30**(4): p. 789-811.
42. Lanyon, L.E., *Osteocytes, strain detection, bone modeling and remodeling*. Calcif Tissue Int, 1993. **53 Suppl 1**: p. S102-6; discussion S106-7.
43. Boyce, B.F., et al., *The osteoclast, bone remodelling and treatment of metabolic bone disease*. Eur J Clin Invest, 2012. **42**(12): p. 1332-41.

44. Monroe, D.G., et al., *Update on Wnt signaling in bone cell biology and bone disease*. *Gene*, 2012. **492**(1): p. 1-18.
45. Nawathe, S., et al., *Microstructural failure mechanisms in the human proximal femur for sideways fall loading*. *J Bone Miner Res*, 2014. **29**(2): p. 507-15.
46. Bell, K.L., et al., *Structure of the femoral neck in hip fracture: cortical bone loss in the inferoanterior to superoposterior axis*. *J Bone Miner Res*, 1999. **14**(1): p. 111-9.
47. Poole, K.E., et al., *Changing structure of the femoral neck across the adult female lifespan*. *J Bone Miner Res*, 2010. **25**(3): p. 482-91.
48. Blain, H., et al., *Cortical and trabecular bone distribution in the femoral neck in osteoporosis and osteoarthritis*. *Bone*, 2008. **43**(5): p. 862-8.
49. Zebaze, R.M., et al., *Femoral neck shape and the spatial distribution of its mineral mass varies with its size: Clinical and biomechanical implications*. *Bone*, 2005. **37**(2): p. 243-52.
50. Mayhew, P.M., et al., *Relation between age, femoral neck cortical stability, and hip fracture risk*. *Lancet*, 2005. **366**(9480): p. 129-35.
51. Johannesdottir, F., et al., *Distribution of cortical bone in the femoral neck and hip fracture: a prospective case-control analysis of 143 incident hip fractures; the AGES-REYKJAVIK Study*. *Bone*, 2011. **48**(6): p. 1268-76.
52. Odgaard, A. and H.J. Gundersen, *Quantification of connectivity in cancellous bone, with special emphasis on 3-D reconstructions*. *Bone*, 1993. **14**(2): p. 173-82.
53. Ulrich, D., et al., *The ability of three-dimensional structural indices to reflect mechanical aspects of trabecular bone*. *Bone*, 1999. **25**(1): p. 55-60.
54. Parkkari, J., et al., *Majority of hip fractures occur as a result of a fall and impact on the greater trochanter of the femur: a prospective controlled hip fracture study with 206 consecutive patients*. *Calcif Tissue Int*, 1999. **65**(3): p. 183-7.
55. Mautalen, C.A., E.M. Vega, and T.A. Einhorn, *Are the etiologies of cervical and trochanteric hip fractures different?* *Bone*, 1996. **18**(3 Suppl): p. 133S-137S.
56. Karagas, M.R., et al., *Heterogeneity of hip fracture: age, race, sex, and geographic patterns of femoral neck and trochanteric fractures among the US elderly*. *Am J Epidemiol*, 1996. **143**(7): p. 677-82.
57. Keaveny, T.M., et al., *Age-dependence of femoral strength in white women and men*. *J Bone Miner Res*, 2010. **25**(5): p. 994-1001.

58. Srinivasan, B., et al., *Relationship of femoral neck areal bone mineral density to volumetric bone mineral density, bone size, and femoral strength in men and women*. Osteoporos Int, 2012. **23**(1): p. 155-62.
59. Rivadeneira, F., et al., *Femoral neck BMD is a strong predictor of hip fracture susceptibility in elderly men and women because it detects cortical bone instability: the Rotterdam Study*. J Bone Miner Res, 2007. **22**(11): p. 1781-90.
60. Bousson, V., et al., *Volumetric quantitative computed tomography of the proximal femur: relationships linking geometric and densitometric variables to bone strength. Role for compact bone*. Osteoporos Int, 2006. **17**(6): p. 855-64.
61. Lang, T.F., et al., *Volumetric quantitative computed tomography of the proximal femur: precision and relation to bone strength*. Bone, 1997. **21**(1): p. 101-8.
62. Lotz, J., E. Cheal, and W. Hayes, *Finite element predictions of stress distributions within the proximal femur during gait and falls*. Journal of Biomechanics, 1992(In press).
63. Verhulp, E., B. van Rietbergen, and R. Huiskes, *Load distribution in the healthy and osteoporotic human proximal femur during a fall to the side*. Bone, 2008. **42**(1): p. 30-5.
64. Verhulp, E., B. van Rietbergen, and R. Huiskes, *Comparison of micro-level and continuum-level voxel models of the proximal femur*. J Biomech, 2006. **39**(16): p. 2951-7.
65. Oxlund, H., et al., *Reduced concentrations of collagen cross-links are associated with reduced strength of bone*. Bone, 1995. **17**(4 Suppl): p. 365S-371S.
66. Wang, X., et al., *Age-related changes in the collagen network and toughness of bone*. Bone, 2002. **31**(1): p. 1-7.
67. Eyre, D.R., I.R. Dickson, and K. Van Ness, *Collagen cross-linking in human bone and articular cartilage. Age-related changes in the content of mature hydroxypyridinium residues*. Biochem J, 1988. **252**(2): p. 495-500.
68. Vashishth, D., et al., *Influence of nonenzymatic glycation on biomechanical properties of cortical bone*. Bone, 2001. **28**(2): p. 195-201.
69. Paschalis, E.P., et al., *Bone fragility and collagen cross-links*. J Bone Miner Res, 2004. **19**(12): p. 2000-4.
70. Keaveny, T.M., *Strength of Trabecular Bone*. Bone Mechanics Handbook, 2001: p. 16-16-42.
71. Ryan, S.D. and J.L. Williams, *Tensile testing of rodlike trabeculae excised from bovine femoral bone*. J Biomech, 1989. **22**(4): p. 351-5.

72. Mente, P.L. and J.L. Lewis, *Experimental method for the measurement of the elastic modulus of trabecular bone tissue*. Journal of Orthopaedic Research, 1989. **7**(3): p. 456-61.
73. Bini, F., et al., *Microtensile measurements of single trabeculae stiffness in human femur*. J Biomech, 2002. **35**(11): p. 1515-9.
74. Choi, K. and S.A. Goldstein, *A comparison of the fatigue behavior of human trabecular and cortical bone tissue*. J Biomech, 1992. **25**(12): p. 1371-81.
75. Kuhn, J.L., et al., *Comparison of the trabecular and cortical tissue moduli from human iliac crests*. J Orthop Res, 1989. **7**(6): p. 876-84.
76. Hernandez, C.J., et al., *Trabecular microfracture and the influence of pyridinium and non-enzymatic glycation-mediated collagen cross-links*. Bone, 2005. **37**(6): p. 825-32.
77. Bevill, G., et al., *The influence of boundary conditions and loading mode on high-resolution finite element-computed trabecular tissue properties*. Bone, 2009. **44**(4): p. 573-8.
78. Nawathe, S., F. Juillard, and T.M. Keaveny, *Theoretical bounds for the influence of tissue-level ductility on the apparent-level strength of human trabecular bone*. J Biomech, 2013. **46**(7): p. 1293-9.
79. Eswaran, S.K., et al., *A computational assessment of the independent contribution of changes in canine trabecular bone volume fraction and microarchitecture to increased bone strength with suppression of bone turnover*. J Biomech, 2007. **40**(15): p. 3424-31.
80. Bessho, M., et al., *Prediction of strength and strain of the proximal femur by a CT-based finite element method*. J Biomech, 2007. **40**(8): p. 1745-53.
81. Keyak, J.H., et al., *Validation of an Automated-Method of 3-Dimensional Finite-Element Modeling of Bone*. Journal of Biomedical Engineering, 1993. **15**(6): p. 505-509.
82. Van Rietbergen, B., et al., *A new method to determine trabecular bone elastic properties and loading using micromechanical finite element models*. Journal of Biomechanics, 1995. **28**(1): p. 69-81.
83. Bevill, G., et al., *Influence of bone volume fraction and architecture on computed large-deformation failure mechanisms in human trabecular bone*. Bone, 2006. **39**(6): p. 1218-25.
84. Fields, A.J., et al., *Vertebral fragility and structural redundancy*. J Bone Miner Res, 2012. **27**(10): p. 2152-8.
85. Keaveny, T.M., et al., *Femoral bone strength and its relation to cortical and trabecular changes after treatment with PTH, alendronate, and their combination as assessed by*

- finite element analysis of quantitative CT scans.* J Bone Miner Res, 2008. **23**(12): p. 1974-82.
86. Orwoll, E.S., et al., *Finite element analysis of the proximal femur and hip fracture risk in older men.* J Bone Miner Res, 2009. **24**(3): p. 475-83.
87. Keyak, J.H., *Improved prediction of proximal femoral fracture load using nonlinear finite element models.* Medical Engineering & Physics, 2001. **23**(3): p. 165-173.
88. Hou, F.J., et al., *Human vertebral body apparent and hard tissue stiffness.* Journal of Biomechanics, 1998. **31**(11): p. 1009-15.
89. Kabel, J., et al., *The role of an effective isotropic tissue modulus in the elastic properties of cancellous bone.* Journal of Biomechanics, 1999. **32**(7): p. 673-80.
90. Nagaraja, S., T.L. Couse, and R.E. Guldborg, *Trabecular bone microdamage and microstructural stresses under uniaxial compression.* Journal of Biomechanics, 2005. **38**(4): p. 707-16.
91. Niebur, G.L., et al., *High-resolution finite element models with tissue strength asymmetry accurately predict failure of trabecular bone.* Journal of Biomechanics, 2000. **33**: p. 1575-1583.
92. Homminga, J., et al., *The osteoporotic vertebral structure is well adapted to the loads of daily life, but not to infrequent "error" loads.* Bone, 2004. **34**(3): p. 510-6.
93. Adams, M.F., et al. *Ultrascaleable implicit finite element analyses in solid mechanics with over a half a billion degrees of freedom.* in *ACM/IEEE Proceedings of SC2004: High Performance Networking and Computing.* 2004.
94. Arbenz, P., et al., *A scalable multi-level preconditioner for matrix-free μ -finite element analysis of human bone structures.* International Journal for Numerical Methods in Engineering, 2008. **73**(7): p. 927-947.
95. Morgan, E.F., et al., *Contribution of inter-site variations in architecture to trabecular bone apparent yield strains.* J Biomech, 2004. **37**(9): p. 1413-20.
96. Stolken, J.S. and J.H. Kinney, *On the importance of geometric nonlinearity in finite-element simulations of trabecular bone failure.* Bone, 2003. **33**(4): p. 494-504.
97. Keaveny, T.M., *Strength of trabecular bone,* in *Bone mechanics handbook*, S.C. Cowin, Editor 2001, CRC press: Boc Raton, Fl. p. 16-1-42.
98. Eswaran, S.K., et al., *The micromechanics of cortical shell removal in the human vertebral body.* Comput Method Appl M, 2007. **196**(31): p. 3025-32.

99. Lang, T., et al., *Volumetric Quantitative Computed Tomography of the Femur: Precision and Relation to Bone Strength*. Bone, 1997. **21**(1): p. 101-108.
100. Bouxsein, M.L. and R.J. Fajardo, *Cortical stability of the femoral neck and hip fracture risk*. Lancet, 2005. **366**(9496): p. 1523-4; author reply 1524-5.
101. Turner, C.H., *The biomechanics of hip fracture*. Lancet, 2005. **366**(9480): p. 98-9.
102. Holzer, G., et al., *Hip fractures and the contribution of cortical versus trabecular bone to femoral neck strength*. J Bone Miner Res, 2009. **24**(3): p. 468-74.
103. Koivumaki, J.E., et al., *Cortical bone finite element models in the estimation of experimentally measured failure loads in the proximal femur*. Bone, 2012. **51**(4): p. 737-40.
104. Riggs, B.L., et al., *Population-based study of age and sex differences in bone volumetric density, size, geometry, and structure at different skeletal sites*. J Bone Miner Res, 2004. **19**(12): p. 1945-54.
105. Manske, S.L., et al., *Cortical and trabecular bone in the femoral neck both contribute to proximal femur failure load prediction*. Osteoporos Int, 2009. **20**(3): p. 445-53.
106. Roberts, B.J., et al., *Comparison of hip fracture risk prediction by femoral aBMD to experimentally measured factor of risk*. Bone, 2010. **46**(3): p. 742-6.
107. Keyak, J.H., *Relationships between femoral fracture loads for two load configurations*. Journal of Biomechanics, 2000. **33**(4): p. 499-502.
108. Courtney, A.C., et al., *Age-related reductions in the strength of the femur tested in a fall-loading configuration*. J Bone Joint Surg Am, 1995. **77**(3): p. 387-95.
109. de Bakker, P.M., et al., *During sideways falls proximal femur fractures initiate in the superolateral cortex: evidence from high-speed video of simulated fractures*. J Biomech, 2009. **42**(12): p. 1917-25.
110. Demes, B., W.L. Jungers, and C. Walker, *Cortical bone distribution in the femoral neck of strepsirhine primates*. J Hum Evol, 2000. **39**(4): p. 367-79.
111. Van Rietbergen, B., et al., *Trabecular bone tissue strains in the healthy and osteoporotic human femur*. Journal of Bone and Mineral Research, 2003. **18**(10): p. 1781-1788.
112. Nishiyama, K.K., et al., *Proximal femur bone strength estimated by a computationally fast finite element analysis in a sideways fall configuration*. J Biomech, 2013. **46**(7): p. 1231-6.
113. Wachter, N.J., et al., *Correlation of bone mineral density with strength and microstructural parameters of cortical bone in vitro*. Bone, 2002. **31**(1): p. 90-5.

114. Augat, P., H. Reeb, and L.E. Claes, *Prediction of fracture load at different skeletal sites by geometric properties of the cortical shell*. J Bone Miner Res, 1996. **11**(9): p. 1356-63.
115. Nawathe, S., et al., *Cortical-Trabecular load sharing and high risk tissue distribution in the human proximal femur*. 57th Annual Meeting of the Orthopaedic Research Society, Long Beach CA, 2011.
116. Bevill, G. and T.M. Keaveny, *Trabecular bone strength predictions using finite element analysis of micro-scale images at limited spatial resolution*. Bone, 2009. **44**(4): p. 579-84.
117. Macneil, J.A. and S.K. Boyd, *Bone strength at the distal radius can be estimated from high-resolution peripheral quantitative computed tomography and the finite element method*. Bone, 2008. **42**(6): p. 1203-13.
118. Keaveny, T.M., et al., *Biomechanics of trabecular bone*. Annual Review of Biomedical Engineering, 2001. **3**: p. 307-333.
119. Bevill, G., et al., *Influence of bone volume fraction and architecture on computed large-deformation failure mechanisms in human trabecular bone*. Bone, 2006. **39**(6): p. 1218-25.
120. Fyhrie, D.P. and M.B. Schaffler, *Failure mechanisms in human vertebral cancellous bone*. Bone, 1994. **15**(1): p. 105-9.
121. Nazarian, A., et al., *The interaction of microstructure and volume fraction in predicting failure in cancellous bone*. Bone, 2006. **39**(6): p. 1196-202.
122. Shi, X., et al., *Effects of trabecular type and orientation on microdamage susceptibility in trabecular bone*. Bone, 2010. **46**(5): p. 1260-6.
123. Liu, X.S., et al., *Micromechanical analyses of vertebral trabecular bone based on individual trabeculae segmentation of plates and rods*. J Biomech, 2009. **42**(3): p. 249-56.
124. Amling, M., et al., *Heterogeneity of the skeleton: comparison of the trabecular microarchitecture of the spine, the iliac crest, the femur, and the calcaneus*. J Bone Miner Res, 1996. **11**(1): p. 36-45.
125. Bagi, C.M., et al., *Morphological and structural characteristics of the proximal femur in human and rat*. Bone, 1997. **21**(3): p. 261-267.
126. Roy, M.E., et al., *Mechanical and morphological variation of the human lumbar vertebral cortical and trabecular bone*. J Biomed Mater Res, 1999. **44**(2): p. 191-7.
127. Gregory, J.S. and R.M. Aspden, *Femoral geometry as a risk factor for osteoporotic hip fracture in men and women*. Med Eng Phys, 2008. **30**(10): p. 1275-86.

128. Carpenter, R.D., et al., *New QCT analysis approach shows the importance of fall orientation on femoral neck strength*. J Bone Miner Res, 2005. **20**(9): p. 1533-42.
129. Taylor, R.L., *FEAP - A Finite Element Analysis Program, Users Manual*, 2003, University of California: Berkeley.
130. Papadopoulos, P. and J. Lu, *A general framework for the numerical solution of problems in finite elasto-plasticity*. Computer Methods in Applied Mechanics and Engineering, 1998. **159**(1-2): p. 1-18.
131. Conner, R.J., et al., *Inspection and management of bridges with fracture-critical details : a synthesis of highway practice*. NCHRP synthesis,2005, Washington, D.C.: Transportation Research Board. 75 p.
132. Holzer, G., et al., *Hip Fractures and the Contribution of Cortical Versus Trabecular Bone to Femoral Neck Strength*. Journal of Bone and Mineral Research, 2009. **24**(3): p. 468-474.
133. Koivumaki, J.E., et al., *Ct-based finite element models can be used to estimate experimentally measured failure loads in the proximal femur*. Bone, 2012. **50**(4): p. 824-9.
134. Gupta, H.S. and P. Zioupos, *Fracture of bone tissue: The 'hows' and the 'whys'*. Med Eng Phys, 2008. **30**(10): p. 1209-26.
135. Jaasma, M.J., et al., *Biomechanical effects of intraspecimen variations in tissue modulus for trabecular bone*. Journal of Biomechanics, 2002. **35**(2): p. 237-246.
136. Bourne, B.C. and M.C. van der Meulen, *Finite element models predict cancellous apparent modulus when tissue modulus is scaled from specimen CT-attenuation*. Journal of Biomechanics, 2004. **37**(5): p. 613-21.
137. Burstein, A.H., D.T. Reilly, and M. Martens, *Aging of bone tissue: mechanical properties*. Journal of Bone and Joint Surgery. American Volume, 1976. **58**(1): p. 82-6.
138. Reilly, D.T. and A.H. Burstein, *The elastic and ultimate properties of compact bone tissue*. Journal of Biomechanics, 1975. **8**: p. 393-405.
139. Courtney, A.C., W.C. Hayes, and L.J. Gibson, *Age-related differences in post-yield damage in human cortical bone. Experiment and model*. Journal of Biomechanics, 1996. **29**(11): p. 1463-71.
140. Llorca, J. and C. Gonzalez, *Microstructural factors controlling the strength and ductility of particle-reinforced metal-matrix composites*. Journal of the Mechanics and Physics of Solids, 1998. **46**(1): p. 1-28.

141. Mortensen, A. and J. Llorca, *Metal Matrix Composites*. Annual Review of Materials Research, Vol 40, 2010. **40**: p. 243-270.
142. Gibson, L.J. and M.F. Ashby, *Cellular solids: structures & properties*. Second Edition ed1997, Oxford: Pergamon Press. 510.
143. Maiti, S.K., L.J. Gibson, and M.F. Ashby, *Deformation and Energy-Absorption Diagrams for Cellular Solids*. Acta Metallurgica, 1984. **32**(11): p. 1963-1975.
144. Verhulp, E., et al., *Micro-finite element simulation of trabecular-bone post-yield behaviour--effects of material model, element size and type*. Comput Methods Biomech Biomed Engin, 2008. **11**(4): p. 389-95.
145. Beck, J.D., et al., *Three-dimensional imaging of trabecular bone using the computer numerically controlled milling technique*. Bone, 1997. **21**(3): p. 281-7.
146. Hildebrand, T., et al., *Direct three-dimensional morphometric analysis of human cancellous bone: microstructural data from spine, femur, iliac crest, and calcaneus*. Journal of Bone and Mineral Research, 1999. **14**(7): p. 1167-74.
147. Laib, A., et al. *Direct measures of trabecular bone architecture from MR images*. in *Noninvasive assessment of trabecular bone architecture and the competence of bone*. 2001. Big Sur, California: Kluwer Academic/Plenum Publishers.
148. Niebur, G.L., et al., *Convergence behavior of high-resolution finite element models of trabecular bone*. Journal of Biomechanical Engineering, 1999. **121**(6): p. 629-635.
149. Guldberg, R.E., S.J. Hollister, and G.T. Charras, *The accuracy of digital image-based finite element models*. Journal of Biomechanical Engineering, 1998. **120**(4): p. 289-295.
150. Sanyal, A., et al., *Shear strength behavior of human trabecular bone*. J Biomech, 2012. **45**(15): p. 2513-9.
151. Crawford, R.P., C.E. Cann, and T.M. Keaveny, *Finite element models predict in vitro vertebral body compressive strength better than quantitative computed tomography*. Bone, 2003. **33**(4): p. 744-50.
152. Cowin, S., ed. *Bone Mechanics Handbook*. 2 ed. 2001, CRC Press: Boca Raton. 968.
153. Morgan, E.F. and T.M. Keaveny, *Dependence of yield strain of human trabecular bone on anatomic site*. Journal of Biomechanics, 2001. **34**(5): p. 569-577.
154. Kopperdahl, D.L. and T.M. Keaveny, *Yield strain behavior of trabecular bone*. Journal of Biomechanics, 1998. **31**(7): p. 601-8.
155. Nazarian, A. and R. Muller, *Time-lapsed microstructural imaging of bone failure behavior*. J Biomech, 2004. **37**(1): p. 55-65.

156. Easley, S.K., et al., *Contribution of the intra-specimen variations in tissue mineralization to PTH- and raloxifene-induced changes in stiffness of rat vertebrae*. Bone, 2010. **46**(4): p. 1162-9.
157. Jaasma, M.J., et al. *The effects of intraspecimen variations in tissue modulus on the apparent mechanical properties of trabecular bone*. in *Trans. Orthop. Res. Soc.* 2001. San Francisco.
158. McNamara, L.M., et al., *Stress-concentrating effect of resorption lacunae in trabecular bone*. J Biomech, 2006. **39**(4): p. 734-41.
159. Verhulp, E., et al., *Indirect determination of trabecular bone effective tissue failure properties using micro-finite element simulations*. J Biomech, 2008. **41**(7): p. 1479-85.
160. Vaughan, T.J., C.T. McCarthy, and L.M. McNamara, *A three-scale finite element investigation into the effects of tissue mineralisation and lamellar organisation in human cortical and trabecular bone*. J Mech Behav Biomed Mater, 2012. **12C**: p. 50-62.
161. Zysset, P.K. and A. Curnier, *A 3D damage model for trabecular bone based on fabric tensors*. Journal of Biomechanics, 1996. **29**(12): p. 1549-58.
162. Garcia, D., et al., *A three-dimensional elastic plastic damage constitutive law for bone tissue*. Biomech Model Mechanobiol, 2009. **8**(2): p. 149-65.
163. Kosmopoulos, V. and T.S. Keller, *Predicting trabecular bone microdamage initiation and accumulation using a non-linear perfect damage model*. Med Eng Phys, 2008. **30**(6): p. 725-32.
164. Currey, J.D., *Bones — Structure and Mechanics*, 2002, Princeton University Press: Princeton, New Jersey. p. 124-138.
165. Turner, C.H., *Determinants of skeletal fragility and bone quality*. J Musculoskelet Neuronal Interact, 2002. **2**(6): p. 527-8.
166. Ammann, P. and R. Rizzoli, *Bone strength and its determinants*. Osteoporos Int, 2003. **14 Suppl 3**: p. S13-8.
167. Eswaran, S.K., et al., *Cortical and trabecular load sharing in the human vertebral body*. J Bone Miner Res, 2006. **21**(2): p. 307-14.
168. Bevill, G., F. Farhamand, and T.M. Keaveny, *Heterogeneity of yield strain in low-density versus high-density human trabecular bone*. Journal of Biomechanics, 2009. **42**(13): p. 2165-70.
169. Nawathe, S., et al., *Cortical-trabecular load-sharing in the human femoral neck*. J Biomech, 2014. **submitted**.

170. Sornay-Rendu, E., et al., *Alterations of cortical and trabecular architecture are associated with fractures in postmenopausal women, partially independent of decreased BMD measured by DXA: the OFELY study*. J Bone Miner Res, 2007. **22**(3): p. 425-33.
171. Augat, P., et al., *Accuracy of cortical and trabecular bone measurements with peripheral quantitative computed tomography (pQCT)*. Phys Med Biol, 1998. **43**(10): p. 2873-83.
172. LaCroix, A.Z., et al., *Hip structural geometry and incidence of hip fracture in postmenopausal women: what does it add to conventional bone mineral density?* Osteoporos Int, 2010. **21**(6): p. 919-29.
173. Boutroy, S., et al., *In vivo assessment of trabecular bone microarchitecture by high-resolution peripheral quantitative computed tomography*. J Clin Endocrinol Metab, 2005. **90**(12): p. 6508-15.
174. Rauch, F. and F.H. Glorieux, *Osteogenesis imperfecta*. Lancet, 2004. **363**(9418): p. 1377-85.
175. Lenart, B.A., et al., *Association of low-energy femoral fractures with prolonged bisphosphonate use: a case control study*. Osteoporos Int, 2009. **20**(8): p. 1353-62.
176. Eswaran, S.K., A. Gupta, and T.M. Keaveny, *Locations of bone tissue at high risk of initial failure during compressive loading of the human vertebral body*. Bone, 2007. **41**(4): p. 733-9.
177. Pinilla, T.P., et al., *Impact direction from a fall influences the failure load of the proximal femur as much as age-related bone loss*. Calcif Tissue Int, 1996. **58**(4): p. 231-5.
178. Courtney, A.C., et al., *Effects of loading rate on strength of the proximal femur*. Calcif Tissue Int, 1994. **55**(1): p. 53-8.
179. Bessho, M., et al., *Prediction of proximal femur strength using a CT-based nonlinear finite element method: differences in predicted fracture load and site with changing load and boundary conditions*. Bone, 2009. **45**(2): p. 226-31.
180. Gregory, C.O., et al., *Detection of cardio-metabolic risk by BMI and waist circumference among a population of Guatemalan adults*. Public Health Nutr, 2008. **11**(10): p. 1037-45.
181. Shi, X., X. Wang, and G.L. Niebur, *Effects of loading orientation on the morphology of the predicted yielded regions in trabecular bone*. Ann Biomed Eng, 2009. **37**(2): p. 354-62.
182. Carretta, R., et al., *Novel method to analyze post-yield mechanical properties at trabecular bone tissue level*. J Mech Behav Biomed Mater, 2013. **20**: p. 6-18.

183. Nawathe, S., et al. *The Effect of Bone Tissue Ductility on Vertebral and Femoral Strength*. in *35th Annual Meeting of the American Society for Bone and Mineral Research*. 2013. Baltimore, MD.
184. Black, D.M., et al., *Proximal femoral structure and the prediction of hip fracture in men: a large prospective study using QCT*. *J Bone Miner Res*, 2008. **23**(8): p. 1326-33.
185. Cheng, X.G., et al., *Assessment of the strength of proximal femur in vitro: relationship to femoral bone mineral density and femoral geometry*. *Bone*, 1997. **20**(3): p. 213-8.
186. Yeh, O.C. and T.M. Keaveny. *Roles of microdamage and microfracture in the mechanical behavior of trabecular bone*. in *Trans. Orthop. Res. Soc.* 2000. Orlando.
187. Dragomir-Daescu, D., et al., *Robust QCT/FEA models of proximal femur stiffness and fracture load during a sideways fall on the hip*. *Ann Biomed Eng*, 2011. **39**(2): p. 742-55.
188. Burghardt, A.J., G.J. Kazakia, and S. Majumdar, *A local adaptive threshold strategy for high resolution peripheral quantitative computed tomography of trabecular bone*. *Ann Biomed Eng*, 2007. **35**(10): p. 1678-86.
189. Liu, X.S., et al., *Complete volumetric decomposition of individual trabecular plates and rods and its morphological correlations with anisotropic elastic moduli in human trabecular bone*. *J Bone Miner Res*, 2008. **23**(2): p. 223-35.
190. Fields, A.J., et al., *Influence of vertical trabeculae on the compressive strength of the human vertebra*. *J Bone Miner Res*, 2011. **26**(2): p. 263-9.